

Contactless Energy Transfer System For Satellite Applications

Research and design of a CET system to replace Slip-Ring Assemblies and eliminate their limited lifetime and working voltage

Bob Morssink



Delft University of Technology

Contactless Energy Transfer System For Satellite Applications

Research and design of a CET system to replace Slip-Ring Assemblies and eliminate their limited lifetime and working voltage

by

Bob Morssink

to obtain the degree of Master of Science
at the Delft University of Technology,
to be defended publicly on Wednesday October 9, 2024 at 10:00 AM.

Student number: 4722620
Project duration: September 1, 2023 – October 9, 2024
Thesis committee: Dr. ir. P. Bauer, TU Delft, Advisor
J. Dong PhD, TU Delft, Supervisor
Dr. M. Ghaffarian Niasar, TU Delft

Cover: FundsUp RoadEO – Using Space Tech to revolutionize road maintenance (Modified)
Style: TU Delft Report Style, with modifications by Daan Zwaneveld

An electronic version of this thesis is available at <http://repository.tudelft.nl/>.

Abstract

The number of satellites launched every year is ever-increasing. Satellites generate energy through solar panels, transferring it to the satellite hub using Slip Ring Assemblys (SRAs). However, SRAs suffer from limited lifetime and operating voltages. Therefore, this research investigates a Contactless Energy Transfer (CET) system for the satellite to eliminate these problems. The system consists of an input source, inverter, Alternating Current (AC)-link and rectifier. A single diode model is introduced for the solar panel input source to model its behaviour. After a brief comparison, the Inductive Power Transfer (IPT) method is favoured over the Capacitive Power Transfer (CPT) method. As a result, the AC-link includes a transformer to obtain the contactless energy transfer. The Single Active Bridge (SAB) topology is chosen after comparing the characteristics of the SAB and Dual Active Bridge (DAB) topologies. Afterwards, two SAB converters, the Single Active Bridge with Output Inductor (SABL) and LLC converter, are compared before choosing the LLC converter. With the CET system design completed, the design procedure for the LLC converter is presented, resulting in transformer requirements. A coaxial solenoid transformer design procedure where the inductance and losses are modelled is used to create a prototype transformer. The models are validated using Finite Element Method Magnetics (FEMM). The designed transformer met the inductance requirement. However, the losses were too significant to meet the overall CET system efficiency requirement.

Contents

List of Abbreviations	4
1 Introduction	6
2 Background	9
2.1 Space environment	9
2.1.1 Particles in space	9
2.1.2 Satellite Orbits	10
2.1.3 Effects on Satellites.	12
2.2 Slip Ring Assembly Developments.	13
2.2.1 Breakdown Research	14
2.2.2 Deep Dielectric Charging.	16
2.2.3 Manufacturing	16
2.3 Wireless Power Transfer Developments	17
3 System Design	20
3.1 Input Source	20
3.1.1 General Solar Panel info	21
3.1.2 Solar Cell	21
3.1.3 Input source to CET	24
3.2 Capacitive vs Inductive Power Transfer	24
3.2.1 Comparative Study.	24
3.2.2 IPT Choice Implications on System Design	25
3.3 Converter Topology Considerations	26
3.3.1 Primary Side Inverter	27
3.3.2 Single vs Dual Active Bridge.	29
3.3.3 Comparative Study of SABL and LLC topologies	31
3.3.4 Conclusion	38
3.4 Transformer choice	38
3.4.1 Transformer Geometries	38
3.4.2 Coaxial Solenoid Transformer	40
4 LLC Design	42
4.1 Design Process	42
4.2 Analysis of the Resulting LLC Design.	46
4.2.1 Voltage Gain	46
4.2.2 Current Analysis in the Resonant Tank	48
4.3 Conclusion	48
5 Design of a Coaxial Solenoid Transformer	50
5.1 Transformer modelling	52
5.1.1 Inductance Estimation	53
5.1.2 Winding Losses	55
5.1.3 Core Losses	57
5.1.4 Foundation of FEMM and Simulation Model	58
5.2 Wire and Core Material Selection	60
5.2.1 Wire Considerations	60
5.2.2 Magnetic Rods	61
5.3 Design Procedure	62
5.3.1 Analytical Transformer Sizing	62
5.3.2 FEMM Transformer Refinement and Power Losses	64

5.4	Results	64
5.4.1	Analytical vs FEMM Sizing	64
5.4.2	Winding Losses	65
5.4.3	Core Losses	66
5.5	Final Transformer Parameters	68
5.5.1	Recalculation LLC components	68
6	Conclusions and Future Work	70
6.1	Conclusion	70
6.2	Future Work	71
A	LTspice Circuit	77
B	Core specifications	78
B.1	Ferrite rods	78
B.1.1	Rod Dimensions	78
B.1.2	Core Loss Curves	78

List of Abbreviations

AC	Alternating Current
AM	Additive Manufacturing
BCM	Boundary Conduction Mode
CCM	Continuous Conduction Mode
CET	Contactless Energy Transfer
CPT	Capacitive Power Transfer
CRAND	Cosmic Ray Albedo Neutron Decay
DAB	Dual Active Bridge
DC	Direct Current
DCM	Discontinuous Conduction Mode
EM	Electric Machine
EOL	End of life
ESA	European Space Agency
ESD	Electrostatic Discharge
ESP	Electrical Sustainable Power
EUV	Extreme UltraViolet
FEM	Finite Element Method
FEMM	Finite Element Method Magnetics
FHA	First Harmonic Approximation
GEO	Geosynchronous Orbit
GPS	Global Positioning System
HV	High Voltage
IPT	Inductive Power Transfer
ISS	International Space Station
LEO	Low-Earth Orbit
MEO	Medium-Earth Orbit
MPPT	Maximum Power Point Tracker
NASA	National Aeronautics and Space Administration
PCB	Printed Circuit Board
RMS	Root Mean Square

RMSD Root Mean Square Deviation

SAB Single Active Bridge

SABL Single Active Bridge with Output Inductor

SADA Solar Array Drive Assembly

SRA Slip Ring Assembly

THD Total Harmonic Distortion

WPT Wireless Power Transfer

ZVS Zero Voltage Switching

1

Introduction

The history of satellites began with the Intelsat I, nicknamed Early Bird, in 1965. Intelsat I was the first satellite launched for commercial purposes and provided telecommunication capabilities for audio and television [1]. Although Intelsat I only had hardware capability for a single television channel, it started the revolution of communication networks. Today, Intelsat satellites offer various functionalities, e.g., mobile communication, data transfer, internet access, and television broadcasting.

Intelsat is not the sole company that has satellites in orbit. Other companies have launched satellites into space to provide various services. All satellites are an integral part of our society in the modern era. As satellites enable devices to communicate with each other from anywhere on the planet, many sectors use satellites, including TV broadcasts and mobile communication networks, navigation systems, scientific research and outer space missions.

Besides communication, satellites perform valuable global measurements of the Earth's climate. For example, satellites are vital for collecting data in remote locations and oceans. Furthermore, analyzing clouds and humidity at higher altitudes is easier from space than Earth's surface [2]. The effects of climate change, such as loss and altering of vegetation in large areas, are most consistent performed from space [3].

Even though climate phenomena are already tracked with the current technology present in satellites, greater accuracy from the measurements is required for analyzing climate effects on a larger time scale. Small variations in the global data can indicate the long-term effects [2]. Currently, local vegetation alteration data needs to be validated by in-field research due to a lack of accuracy [3]. These limitations indicate the future development of measurement equipment used for environmental research.

As a result of the evolution of satellite measurement equipment and the increased dependency on satellite functions, more and more satellites are required. Figure 1.1 shows the number of satellites launched annually between 2019 and 2023 [4]. In four years, the global launch attempts have more than doubled.

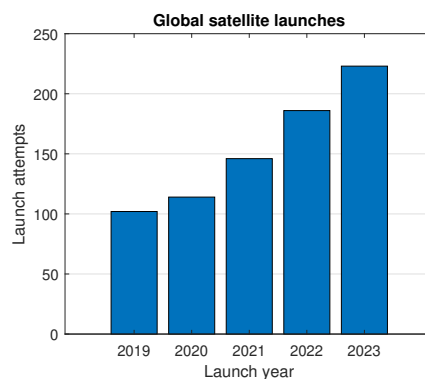


Figure 1.1: The global satellite launches attempts per year provided by [4].

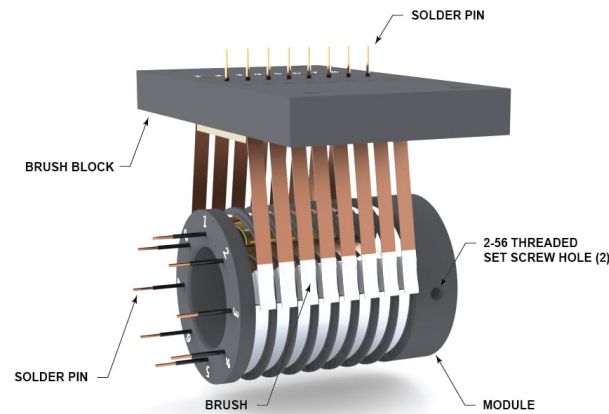


Figure 1.2: The SR001 series, manufactured by RotatySystems, is an example of an SRA capable of transferring 3 A to 26 A of current at a maximum voltage of 150 V_{DC}.

The cost of satellite launches is often expressed in cost per mass (\$/kg). This is done because launching objects into orbit costs an enormous amount of energy. Adding extra weight means more energy, and consequently, more fuel is needed for the launch. In the past decades, the cost per mass has decreased significantly for satellites destined for the Low-Earth Orbit (LEO) when the costs are adjusted for inflation. The decrease is especially true for the medium and heavy payloads carrying respectively between 2.000 kg and 20.000 kg and above 20.000 kg [5]. This reduction could also play a factor in the rise of satellite launches.

While the equipment onboard satellites differs vastly depending on the functionality of the satellite, all equipment onboard needs to be powered. A large energy storage could be charged before the satellite is launched to provide the energy required during operation. However, large energy storage often adds significant extra weight and, consequently, additional cost. Furthermore, satellites operate for several years, e.g. SpaceX satellites operate for 5-6 years [6], requiring huge energy storage.

Satellites generate their power in space to eliminate the large energy storage issue. The most common way to generate power in space is via solar panels. In theory, solar panels could provide satellites with energy for their whole operational lifetime. Unfortunately, the solar panels degrade over time, reducing the energy generation.

The maximum efficiency of the solar panel is achieved when it is angled perpendicular to the incoming solar rays. For that reason, solar panels on satellites are mounted on a rotating axle, ensuring the maximum power generation possible [7]. Despite the increase in efficiency due to the rotating of the panels, a problem is introduced regarding the energy transfer from the solar panels to the satellite hub.

While the solar panels rotate, the satellite hub or core needs to remain stationary with respect to the solar panels to ensure measurements remain aimed towards the Earth. Therefore, the energy generated by the moving solar panels must be transferred to the stationary hub. Currently, the power is transferred via SRA. From Figure 1.2, it can be seen that SRAs consists of multiple conductive brushes pressed onto conductive rings via springs.

Despite the maturity of SRAs, there are inherent downsides to the transfer method. First, mechanical friction between the brushes and the rings causes wear, resulting in an intrinsic limited lifetime. Second, arcing and Electrostatic Discharge (ESD) can occur due to deep space charging, and the likelihood of it is increased because of the conductive debris [8]. Third and lastly, due to the arcing, the working voltage of the SRA and, therefore, the power system is limited [9].

Because of the SRA limitations, this research investigates the other methods to transfer energy from the solar panels to the satellite. The main research question is given below.

- How can energy be transferred from the stator to the rotor contactlessly in a space environment?

Besides the main research question, the following sub-research questions are investigated in this research.

- What is the influence of the space environment on electronics used in satellites?
- What is the optimal structure for the AC-link?
- What is the optimal conversion technique to transfer energy contactlessly?

The structure of this research is as follows: in Chapter 2 information regarding the space environment, SRAs and Wireless Power Transfer (WPT) is provided. Chapter 3 introduces the satellite CET system and defines the input source, AC-link, converter topology and transformer geometry. Next, Chapter 4 shows the LLC converter design process and resulting design followed by the transformer design process and results in Chapter 5. This work is completed by the conclusions and future work suggestions in Chapter 6.

2

Background

Before the design of the CET system in this research starts, research is conducted regarding the space environment, SRA developments, and current WPT meant for use in satellites. The space environment is vastly different to the environment present on Earth. Therefore, the electronic design guidelines can not be transferred to space applications. Design limitations are discovered by researching the composition of the Earth's atmosphere at different altitudes.

Afterwards, the SRA developments found in the literature are presented. The current research presents limitations and problems from the SRA concept.

Lastly, WPT designs found in the literature are used to create a basic understanding of the ongoing developments.

2.1. Space environment

To ensure the designed WPT system works in the space environment, knowledge of the harmful processes on electronic devices needs to be acquired. First, the environment of the Earth's atmosphere is described based on research. Second, the orbits in which satellites revolve around the Earth are characterized based on altitude, after which the particles present are described. Third and lastly, the potential adverse effects of the particles and radiation on satellite electronics are presented.

2.1.1. Particles in space

Contrary to intuition, the space environment around Earth is not a perfect vacuum. For example, Earth's atmosphere contains many particles protecting organic life from Extreme UltraViolet (EUV). Even beyond the Earth's atmosphere, particles are still floating in space. These particles originate from the solar wind plasmas, and [10] describes their origin extensively. The following section describes the origin of the solar plasmas and their effect on the Earth's atmosphere based on the information in [10].

As the sun's surface is extremely hot, hydrogen and helium atoms are accelerated enough to escape the sun's gravitational forces. These escaped atoms are ions and form a fully ionized plasma called the solar wind plasma. The plasma remains fully ionized due to the sun's constant radiation. As a result of heat, compression, and expansion, the solar wind plasma travels at supersonic speed towards the Earth.

Once the solar wind plasmas reach the Earth's space environment, it interacts with Earth's magnetic field. Considering that the fully ionized solar wind plasma consists only of charged particles, the Earth's magnetic field deflects the electrons to one side and the ions to the other. As charged particles get closer to the Earth, the magnetic field strength increases and at some point, the magnetic field strength is strong enough to deflect all charged particles. This area inside the boundary is called the magnetosphere, as seen in Figure 2.1(a). It should be noted that neutrally charged particles can still enter the magnetosphere.

At the boundary, electrons are separated from ions due to the negative charge. Electrons flow to one side and ions to the other, creating a current at the boundary. The magnetic field from the current sheet enhances the Earth's magnetic field inside the magnetosphere. In contrast, the magnetic field of the current outside the magnetosphere cancels the Earth's magnetic field and the boundary is called the magnetopause.

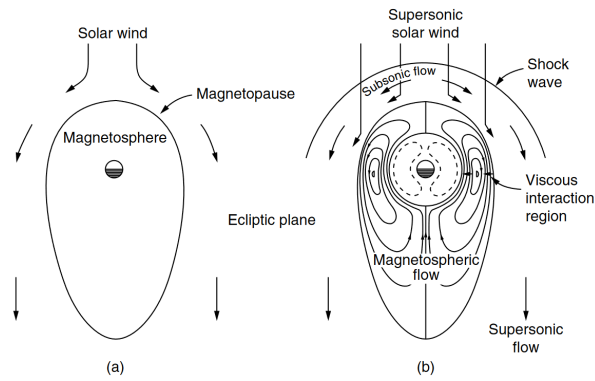


Figure 2.1: (a) Shows a schematic overview of the interaction between a subsonic solar wind plasma and Earth's magnetic field. (b) The more complex schematic overview is when the solar wind plasma has a supersonic speed.

However, [10] claims a shock wave must be present to decelerate the velocity of the solar wind plasma to a subsonic level. In the shock wave, the plasma density and temperature increase significantly due to the deceleration. As the magnetosphere is closed, no plasma is exchanged between the Earth's ionosphere and the solar wind plasma. Nevertheless, a weak coupling exists between the plasmas on the in- and outside, resulting in a plasma flow inside the magnetosphere. This is shown in Figure 2.1(b).

Until now, the energizing of particles is not considered; nevertheless, there is a significant difference between particle energy levels. [10] provides a brief explanation. In Table 2.1, the energy of charged particles in the Earth's space environment is presented. The solar wind electrons start at an energy of a few eV before being energized in the shock wave. Some energized electrons penetrate the Earth's ionosphere and collide with the natural gas present. This ionization contributes to the daytime auroras. At the magnetosphere's tail, due to the plasma flow inside the magnetosphere, electrons are accelerated from the tail towards the Earth. This region, called the plasma sheet, increases the electron energy to approximately a keV. These highly energized electrons contribute to the ionization of the natural gas in the Earth's atmosphere.

Table 2.1: The approximate energy levels of charged particles in the Earth's space environment [10].

Particle	Approximate Energy [eV]
Solar wind electrons	1 to 10
Shock wave electrons	10 to 100
Plasma sheet electrons	1000
Ions	1000

2.1.2. Satellite Orbits

With the knowledge that the space environment around Earth does not consist of a vacuum, it is time to look at the altitudes at which satellites operate. In this section, the orbits in which satellites reside are defined along with the particles present in these orbits.

Within this research, the orbits of the satellites are defined as presented in [11]. There are three distinct orbits, namely, LEO, Medium-Earth Orbit (MEO) and Geosynchronous Orbit (GEO), which are visualized in Figure 2.2. In Table 2.2, the altitude, revolution time and satellite occupancy are shown.

Some examples of satellites in LEO, MEO, GEO are respectively The International Space Station (ISS), the 24 satellites enabling the Global Positioning System (GPS) and Intelsat satellites used for broadcast services. Next, the conditions specific to the three distinct orbits are presented.

Low-Earth Orbit

Starting with the LEO environment that is quite extensively described by [10]. The temperature in the LEO varies significantly depending on the altitude, as shown in Figure 2.3a. In the stratosphere (10-90 km), the temperature increases with increasing altitude due to the photon absorption of the ozone



Figure 2.2: The figure shows the characterization of three orbits namely Low-Earth Orbit (LEO), Medium-Earth Orbit (MEO) and Geosynchronous Orbit (GEO) as given by [11].

Table 2.2: The characterization of the satellite orbits as presented by [11].

Orbit	Altitude [km]	Revolution around Earth [h]	Satellite occupancy
LEO	160-2000	1.5-2	55%
MEO	2000-35000	2-<24	10%
GEO	35786	24	35%

layer. Due to radiative cooling, the temperature suddenly drops at about 100 km altitude. A significant increase in temperature occurs at altitudes higher than 100 km as higher energy photons are absorbed.

Besides the temperature, the ionized gas density is also shown in Figure 2.3a. The ionized gas mainly originates from two processes.

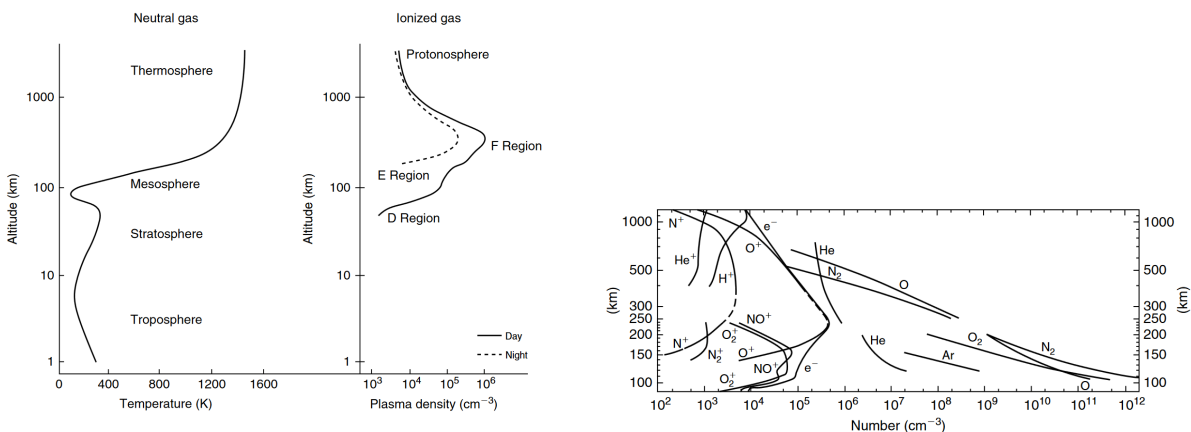
The first process is electron particle impact, which occurs mostly at higher latitudes and lower altitudes. In this process, high-energy electrons collide with neutral molecules, releasing an extra electron at impact. As a result, the molecule becomes positively charged, and an ion is formed. The auroras seen in the polar areas are a well-known phenomenon of the electron particle impact process.

The second process energizes the natural gas by EUV photons. When photons collide with a molecule, there is a chance the photon is absorbed. During the absorption, the electron energy is increased. If the increase in energy is sufficient, the electron is released from the molecule, and an ion is created.

Figure 2.3b shows the composition of particles in LEO. The four regions named D, E, F and protonosphere in Figure 2.3a are defined based on the dominant ions. An overview of the altitudes and dominant particles of the regions is shown in Table 2.3.

A noticeable difference between the E and F regions from Figure 2.3a is the absence of ionized gas in the E region at night. A change between day and night is expected as the primary ionization process is the energizing via EUV photons. However, at night, ionized gas in the F region hints at another mechanism.

The dominant ions within the regions can explain the difference. In the E and F regions, molecular



(a) The figure shows the temperature of neutral gas and the plasma density of ionized gas as a function of the altitude.

(b) The figure shows the atmosphere's composition at different altitudes.

Figure 2.3: Figures presented in [10] regarding the LEO environment.

and atomic ions are the most dominant ions. The molecular ions will fall apart in the recombination process, which is called dissociative recombination. In contrast, the recombination of atomic ions results in the release of a photon and is called radiative recombination. Since dissociative recombination is faster than radiative recombination, ionized gas density in the E region is reduced quickly at night.

Lastly, the ions in the protonosphere are mainly created via electron charge exchange between atomic oxygen from the F region and hydrogen and helium ions from the E region.

Table 2.3: The characterization of ionized gas regions observed in the LEO.

Region	Altitude [km]	Dominant ions
D	<90	-
E	90-150	NO ⁺ & O ₂ ⁺
F	150-500	O ⁺
Protonosphere	>600	H ⁺ & He ⁺

Medium-Earth Orbit & Geosynchronous Orbit

Next, the MEO environment is presented based on the Van Allen radiation belts. The Van Allen belts consist of an inner and outer belt spanning between distances of 1000 to 9600 km and 13 500 to 58 000 km from the Earth [12].

The Earth's magnetic field traps protons and electrons in the Van Allen belts. [13] extensively describes the origin of the particles. The protons are only present in the inner belt and are formed by the Cosmic Ray Albedo Neutron Decay (CRAND) process. The process describes the interaction of high-energy protons and alpha particles, known as Albedo particles, with neutrally charged particles in Earth's atmosphere. As a result of this interaction, protons lower energy protons are produced and trapped in the Earth's magnetic field.

In contrast, electrons are present in both the inner and outer belts. Generally, low-energy and high-energy electrons reside in the inner and outer belts, respectively. The sun mainly emits the highly energized electrons residing in the outer belt before being trapped.

In the inner belt, the origin of the electrons differs according to the energy levels. The high energy electrons (~ 1 MeV) are exchanged between the two belts. It should be noted that these exchange events do not occur often. Next, the lower energy electrons (<10 keV) are a byproduct of the CRAND process. Lastly, low-energy electrons are energized due to acceleration inside the magnetosphere, resulting in medium-energy electrons (10 to 100 keV). This energizing process is caused by acceleration and is called inward radial diffusion.

2.1.3. Effects on Satellites

With a basic understanding of the particles present in the space environments and the satellite orbits defined, the environmental effects on satellites are described in this section. A comprehensive study is presented in [14] where these effects on spacecraft are described per orbit. This section briefly summarises the impact on satellites, and the same structure is followed as presented in [14]. First, the effects in LEO are presented before moving on to the MEO and GEO.

Low-Earth Orbit

As mentioned, the CRAND process occurs in the LEO. As a result of CRAND, atomic oxygen is formed in the atmosphere. When satellites collide with the atomic oxygen particles, surface material erosion and chemical bond damage can occur.

In addition, the plasma in LEO influences transmitted signals as they get attenuated in the medium. Another effect of the plasma is the surface charging of satellites that can reach voltages of kilovolts.

Furthermore, the LEO is shielded by the magnetopause. Consequently, high-energy electrons are absent, and high-energy protons are mostly present. These high-energy protons penetrate the satellite's surface and influence electronic logic circuits. This effect is called the single-event effect.

Another source of damage to satellites is space debris. In the LEO space, debris is becoming a more pressing problem as the amount of debris increases. If a satellite collides with the debris, parts, especially the solar panels, can get damaged.

Lastly, the temperature in space varies significantly. When the atmosphere absorbs cosmic rays, heat is produced. Furthermore, the Earth radiates heat via infrared. Along with solar radiation, this

causes an increase in the satellite's temperature. In contrast, a satellite is cooled by radiation. As a result of these mechanisms, the satellite experiences temperatures between -100 to 93°C with rapid changes in temperatures. Damage may occur to materials due to thermal expansion or compression if the temperature changes quickly. Furthermore, electrical and other equipment should be designed to withstand the temperatures.

Medium-Earth Orbit & Geosynchronous Orbit

While, in principle, many effects from the LEO can be applied to the MEO and GEO, there are some differences. First, the MEO and GEO reside outside the protective magnetopause, resulting in solar wind plasmas. While these plasmas still cause erosion and damage, the surface charging effect significantly increases. This results in voltages up to hundreds of kilovolts.

Second, MEO resides in the outer Van Allen radiation belts with high-energy electrons. These electrons penetrate the satellite and cause internal charging of materials. Over long periods, exposure to high-energy electrons results in errors in electronic devices, which is called the total dose effect.

Third, the risk of damage due to debris is still present; however, it is at a lower risk compared to LEO. It should be noted that there is an increased risk of collisions with debris in GEO as more debris is present.

Lastly, the temperature in the MEO, and further away, is a bit lower compared to the LEO and between -175 to 25°C . While the temperature is lower, the temperature changes at a slower rate. This results in smaller risks due to thermal expansion.

In summary, the space environment around the Earth is not a complete vacuum, and particles are present. Charged particles are created or transferred to orbits around the Earth through various processes. While part of the charged particles are deflected by the Earth's magnetic field, resulting in a magnetosphere, some charged particles are created inside the magnetosphere. The charged particles can damage satellites by causing erosion of materials or charging the surface or the internals. Another challenging aspect is the temperature changes a satellite is subjected to and potential collisions with space debris.

To conclude, the space environment in the LEO, MEO and GEO is harsh. Special care and thoughts should be taken when setting the requirements for electrical designs meant for space, especially considering the operating temperatures and high voltage design.

2.2. Slip Ring Assembly Developments

Next, the current developments of SRA are presented to find shortcomings of the power transfer method. An example of a physical SRA is shown in Figure 2.4 along with a schematic overview. This section discusses the areas of active research regarding SRAs, including the understanding and improving the breakdown voltage, deep dielectric charging and improved manufacturing methods.

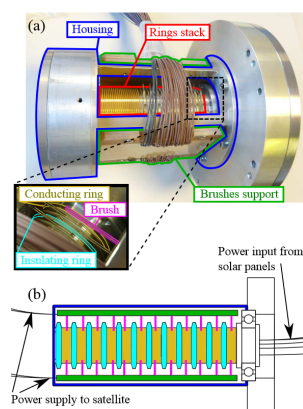


Figure 2.4: (a) Shows a slip ring with housing. (b) Shows a schematic overview of the slip ring assembly and the electrical connections. The images are presented in [9].

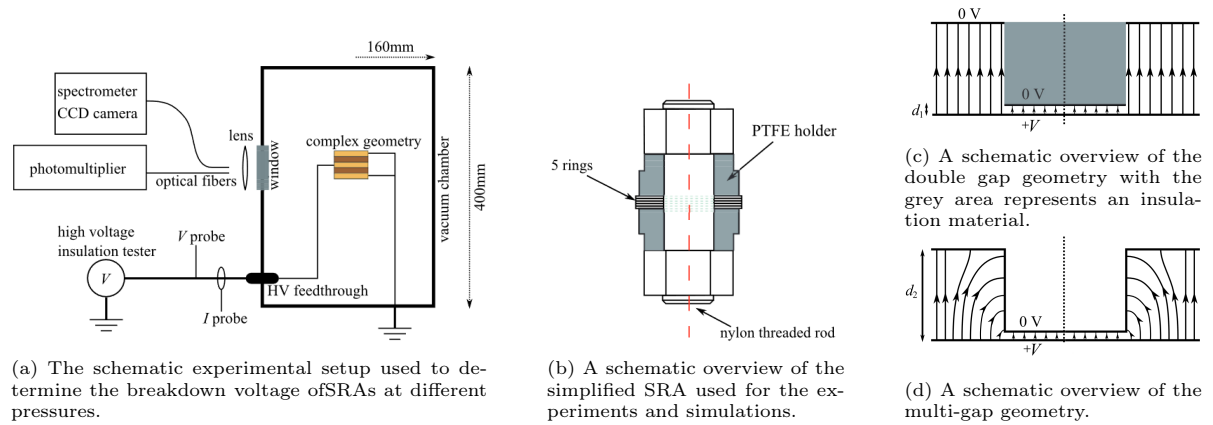


Figure 2.5: The above figures are schematic overviews presented by [15].

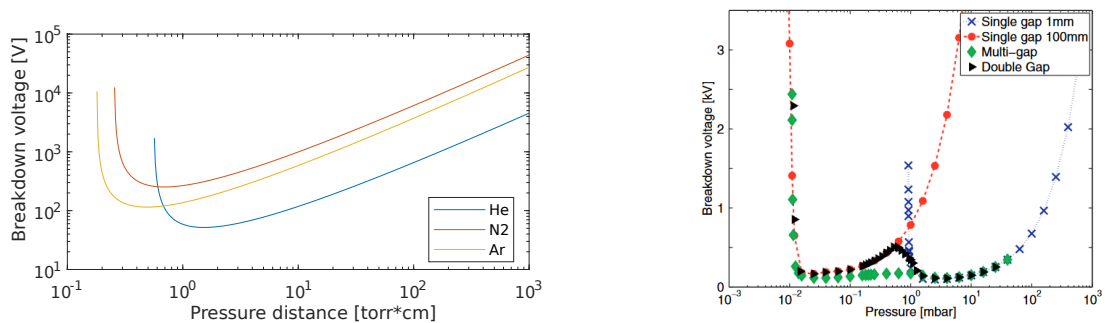
2.2.1. Breakdown Research

First, the research of breakdowns in SRAs is presented. This topic is actively researched as the breakdown in SRAs is a reason for the working voltage limit of the devices. With an understanding of the breakdown mechanism, mitigation factors can be incorporated into designs to improve the breakdown voltage and the working voltage limit.

[15] remarks that the breakdown mechanism is known for the plate-to-plate and pin-to-plate geometries; however, the analysis of complex geometries is missing. Schnyder *et al.* start with experiments to analyze the Direct Current (DC) breakdown of a SRA at varying pressures for different gases. Figure 2.5a shows the test-setup used by [15]. It should be noted that the tested geometry only consists of five rings and not a full SRA. The experimental results show two breakdown mechanisms, namely vacuum and gas breakdown at pressures below 10^{-3} mbar and above 10^{-2} mbar, respectively. The medium for the vacuum breakdown is provided by the surface of the electrodes as small metal parts and electrons are emitted and form a conductive path. Conversely, gas is the main medium for the breakdown instead of the electrodes in the gas breakdown. Both mechanisms are verified via spectroscopy in [15].

Next, [15] builds subsequent numerical models for the following geometries: the plate-to-plate, double gap, multi-gap and slip assembly. Figures 2.5b to 2.5d respectively show the double gap, multi-gap and SRA schematical overviews.

The Paschen curve is introduced before continuing with the results of the numerical models. The Paschen law describes two voltage breakdown mechanisms: the electron impact ionization and secondary emission [16]. In short, the electron impact ionization process describes the release of electrons and ions from neutrally charged molecules through impact. The secondary emission mechanism describes the effect where electrons are released from the cathode. The Paschen curve is obtained by mathematically combining the two previously mentioned mechanisms. By looking at the Paschen curve, in Figure 2.6a, it can be seen that for a given distance, the breakdown voltage rises to infinity as the pressure decreases.



(a) The breakdown voltage of helium, argon and a mixture of nitrogen and air as a function of the pressure distances from [17].

(b) The figure above shows the simulated breakdown voltage at different pressures for the 1mm, 100mm single gap, double gap and multi-gap. The figure is obtained from [15].

Figure 2.6: The relation between the breakdown voltage and the pressure distance and the pressure.

Starting with the results, the plate-to-plate model is compared to the Paschen curve and shows good correspondence, validating the model for the gas breakdown. Second, the double gap geometry, shown in Figure 2.5c, was simulated. From the simulations, shown in Figure 2.6b, it can be seen that the breakdown voltage of the double gap geometry is a combination of the 1 mm and 100 mm single gap breakdown curves. The breakdown curve shifts towards lower pressures by increasing the gap between the electrodes. This is because the Paschen curve, see Figure 2.6a, uses the pressure distance as the input variable.

Third, the multi-gap geometry is simulated with the numerical model and the results are again shown in Figure 2.6b. A low breakdown voltage is observed over a large pressure range for the multi-gap geometry. [15] observes that in the multi-gap geometry, every gap distance between 1 mm and 100 mm is present, see Figure 2.5d. As a result, the multi-gap breakdown curve combines all the breakdown curves between 1 to 100 mm, where all the lowest breakdown voltages are taken. Thus explaining the low breakdown voltage over a large pressure range.

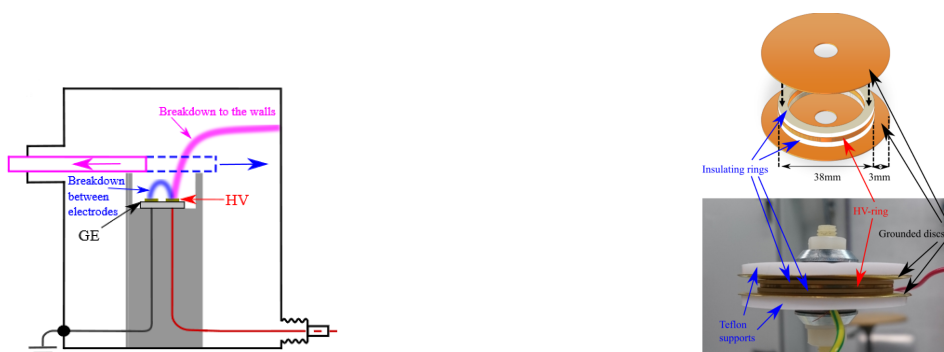
Lastly, the experimental and numerical results for the ring assembly are compared. Unfortunately, the numerical data showed significantly higher and lower breakdown voltage at lower and higher pressures, respectively, compared to the experimental data. According to [15], the simulation parameters are given as a reason for the difference between the simulation and experimental data.

Similarly to Schnyder *et al.*, the research of [9] begins with understanding the breakdown mechanism of a simple geometry in a vacuum chamber. The goal of [9] and [18] is to increase the breakdown voltage of SRAs to a minimum of 600 V such that the SRAs are ready for satellites with new High Voltage (HV) buses.

Starting with the experimental setup to determine gas breakdown voltage at different pressures, as seen in Figure 2.7a. First, a reference test is performed, where the lid of the electrodes is open, and the negative electrode is grounded. Second, the negative electrode is left floating. Lastly, the negative electrode is grounded again, and the lid is closed over the electrodes.

Two breakdown paths are observed from the experimental results conducted in [9]. In the low- (0.3 mbar) and high-pressure region (0.3 mbar) the breakdown occurs respectively between the HV electrode and the vacuum chamber wall and between the HV and grounded electrode, as shown by [9] in Figure 2.7a. Firstly, the low-pressure region breakdown voltage is increased by adding grounded discs to the ends of the HV slip ring, as shown in Figure 2.7b. These grounding discs act as partial Faraday screens, significantly increasing the breakdown voltage at pressures below 1 mbar. However, the breakdown voltage above a pressure of 1 mbar is decreased compared to the no-disc assembly.

Secondly, the work of [9] is continued in [18], where the focus is shifted to increasing the breakdown voltage in the high-pressure region. The same assembly, with discs on the sides, is used, but the discs are not grounded. Instead, the discs are connected to a voltage divider between the HV electrode and ground. Decreasing the voltage between the disc and HV electrode increases the breakdown voltage in the high-pressure region. Unfortunately, due to the potential on the discs, part of the Faraday screen effect is reduced. Thus reducing the breakdown voltage in the low-pressure region. It should be noted that even though the breakdown voltage in the low-pressure region is decreased, it still is increased compared to a no-disc assembly.



(a) A schematical overview of the test setup used by [9] to determine the breakdown voltage of gas at different pressures.

(b) The top figure shows the schematic basic assembly with grounding discs as presented in [9]. The bottom figure shows the realized assembly.

Figure 2.7: The figures above are taken from [9] and show the gas breakdown setup and designed SRA.

2.2.2. Deep Dielectric Charging

As mentioned before, high-energy electrons can penetrate the hull of satellites. The sun emits these electrons in solar wind plasmas, and sometimes these events can last hours [8]. If the electrons penetrate the shell, they are deposited onto the SRA material. The deposited electrons on the grounded conductive parts are quickly released. Nevertheless, the dielectric parts of the SRA are unable to release the electrons rapidly, resulting in a charge buildup and eventually ESD. This deep dielectric charging phenomenon accounts for 54% of spacecraft failures [8].

To combat the deep dielectric charging of the SRA, Wang *et al.* developed three solutions, as seen in Figure 2.8, to reduce the electric field potential due to charge accumulation. The solutions were found after studying simulations of a 3D SRA in COMSOL. Next, the solutions and their effects on the deep dielectric charging are explained.

- Locally strengthening the aluminium shell** The accumulation of electrons is largest at the top of the substrate baffle. Therefore, the aluminium shell is reinforced above the baffle, as seen in Figure 2.8a, to reduce the penetration of electrons. To keep the weight of the aluminium shell constant, the shape is optimized by taking the extra weight from the aluminium above the copper slip rings and adding it to the locally reinforced parts. A reduction of 20% was achieved for the maximum electric field.
- Grooved baffle structure** From the simulation, the electron accumulation gradually decreased from the substrate's top to bottom. To reduce the accumulated electrons, the height of the substrate is decreased. Nonetheless, by reducing the height of the substrate, the creepage distance between conductors is also decreased, increasing the risk of surface breakdown, especially for future high-voltage SRA. The U-shaped baffle, see Figure 2.8b, is introduced to maintain and even increase the creepage distance. The reduction in electric field potential was 25%.
- Grounding structure** The contact area between the dielectric substrate and the copper rings is minimal and sharp. Consequently, the current density is mostly located at the junction of the substrate, copper and air. To improve the contact area, the copper is embedded into the dielectric with a radial fillet, see Figure 2.8c. As a result, the conduction current was distributed more evenly, and the electric field potential was reduced by 48.6%.

Combining the three SRA optimizations, an electric field potential reduction of 70% was achieved. A final note from Wang *et al.* highlights the potential dangers of debris due to the wear of the brushes and copper rings. The debris accumulates locally due to the electrostatic forces. As a result, the electric field is distorted and ESD or arcs can take place.

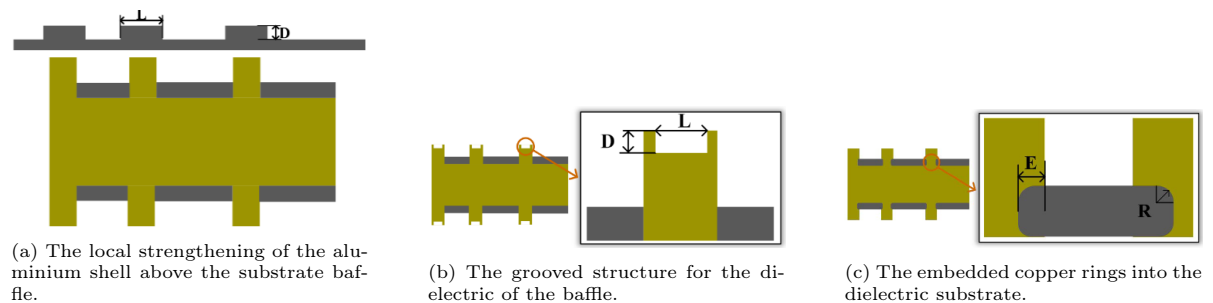


Figure 2.8: The optimization solutions presented in [8] to reduce the deep dielectric charging in an SRA.

2.2.3. Manufacturing

This subsection presents developments in the manufacturing process of SRAs. First, Additive Manufacturing (AM) is introduced to improve the manufacturing of the SRA hull before a design is introduced to improve the alignment of brushes and slip rings in SRA.

A novel AM is introduced for the manufacturing of SRAs [19]. While manufacturing a SRA, many rings are stacked on top of each other. The total deviation for the complete SRA is increased significantly compared to the manufacturing tolerances of the rings and associated components. To alleviate this

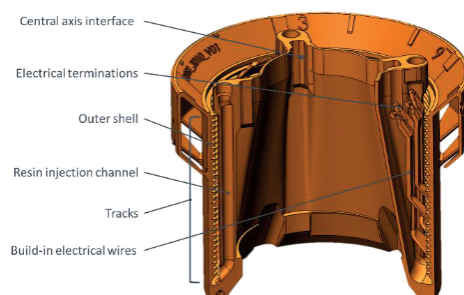


Figure 2.9: The monolithic hull design for additive manufacturing as presented in [19].

problem, AM is introduced to produce a monolithic structure shown in Figure 2.9. The outside of the structure is plated with conductive metals, which are connected to build-in wires. Another benefit of the hull structure is, therefore, the reduction in number of components. It should be noted that structural tests still need to be performed to validate their suitability for use in spacecraft.

Another sensitive manufacturing process is the alignment of the brushes and the slip rings of an SRA. Misalignment of the brushes increases the resistance, reduces the lifetime of the SRA and may lead to short-circuit faults [20]. To improve the alignment of the brushes Chen *et al.* propose a vision-aided brush assembly design. With the continuing improvement of cameras and image processing, a camera and lens are used to enhance the SRA process. With the help of image processing, the misalignment is directly calculated during assembly and can be corrected. As a direct consequence of the vision-aided brush alignment assembly system, the alignment accuracy was kept within ± 0.02 mm.

To summarize, the development field of SRAs is still very active. The research aims to improve the breakdown voltage, reduce deep dielectric charging and decrease the dependency on manufacturing tolerances. However, it should be noted that improving the breakdown voltage removes both the low and high-pressure regions, which is a balancing act. Therefore, estimating how far the working voltage limit of a SRA can be pushed is difficult. In addition, the alignment improvement in the manufacturing process increases the lifetime but does not remove the wear of the brushes.

2.3. Wireless Power Transfer Developments

This research aims to develop a novel and improved CET system for satellite or space applications. Therefore, the current state-of-the-art research developments are presented in this section.

The summary of the theoretical design state-of-the-art starts with the work of Deceuleneer [21]. For his thesis at the KU Leuven University, Deceuleneer studied the Solar Array Drive Assembly (SADA) of satellites. From a concise comparison of slip rings, IPT and CPT, Deceuleneer concluded that IPT offered the most potential based on higher working voltage, Tri-port and battery charge and discharge regulator functionality. Furthermore, the IPT system should be able to compete with the slip rings regarding power transfer and efficiency.

Moving on to the specifications of the IPT system, the most important design requirements of the rotary transformer are shown in Table 2.4. After a brief comparison, the geometry, shown in Figure 2.10a, was chosen for the IPT system. The mentioned benefits of this geometry are:

- A large overlap between the windings and the core for thermal management.
- The air gap is in the axial direction and should suffer less from thermal expansions than a radial air gap.
- An axial gap allows for a small air gap, resulting in higher efficiencies.
- Coaxial windings and small window height (L_4) are beneficial for the proximity effect.

To drive and control the output of the transformer, a DAB is used in the IPT system. This DAB consists of a H-bridge on both the primary and secondary sides. Even though using a DAB increases the number of components used in the design, it also allows for the control of input and output current compared to a passive solution such as a full-bridge rectifier. Two benefits of the DAB architecture are

Table 2.4: The design requirements of the IPT system from [21].

Requirement	Value
Rated power	10 kW
Input voltage	300 V
Total efficiency	>98%

that the primary side converter functions as the Maximum Power Point Tracker (MPPT) for the solar panels, and the secondary converter controls the charging and discharging of the battery.

The DAB is driven using phase-shift angle control where the phase-shift is regarded between the in- and output bridges. After a per-unit analysis, a rated phase-shift angle is determined to minimize the apparent power needed. From the switching frequency, the rated phase-shift angle, in- and output voltage and power rating, required series inductance is determined for the case where an ideal transformer is used. The resulting value turned out to be too large, to achieve with the leakage inductance of a real transformer. Therefore, an external inductor is introduced.

Next, a model is constructed of the transformer to estimate the losses based on design parameters such as current density (J), number of turns (n), switching frequency (f), peak flux density (\hat{B}) and winding window factor (k_g). These parameters are also the inputs for the optimization model to size the transformer using two optimization functions. The first function is the total losses of the transformer, composed of copper and core losses, and the second function computes the weight of the transformer.

After the transformer was optimized, an attempt was made to create a prototype. Unfortunately, off-the-shelf ferrite pot cores could not be used as the dimensions of the transformer were too large. As a result, the core pieces were manufactured using water jetting; however, some ferrite core pieces broke in the process. Thus, no functional prototype was realized.

In contrast, the external inductor is designed around an off-the-shelf E-core. Based on the core geometry and the reluctance model, the required air gap is determined before the external inductor's losses are determined.

Ultimately, the final theoretical design had a power loss of 41.5 W and 27 W for the transformer and external inductor, respectively. Together with the estimated losses of 100 W from the DAB, the total losses of the IPT system was 170 W, thus achieving the desired efficiency of >98%.

Another area of research with SADA systems of satellites is the improvement of redundancy in the power transfer system. Wang *et al.* present a IPT theoretical design with three coils on both the primary and secondary side, as seen in Figure 2.10b, with the capability of transferring 5 kW of power. This design should replace slip rings in SADA to improve the lifetime and reliability besides the built-in redundancy. Through the position of the coils, the mutual coupling between same-sided coils is almost eliminated. With the help of ANSYS, the mutual coupling between the primary and secondary sides remained constant during rotation. Even when a fault occurs at a coil at the primary or secondary side, the IPT system can operate in a derating state with 2.2 kW output power.

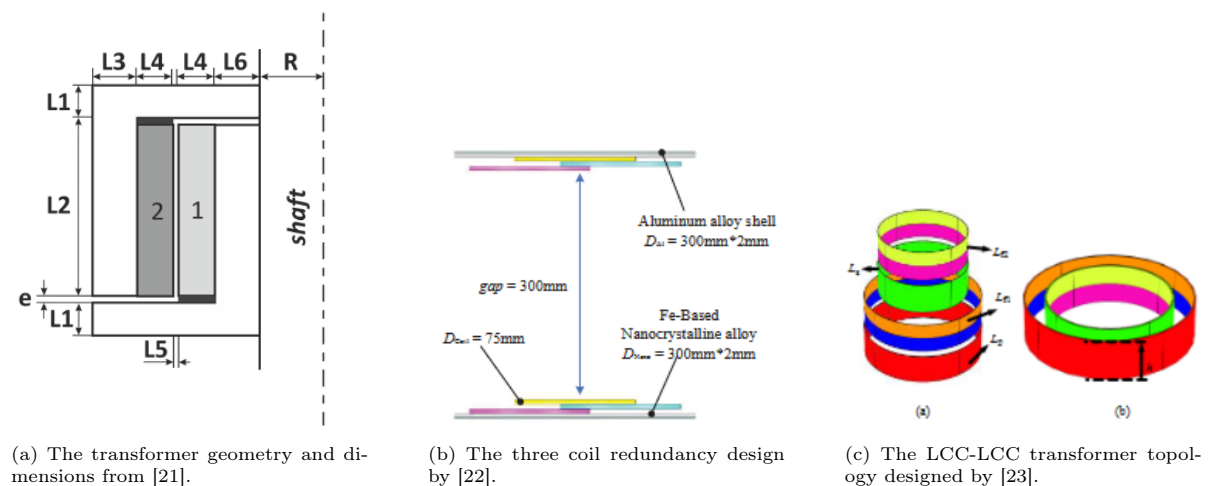


Figure 2.10: State-of-the-art theoretical transformer models for satellite applications.

Interestingly, Wang *et al.* chose a nanocrystalline alloy for the core instead of the traditional Mn-Zn ferrite material. This choice was mostly made to improve the saturation margin and reduce the weight and size of the core. It should be noted that no prototype was realized in the presented work. All results were obtained from simulation software such as ANSYS and analytical methods. Therefore, it is uncertain if a prototype reaches the stated coupling device efficiency of 95.1%.

A way to increase the throughput capability of the IPT system for space applications is presented by [23]. Again, a different type of transformer is designed. In Figure 2.10c, a transformer with two unipolar and two bipolar solenoid coils is shown. Both the primary and secondary sides have a uni- and bipolar coil. In addition, there are two compensation capacitors added on the primary and secondary side. As a result, this compensation network is called an LCC-LCC compensation with dual coil pair topology.

A bipolar coil consists of a forward and reverse-wound coil and could be seen as two unipolar coils. When a magnetic field originating from a unipolar coil passes through the bipolar coil, one side generates an induced voltage. In contrast, the other side generates a voltage of the opposite sign. Therefore, the total induced voltage is zero, and no coupling is observed. However, if a magnetic field is generated and received by two bipolar coils, the two induced voltages in the forward and reverse windings do not compensate each other but add up. As a result, only two mutual inductances are significant, namely the coupling between the two main unipolar coils and between the two bipolar coils.

The dual coil pair topology significantly increases output capability and load dependency compared to a single coil pair LCC-LCC topology. Furthermore, the theoretical design transferred a power of 258 W.

In summary, multiple WPT designs are already present in literature with various research focuses. [21] presents a comprehensive design report with a focus on decreasing losses as well as with weight and size, while [22] focuses on introducing redundancy to improve reliability. Lastly, [23] aims to increase the throughput of IPT systems while minimizing the increase in transfer device size. These three articles indicate the active development of IPT systems aimed at satellites. However, the three designs presented in this section did not produce functional prototypes, so the real-life power losses and efficiencies remain unknown.

3

System Design

This chapter presents the system design of the CET system. However, before the system is introduced, the design requirements are discussed.

As mentioned in the previous chapter, [18] highlights the need to increase the working voltage in satellites to power new systems onboard. Furthermore, [21] indicates that the working voltage is limited to $V = 110\text{ V}$ for most spacecraft due to the SRA. To showcase the advantage of a CET system, the output voltage of the system should be higher than 110 V .

In addition, [21] points out that the efficiency of SRAs is generally 98%. Thus, the system efficiency should be similar for the CET system to be competitive.

Next to the efficiency, the transferred power needs to be specified. The limiting factor for this parameter is the equipment available in the Electrical Sustainable Power (ESP) from the TU Delft. Therefore, the power transfer is set to $P = 3\text{ kW}$.

Lastly, as mentioned in the introduction, the weight of the CET system is vital in relation to the cost of the satellite. Furthermore, the available space in a satellite is limited. Thus, the requirement for the size of the CET system is to be as small as possible.

To conclude, Table 3.1 presents the general requirements for the CET system. More design requirements for specific subsystems are introduced later in the dedicated sections and chapters.

Table 3.1: The system requirements for the CET system.

Requirement	Value
Output voltage (V_{out})	300 V
Power (P)	3 kW
Total efficiency (η)	$\geq 98\%$

A general overview of the CET system is shown in Figure 3.1. In Section 3.1, the input source based on the solar panels is defined. Next, the capacitive and inductive transfer methods for the AC-link are discussed in Section 3.2. The converter topology considerations are presented in Section 3.3 where the combined behaviour of the inverter, rectifier and the AC-link is considered. Lastly, the chapter is concluded by defining the transformer geometry in Section 3.4.



Figure 3.1: Generic architecture of a Contactless Energy Transfer system with solar power as input.

3.1. Input Source

The section starts with introducing the solar cell used in this project. Afterwards, the solar cell is modelled based on the values provided in the datasheet. Next, an array structure is designed to meet

the voltage, current and power requirements of the CET system. Lastly, the characteristics of the scaled solar input source are presented.

3.1.1. General Solar Panel info

In recent years, the use of solar panels has seen an astronomic rise in the private and industry sectors. [24] cites government subsidies as the main reason for the significant solar panel demand. As a result of the increase in demand and maturing of the production process between 2010 and 2015, the price of solar panels decreased by 75%

Consequently, the technology has matured rapidly, and performance keeps increasing while cost decreases. As solar panels are an essential energy source for the space industry, these companies benefit from these developments. However, solar panels used in space are designed with stricter requirements than those destined to operate on Earth's surface.

As discussed in Section 2.1.3, space environment plasmas can lead to material erosion and damage if they collide with satellites. In addition, the solar panel surfaces are charged by the plasma. As a result, arcing on the solar panel may result in damage.

Furthermore, solar panels exposed to high-energy radiation suffer performance degradation over time. The high-energy particles from the radiation can displace atoms from the lattice during a collision with the solar panel. This process is called displacement damage and decreases the efficiency of solar panels during their lifetime. Developments are ongoing to combat the displacement damage by ensuring End of life (EOL) efficiency for space solar panels [25].

Azur Space is a solar cell manufacturer for telecommunication organizations and other space organizations such as National Aeronautics and Space Administration (NASA) and European Space Agency (ESA). They are among the leading companies in the production of multi-junction solar cells. Their solar cells power the Hubble telescope and many Intelsat communication satellites [26] with efficiencies up to 30%

As the solar cells produced by AZUR SPACE are state-of-the-art within the space industry, they are used as the energy source in this research. To be more specific, the 3G30C-Advanced solar cells are used.

3.1.2. Solar Cell

Before the design of the WPT system can start, it is essential to understand the characteristics of the input source. Especially the relation between the voltage, current and power the input source can deliver. This section presents a model for the 3G30 solar cells that will act as a simplified input source to the CET system.

First, the available data from the datasheet of the 3G30C-Advanced solar cell is presented in Table 3.2. The given values indicate the current and voltage limits of the solar cell via the short circuit current I_{sc} and the open circuit voltage V_{oc} , respectively. Furthermore, the maximum power can be estimated with the voltage and current at the maximum power point, V_{mp} and I_{mp} , respectively.

Table 3.2: The specification for the 3G30-Advanced solar cell from AZUR SPACE [27]. I_{sc} and I_{mp} are the short circuit and maximum power current respectively. V_{oc} and V_{mp} are the open circuit and maximum power voltage respectively.

Parameter	I_{sc} [mA]	V_{oc} [mV]	I_{mp} [mA]	V_{mp} [mV]	η [%]
Value	457	2700	442.8	2411	29.5

A simple one-diode model is presented in [28] and shown in Figure 3.2a. In the figure, the following quantities are present: I_{ph} is the photocurrent, I_d the diode current, I_{sh} the shunt current, R_{sh} the shunt resistance and R_s the series resistance.

The above quantities are related to each other according to Equations (3.1) to (3.4). In the equations, k is the Boltzmann constant, T temperature, q the electron charge, n_s the number of series connected cells and n the diode quality factor.

$$i = I_{ph} - I_d - I_{sh} \quad (3.1)$$

$$I_{sh} = \frac{v + iR_s}{R_{sh}} \quad (3.2)$$

$$I_d = I_0 \left(\exp \left[\frac{v + iR_s}{n_s n V_t} \right] - 1 \right) \quad (3.3)$$

$$V_t = \frac{kT}{q} \quad (3.4)$$

Equation (3.1) is nonlinear; therefore, a purely analytical solution is difficult to achieve, especially with unknown parameters. [28] presents a numerical method to obtain all the parameters for the model; however, the complexity of this method exceeds the goal of this research. A general behaviour of the solar cell is sufficient to determine the operating constraints for the WPT system.

Assuming that the solar cell has a no series resistance R_s , the model becomes linear, and the new relations between the parameters are shown in Equations (3.5) and (3.6) and the general solar cell behaviour is shown in Figure 3.2b.

$$I_{sh} = \frac{v}{R_{sh}} \quad (3.5)$$

$$I_d = I_0 \left(\exp \left[\frac{v}{n_s n V_t} \right] - 1 \right) \quad (3.6)$$

Parameter estimation

Next, the unknown parameters of the diode model need to be linked to the values provided in the datasheet. For this analysis, the diode quality factor is assumed to be $n = 1$, and only a single cell is used $n_s = 1$. This leaves the parameters I_{ph} , I_0 and R_{sh} as unknowns.

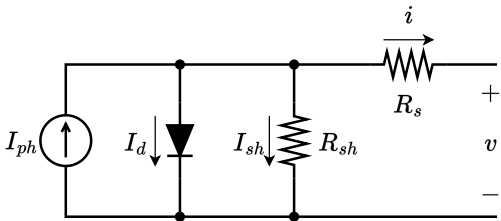
Starting with the photocurrent I_{ph} . When the voltage is zero, the diode and shunt current are zero, and the photocurrent remains. Within the datasheet, a short circuit current is provided at zero voltage. Thus, for the model, the short circuit current equals the photocurrent $I_{sc} = I_{ph}$.

Moving on, from the datasheet, two more points on the current-voltage curve (IV-curve) are present. Namely, the current and voltage are at maximum power, and the open circuit voltage is where the output current is zero. As only two parameters, R_{sh} and I_0 , remain unknown, they can be expressed by Equations (3.1), (3.5) and (3.6) and the datasheet points.

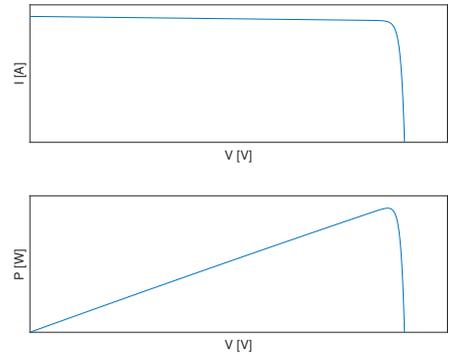
First, at the open circuit voltage, the output current is zero. As a result, the photocurrent is equal to the sum of the diode and shunt current, as shown in Equation (3.7). From this equation, the dark saturation current I_0 is expressed in known terms and R_{sh} , see Equation (3.8).

$$I_{ph} = I_d + I_{sh} = I_0 \left(\exp \left[\frac{v}{n_s n V_t} \right] - 1 \right) + \frac{v}{R_{sh}} \quad (3.7)$$

$$I_0 = \frac{I_{ph} - \frac{V_{oc}}{R_{sh}}}{\exp \left[\frac{V_{oc}}{V_t} \right] - 1} \quad (3.8)$$



(a) The single diode model to approximate the electrical behaviour of solar panels.



(b) Above the current-voltage and below power voltage curves.

Figure 3.2: The solar cell model and characteristics.

Second, the maximum power point is evaluated in the model using the expression derived for I_0 . Solving the resulting equation for the shunt resistance leads to Equations (3.9) and (3.10).

$$R_{sh} = \frac{aV_{oc} - V_{mp}}{i_{imp} + I_{ph}(a - 1)} \quad (3.9)$$

$$a = \frac{\exp\left[\frac{V_{mp}}{V_t}\right] - 1}{\exp\left[\frac{V_{oc}}{V_t}\right] - 1} \quad (3.10)$$

Now that the unknown parameters are expressed in terms of values provided by the datasheet, the solar cell model is established. The resulting model parameters are shown in Table 3.3.

Table 3.3: The estimated model parameters for the 3G30-Advanced solar cell from AZUR SPACE [27].

Parameter	I_0 [A]	I_{ph} [mA]	R_{sh} [Ω]
Value	$2.77 \cdot 10^{-46}$	457	169.87

The last part of the analysis compares the model and the datasheet values. The model's voltage, current and power characteristics are shown in Figure 3.3 and show the expected behaviour of a solar cell.

Next, the performance numbers are shown in Table 3.4. From the table, it can be seen that the maximum power point is shifted to a higher voltage. While the current is lower at the maximum power point, the maximum power of the model is higher compared to the datasheet.

The solar cell operating limits are modelled correctly, as the open circuit voltage and short circuit current values correspond between the model and the datasheet.

Table 3.4: The solar cell performance characteristics from the datasheet and the estimated model.

Parameter	Datasheet	Model
I_{sc} [mA]	457	457
V_{oc} [V]	2.7	2.7
I_{mp} [mA]	442.8	437.5
V_{mp} [V]	2.411	2.58
P_{max} [W]	1.06	1.13

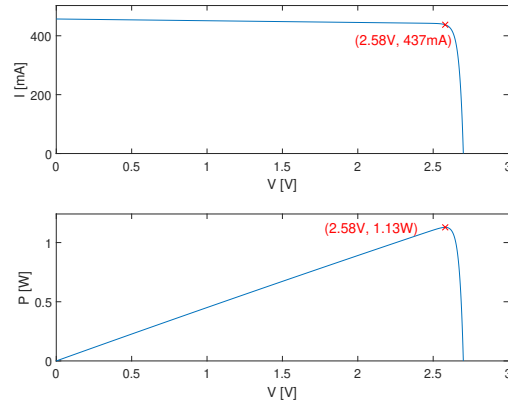


Figure 3.3: The solar cell model current and power characteristics versus voltage with parameters from Table 3.3. The maximum power point is highlighted with the red cross.

Arrangement of Solar Cells

The model presented in the previous section provides a power of approximately a single watt at a voltage of 2.5 V. These numbers do not correspond with the power required on most satellites. Therefore, a solar cell structure must be developed to ensure the energy source provides the satellite with enough power.

Luckily, solar cells or panels are scaled easily by connecting them in parallel or series. The output voltage of the solar cell structure is determined by the number of cells connected in a series n_s , called a string. Assuming all cells behave identically, the output voltage is obtained by multiplying the single cell voltage with n_s .

A similar approach is followed for the total output current of the solar cell structure. The same current flows through all cells in a single string as in a single solar cell. Therefore, the total output

current equals the multiplication of the number of strings connected in parallel n_p and the single cell current.

As a result, the structure of the energy source is a grid of solar cells of n_s by n_p . The sizing of the energy source is based on the satellite requirements and the characteristics of the solar cell model. For repetition, the satellite power is $P_{sat} = 3\text{ kW}$ at approximately a $V_{sat} = 300\text{ V}$.

Using the power obtained from the model of a single solar cell, the minimum amount of solar cells required to meet the satellite power requirement is calculated to be $n_{cells,min} = 2658$. Furthermore, for this research, the current is limited to $I_{max} = 10\text{ A}$ to restrict the size of the Litz wire required. Based on the short circuit current of the solar cell model, the maximum amount strings is $n_{p,max} = 21$. As a result, the amount of series connected cells is $n_s = 127$.

The energy source structure is defined with n_s and n_p known. The final specifications and characteristics of the energy source are presented in the next section of this chapter.

3.1.3. Input source to CET

In summary, this chapter introduces the solar cells used in the space industry. A single diode model is created to understand solar cell behaviour. The parameters for the model are estimated based on the solar cell datasheet. Lastly, a grid structure of solar cells is created to meet the satellite power requirement.

In conclusion, the satellite's input source for this research is defined. The resulting electrical behaviour of the energy source is shown in Figure 3.4 along with the essential characteristics in Table 3.5.

Table 3.5: The solar cell structure characteristics used as the energy source in this research.

Parameter	Value
n_s	127
n_p	21
V_{max}	342.9 V
I_{max}	9.60 A
P_{max}	3010 W
V_{mp}	327.7 V
I_{mp}	9.19 A

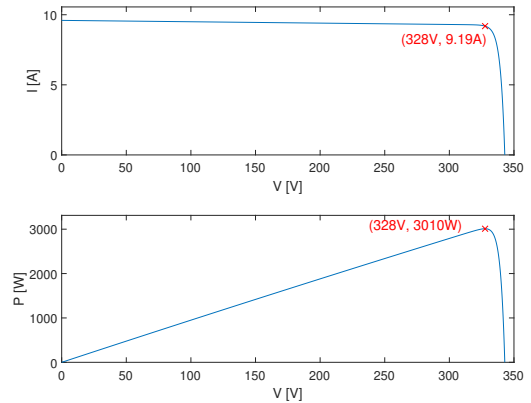


Figure 3.4: The current and power versus voltage curves of the energy source used in this research.

3.2. Capacitive vs Inductive Power Transfer

This section aims to define the method of power transfer for the CET system. Both a capacitive and inductive power transfer are considered. The power transfer method is discussed before the converter topology, as the resulting choice influences the electrical components used in the conversion process.

A short comparative study is performed to establish the best choice between CPT and IPT for the AC-link. This study introduces and compares results from experimental AC-link prototypes found in the literature. Afterwards, the implications of the chosen power transfer method regarding the AC-link structure and converter topology are briefly introduced.

It should be noted that these prototypes are not designed for satellite applications but rather for Electric Machines (EMs). Nevertheless, the CET principle from stator to rotor in a EM is similar to satellites. Therefore, comparing the prototypes provides valuable insights into the AC-link.

3.2.1. Comparative Study

In this subsection, first, the similarities and second, the differences between the CPT and IPT are introduced. Third and last, the two power transfer methods are compared, and the most promising method is chosen based on efficiency, power throughput, and power density.

The first similarity between both IPT and CPT is the system architecture. The generic CET system architecture, shown in Figure 3.1 at the beginning of this chapter, is valid for both transfer methods. While the specifications of the blocks connected to the AC-link may differ between the methods, the functions of the blocks are equal.

The second similarity is the use of AC current within the AC-link for both systems. Thus, both systems require an inverter connected to the main power source. Due to the AC power transfer, a rectifier is needed on the secondary side to convert the power back to DC. Next, the main differences between the two AC-links are highlighted based on prototypes found in the literature.

First, the field used for the energy transfer differs between IPT and CPT since the magnetic and electric fields are used, respectively. For the IPT, the AC-link is often a transformer or rotary transformer, depending on the application. Here, a core material is usually used to help guide the magnetic field lines and increase the power capabilities as seen in [29]–[34]. However, it is unnecessary, as shown by [35]. Within the papers cited before, different shapes and sizes are presented to meet the specific power requirements and available space. For the CPT, capacitors are constructed as AC-links. Here, air is an option as the main dielectric [36] or if the capacitor forms a sealed enclosure, a dielectric lubricant can be used [37].

Second, there is a difference between the CPT and IPT operating frequency when a core material is used. As seen from Table 3.6, the operating frequency of IPT systems with a core lies between 20 to 120 kHz. The prototype of [35] does not use a core material and uses a significantly higher operating frequency to achieve the power transfer. This operating frequency is more in line with the frequencies used by the CPT prototypes. A benefit of the higher operating frequency is the reduced reactive component size and, therefore, the overall system size. However, special care must be given to the design of the inverter not to increase the switching losses to obtain a higher operating frequency.

The third difference is the power capability. From Table 3.6, it is clear that the IPT systems can achieve a higher power capability compared to the CPT systems. Furthermore, it can be seen that the efficiency of the IPT systems is generally higher than the CPT systems even at higher power. Thus, it is a safe assumption that the IPT systems are more efficient compared to the CPT systems, even if the IPT systems are designed for lower power requirements.

Fourth and last, the power density of the two methods is compared. The power density is an important aspect when comparing IPT with CPT since often there is limited space available for the CET system on satellites. The outer dimensions of the AC-link are taken to determine the power density of the different prototypes. Next, the efficiency is used to determine the available output power and the power density. The results are shown in Table 3.6, and it can be concluded that the power density of the IPT prototypes is significantly higher compared to the CPT prototypes.

Table 3.6: Specifications for different CET prototypes designed for EM

Design	Coupling	Operating frequency [kHz]	Power [W]	Efficiency	Power density [kW/m ³]
Ludios [36]	CPT	626	6.5	94%	12.4
Dai [37]	CPT	700-1000	340	85%	533
Littau [32]	IPT	20	1000	97.6%	2240
Krupp [33]	IPT	120	400	-	3020
Vip [34]	IPT	100	1000	96.3%	2950
Stancu [30]	IPT	100	5000	95%	2120
Sun [35]	IPT	1000	400	-	3710
Zhang [29]	IPT	25	1000	90%	46.3

Thus, based on the above observations, IPT has a higher power density, capability and efficiency than CPT. In this research, the AC-link needs to transfer a power of 3 kW, and the dimensions are limited on satellite. Thus, IPT is chosen as the AC-link method with the most potential for this research.

3.2.2. IPT Choice Implications on System Design

The selection of the IPT method has an impact on the overall CET system design and the structure of the AC-link. First, the IPT method requires an inductive circuit element to transfer power. In this research, a CET system is needed; therefore, a transformer is considered. A transformer offers a

magnetic link between two coils that are physically not connected. As a result, the primary coil can be connected to the solar panel input source and the secondary coil to the satellite power system, which is considered the load.

Second, the transformer's primary and secondary coils both provide a self-inductance and, together, a mutual inductance due to their coupling. In addition, the number of turns for primary and secondary coils influences the transformer's voltage and current transfer. The inductances and number of turns need to be considered when evaluating the system behaviour of the CET system with a transformer.

Therefore, in the next section, different converter topologies with inductive components are introduced and compared to determine the most suitable topology for the CET system. Afterwards, the transformer geometry is refined in Section 3.4.

3.3. Converter Topology Considerations

After analyzing the input source and choosing the IPT method for the AC-link, this section investigates the conversion process from a system level. In this investigation, the primary side inverter considerations are presented first. Second, the secondary rectification options are introduced. Third, the conversion topology as a whole is investigated, including the inverter, rectification and the AC-link. Multiple converter topologies are introduced and compared. Before moving on, the requirements for the conversion system are defined.

In Section 3.1, the input source and its characteristics are defined. The input voltage depends on the power drawn from the input source and can range from zero to $V_{in,max}$. By recalling that the CET system is connected to a battery, the output voltage is considered constant for ease of analysis. Therefore, the conversion system must have a wide voltage gain range to use the full power range from the input source.

As the power output of the input source is almost linearly related to the voltage, the input source voltage can reach values close to zero at operating points with low power output and high currents. To limit the input voltage range and, therefore, the required gain of the conversion system, a minimum operating voltage is set for the conversion system. This minimum operation voltage is half the maximum power point voltage V_{mp} . Furthermore, the maximum voltage of the input source is also specified as the maximum voltage of the conversion system.

The requirements for the conversion system are presented in Table 3.7. The input and output voltage range determines the conversion system's minimum and maximum voltage gains. In addition, the maximum power gain is determined using the maximum power voltage $V_{in,mp}$.

Besides the specifications in Table 3.7, the required apparent power of the conversion system is considered when comparing different topologies. The apparent power is directly related to the size of reactive components in the conversion system. A lower apparent power results in smaller reactive components, reducing the overall system size. Thus, the apparent power of different topologies is compared before the most suitable conversion system topology is chosen.

The remaining parts of this section are divided into two subsections. First, the half- and full-bridge inverter topologies are introduced and analyzed. Second, the SABL and LLC converter types are compared using waveform analysis and the design of an example inverter. The inverter and converter topologies for the CET system are chosen to conclude the section.

Table 3.7: The specifications of the converter that sits between the solar panels and the satellite battery.

Parameter	Value
$V_{in,min}$	163 V
$V_{in,mp}$	328 V
$V_{in,max}$	343 V
$P_{in,max}$	3010 W
V_{out}	300 V
Minimum gain (A_{min})	0.875
Maximum power gain (A_{mp})	0.915
Maximum gain (A_{max})	1.840

3.3.1. Primary Side Inverter

The AC-link must be supplied by an AC signal to transfer energy. However, the input source outputs a DC power. Therefore, an inverter is needed to convert the DC to AC power such that the AC-link can function.

In this subsection, the half- and full-bridge topologies are considered. Both the topologies are presented based on the information from [38]. First, the half-bridge topology, waveforms and basic operating principle are discussed in the second part, and the same information is provided for the full-bridge. Third, the possible control methods of both half- and full-bridge are presented, and differences are highlighted. Lastly, the two topologies are compared.

Half and Full-Bridge Topologies

The half-bridge topology is shown in Figure 3.5a. It consists of switching leg with two switches T_{A+} and T_{A-} along with the associated switch diodes D_{A+} and D_{A-} respectively. Via the two identical capacitors connected between the DC input voltage V_d , a new reference point is created at half the input voltage and used at the output.

With two switches in the topology, four switching states are possible. Nevertheless, there are only two allowed switching states. First, the input can not be shorted; thus, both switches can not be closed simultaneously. Second, the load connected to the half-bridge influences the switching states. As the AC-link is a transformer, the load connected to the half-bridge is inductive. If a current flows in the inductive load, there must be a path for the current on the half-bridge. Consequently, one of the switches must be closed to ensure the current path. The output voltage of the half-bridge is thus equal to half the input voltage, which is either positive or negative.

Next, the full-bridge topology is introduced and presented in Figure 3.5b. The figure shows that the full-bridge uses two switching legs, A and B , instead of the single switching leg used by the half-bridge. Adding the second switching leg allows the voltage at the negative output terminal to be controlled, creating more possible output voltage combinations.

The possible switching states for the full-bridge compared to the half-bridge are increased from four to sixteen. Still, as with the half-bridge, not all switching states are allowed. By applying the same constraints regarding the shorting of the input and the inductive load, the allowed switching states are reduced to four as shown in Table 3.8. The table shows that a zero output voltage is possible while providing a current path. Furthermore, the magnitude of the output voltage is doubled and equals the input voltage.

With the knowledge of the allowed switching states, the focus is shifted to controlling the output voltage. In the next section, the control methods for both the half- and full-bridge are introduced.

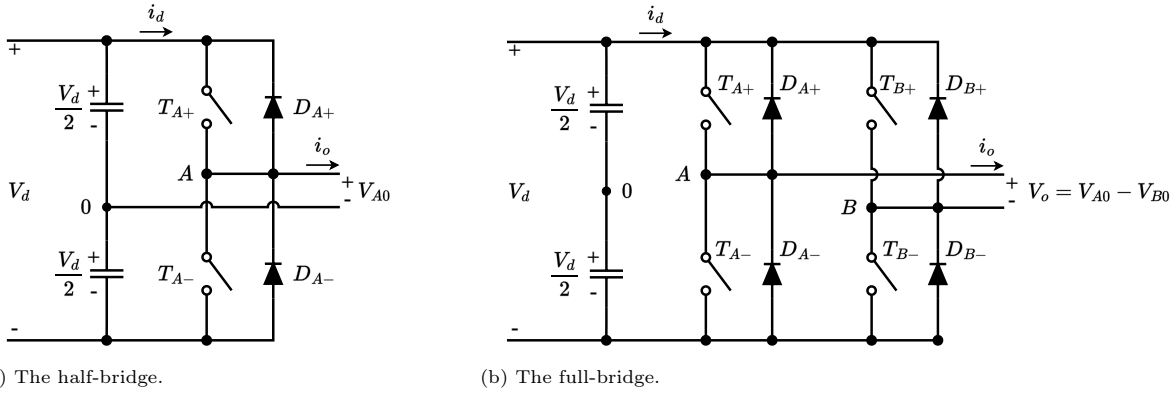


Figure 3.5: The considered inverter topologies in this research.

Bridge Control Methods

Two methods for controlling the bridge topologies are introduced. First, the square-wave mode is explained before continuing with the phase-shift angle control.

The square-wave control uses a duty cycle of $D = 0.5$ for the switches in the bridge. For the half-bridge, switches $T = A+$ and T_{A-} are opened and closed opposite of each other. As a result, the output voltage is a square wave that is switched between $-\frac{V_d}{2}$ and $\frac{V_d}{2}$.

Table 3.8: The allowed switching states for the full-bridge and the output voltage where 0 and 1, respectively, represent an open and closed switch.

State	T_{A+}	T_{A-}	T_{B+}	T_{B-}	V_o
1	1	0	0	1	V_d
2	0	1	1	0	$-V_d$
3	1	0	1	0	0
4	0	1	0	1	0

The output signal can be decomposed into a fundamental frequency and harmonics with the Fourier analysis. From the decomposition of the square-wave output, the peak amplitude of the fundamental component, denoted by subscript 1, is shown by Equation (3.11) [38].

$$\hat{V}_{o1} = \frac{2V_d}{\pi} \quad (3.11)$$

Similarly, the full-bridge switches have the same duty cycle as the switches in the half-bridge. However, in the full-bridge, there are switching pairs. The first pair consists of T_{A+} and T_{B-} and the second of T_{A-} and T_{B+} . Consequently, the output voltage is switched between $-V_d$ and V_d and the peak amplitude of the fundamental component is given by Equation (3.12).

$$\hat{V}_{o1} = \frac{4V_d}{\pi} \quad (3.12)$$

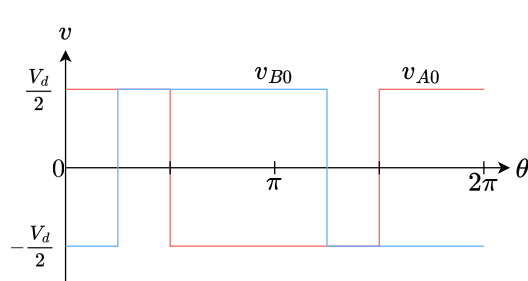
It should be noted that for both the half- and full-bridge, the output voltage amplitude is constant and can not be controlled. Only the switching frequency can be manipulated to control the output voltage frequency. This fact should be considered when choosing the converter topology.

The second and last control method introduced is the voltage cancellation or phase-shift angle control. This control method only applies to the full-bridge inverter as it uses the overlap of the two switching leg outputs. In Figure 3.6, the output voltage waveforms of both switching legs are shown along with inverter output.

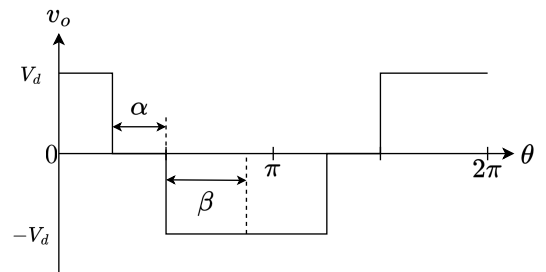
Both the switching legs operate in square-wave mode and thus have duty cycles of $D = 0.5$. The control of the output is achieved by shifting the phase angle of switching leg B while keeping the phase shift of A at zero. As seen in Figure 3.6, the inverter output is zero when the two switching legs outputs overlap. This overlap angle is defined as α . For ease of analysis, the overlap angle is redefined to β as seen in Equation (3.13). Finally, the fundamental frequency component of the inverter output is given by Equation (3.14)

$$\beta = \frac{\pi - \alpha}{2} \quad (3.13)$$

$$\hat{V}_{o1} = \frac{4}{\pi} V_d \sin(\beta) \quad (3.14)$$



(a) The switching leg A and B voltage output waveforms v_{A0} and v_{B0} respectively.



(b) The full-bridge inverter output v_o where α is the overlap angle and $\beta = \frac{\pi - \alpha}{2}$.

Figure 3.6: The output waveforms of the full-bridge inverter with phase-shift angle control.

In the case of phase-shift angle control, the inverter can directly control the amplitude and frequency of the output. This allows for more freedom regarding the choice of the rectification and the AC-link compared to the square-wave control. The following subsection compares the half- and full-bridge based on the output characteristics.

Inverter Topology Comparison

To conclude this inverter section, the half- and full-bridge are compared based on the output voltage and the control methods. In addition, the conduction and switching losses are considered.

The half- and full-bridge characteristics are summarised in Table 3.9. The first difference between the topologies is the maximum output voltage. The half-bridge only outputs half of the full-bridge output voltage. As a result, the half-bridge output current is doubled compared to the full-bridge when the same output power is required. Since a transformer is connected to the output of the inverter, the winding losses are influenced by the inverter output current. As a result, a lower output current decreases the winding losses.

A second noticeable difference is the increase in switches for the full-bridge. At first sight, the doubling of the switches also seems to double the switch losses. However, if the general equations for the conduction and switching losses for MOSFETs, respectively shown in Equations (3.15) and (3.16), are reviewed, a dependency on the switch current I_{sw} is found. As mentioned before, the output current of the half-bridge is double that of the full-bridge.

The switching losses are linearly dependent on I_{sw} . Considering the doubling of the switches for the full-bridge and the doubling of the current for the half-bridge, the switching losses for both topologies can be regarded as the same. However, the same can not be said for the conduction losses, as they depend on the square of the switch current. Therefore, the half-bridge conduction losses are considered higher than the full-bridge.

$$P_{con} = I_{sw,rms}^2 R_{DS,on} \quad (3.15)$$

$$P_{sw} = V_d I_{sw} f_{sw} (t_r + t_f) \quad (3.16)$$

The third and last difference is the possible control methods. The square-wave control method applies to both inverter topologies. Furthermore, the phase shift angle control methods can be applied to the full-bridge. Therefore, the full-bridge inverter provides more flexibility for controlling the inverter output than the half-bridge.

To conclude, the full-bridge offers a larger maximum output voltage, lower output current, lower switch losses, and more control possibilities than the half-bridge. No inverter topology has been selected yet, as the converter topology needs to be considered. Therefore, the inverter choice is indicated when the converter is chosen. In the following section, the rectification on the secondary side is discussed.

Table 3.9: The characteristics and possible control methods for the half- and full-bridge inverters.

	Half	Full
Characteristics		
Maximum output voltage	$\frac{2V_d}{\pi}$	$\frac{4V_d}{\pi}$
Number of switches	2	4
Maximum switch voltage	V_d	V_d
Maximum switch current	\hat{i}_o	\hat{i}_o
Control method		
Square wave	Yes	Yes
Phase shift angle	No	Yes

3.3.2. Single vs Dual Active Bridge

This section describes the considerations for the rectification on the secondary side of the CET system. The satellite battery is the load connected to the satellite CET system. This battery operates on a DC

voltage and, therefore, the AC power from the AC-link needs to be rectified to DC before the battery can be charged.

Besides the secondary side, the inverter and the transformer used in the IPT method are also considered in this section. As both the half- and full-bridge are active bridges, there is always an active bridge in the CET system. Next, the two rectification methods are introduced.

First, the simplest rectification topology of four diodes is presented in Figure 3.7a. This diode rectifier is a passive device without any control signals required and, therefore, called a SAB topology. As a result, the current can only flow into the output, and thus, the power flow is unidirectional. The power losses of the diode rectifier are primarily the diode conduction losses. Furthermore, the output voltage of the rectifier can not exceed the input voltage as the diode rectifier is a passive device. Nevertheless, the output voltage can be increased when using the turns ratio of the transformer. In addition, full soft-switching can be achieved for the bridge in case of Continuous Conduction Mode (CCM) operation [39].

Second, the active switch rectifier is shown in Figure 3.7b. In contrast, this topology is called a DAB. This topology is similar to the full-bridge inverter; only the in- and output are switched. A benefit of the switch rectifier is the ability to produce a larger output voltage than the output voltage. In addition, the current can be conducted in both directions resulting in the possibility of bidirectional power flow.

Nevertheless, the bidirectional power flow comes at a cost. On top of the conduction losses, switching losses are introduced. However, these switching losses can be significantly reduced if Zero Voltage Switching (ZVS) can be applied to the switches. [39] shows that soft-switching for input and output bridges is achieved when the DAB operates in boost mode. When in buck mode operation, soft-switching is achievable if the output current is larger than a lower limit.

To control the DAB, both in- and output bridges operate in square-wave mode, and the phase-shift angle control is applied. Nevertheless, the phase shift angle α is defined as the phase shift between the input and output bridges instead of the switching legs within a bridge. Therefore, a single control parameter can control the overall voltage gain of the DAB.

Comparing the SAB and the DAB shows that both topologies require a single control signal to change the voltage gain of the CET system. In addition, both topologies are capable of soft-switching the bridges during operation. However, there are some difference between the two topologies.

First, even though the switching losses are reduced via soft-switching in the DAB, extra losses are still introduced compared to the SAB. Second, the DAB can operate in buck-boost mode while SAB only operates in buck mode. Third, the DAB can bidirectional power flow while the SAB only allows for unidirectional power flow. Lastly, the control and topology complexity of the DAB is increased compared to the SAB because of the added active components. Furthermore, a control signal must be transferred from the primary to the secondary side to coordinate the phase-shift angle α in the case of the DAB topology.

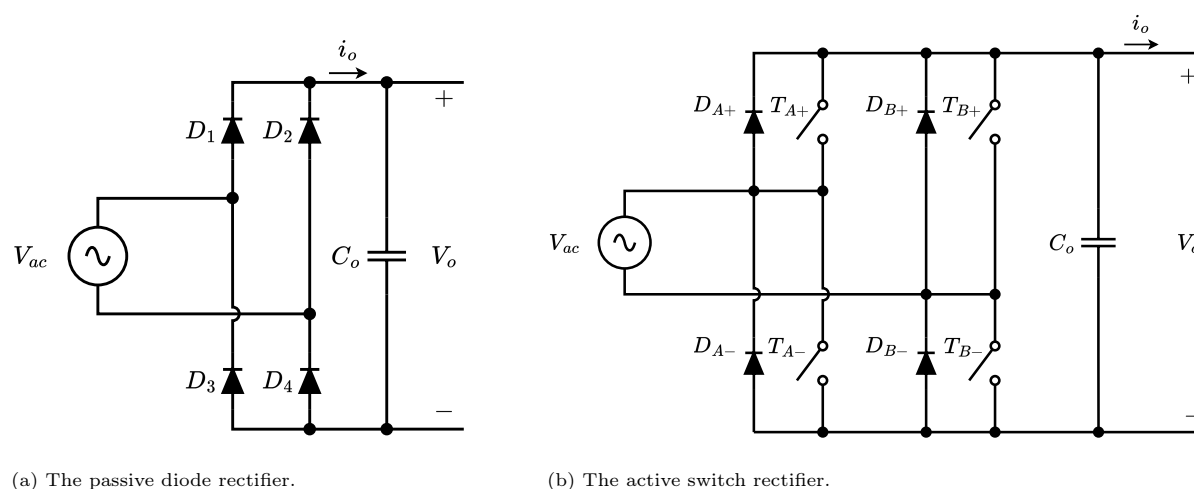


Figure 3.7: The rectification topologies considered in this research.

To conclude, considering the lower losses, reduced complexity and sufficient unidirectional power flow, the SAB is chosen as the preferred topology for rectification on the secondary side. Therefore, a diode rectifier is used for the rectification. The required voltage gain larger than unity from the conversion requirements can be achieved by the turns ratio of the transformer to ensure that a buck operation is required over the whole operating range. In the following section, the SAB topology is further refined by introducing the SABL and LLC converter topologies.

3.3.3. Comparative Study of SABL and LLC topologies

This section finalizes the choice for the converter topology. Two SAB converter topologies are considered: the SABL and the LLC converter. First, both topologies are introduced before performing a waveform and voltage gain analysis. Afterwards, two example converters are built to the same specifications so that the performance can be compared. The most promising of the two converter topologies is chosen to conclude the section.

Single Active Bridge with Output Inductor

In Figure 3.8, the SABL converter topology is presented where the full-bridge inverter, transformer and rectifier are present at, respectively, the left side, middle and right side of the figure. a is the ratio between the transformer's primary and secondary number of turns. To simplify the analysis of the SABL, a is set to unity. This effectively connects the series inductance L directly to the rectifier. It should be noted that the SABL topology can also be driven from a half-bridge inverter.

The phase-shift angle control is used for the SABL converter. The main reason for choosing this control method is the single control input allowing control over both the amplitude and the Total Harmonic Distortion (THD). Having a single control input also simplifies the waveform analysis, as shown further in the section.

Some assumptions are made before analyzing the SABL, and the basic working is explained. First, the in- and output voltage are constant with values V_d and V_o , respectively. Second, the components in the circuit, shown in Figure 3.8, are assumed to be ideal. Consequently, the switches open and close instantaneously, resulting in immediate voltage changes. In addition, the ideal transformer with turns ratio a has an infinite magnetizing inductance, and the leakage inductance is represented by L .

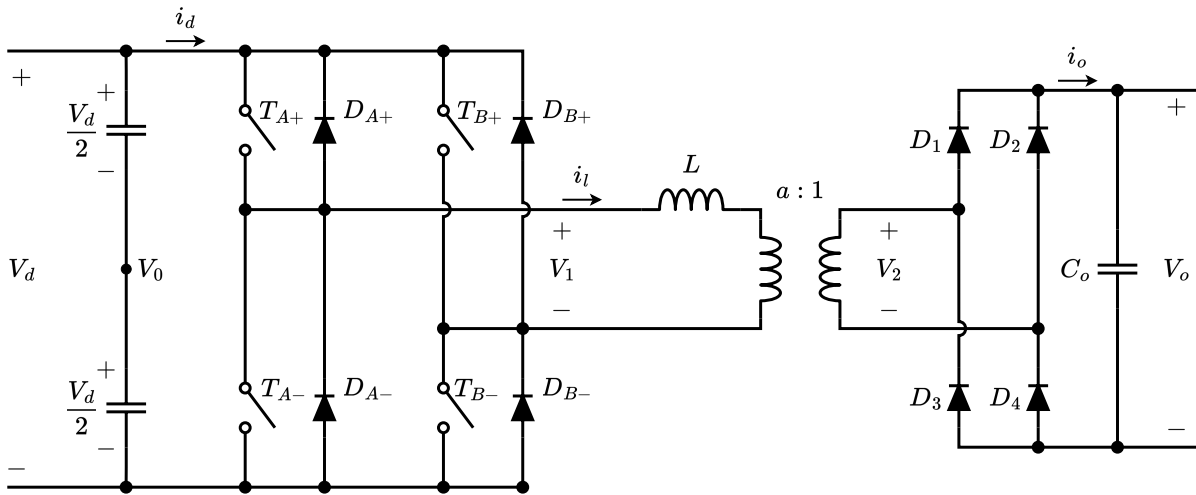


Figure 3.8: A schematic overview of the SABL converter topology where a is the ratio between the primary and secondary number of turns.

With these assumptions and the phase-shift angle control in mind, the basic working of the SABL converter is explained. First, since the output is connected to the secondary side of the transformer via a rectifier, the voltage at V_2 will either be $-V_o$ or V_o depending on the direction of the current i_o . In contrast, due to the use of phase-shift angle control at the primary side, V_1 can take on three values, namely $-V_d$, V_d and zero.

In the ideal SABL converter, the current is completely determined by the inductance value L and the voltages at V_1 and V_2 . Three operating modes are possible based on the current in the inductor L . If the current flow in the inductor is continuous, the converter operates in CCM. On the contrary, if the current returns to zero before half a switching cycle, the converter operates in Discontinuous Conduction Mode (DCM). The last operation mode is achieved when the inductor current is zero at half the switching cycle and is called Boundary Conduction Mode (BCM).

The most current is delivered to the output in the CCM. Combining this with the constant voltage at the output results in the most power delivered in CCM. Therefore, this mode is the most interesting and will be further analyzed. To achieve the CCM operation mode in the SABL converter, Equation (3.17) needs to be satisfied [40].

$$\frac{V_o}{V_i} < \frac{\beta}{\pi} \quad (3.17)$$

[40] published a comprehensive analysis of the SABL converter and the corresponding waveforms. In Figure 3.9a, the voltage and current waveforms for the SABL converter in CCM are shown. From the waveforms in Figure 3.9a, the average output current and the Root Mean Square (RMS) input current can be derived based on β . In addition, the RMS voltage at the input of the transformer $V_{1,rms}$ is determined via the waveform in Figure 3.9a. The apparent and real power can be determined with the currents and the known output voltage V_o .

The analysis of the waveforms is performed in [40] and starts by defining base values. These base values are used to create per-unit quantities that significantly reduce the complexity of the equations. The definitions of the base values are shown in Equation (3.18), and the derived quantities for the current and power are demonstrated in Equation (3.19).

$$V_b = V_d \quad Z_b = \omega_s L \quad \theta_b = \pi \quad (3.18)$$

$$P_b \equiv \frac{V_b^2}{Z_b} = \frac{V_d^2}{\omega_s L}; \quad I_b \equiv \frac{V_b}{Z_b} = \frac{V_d}{\omega_s L} \quad (3.19)$$

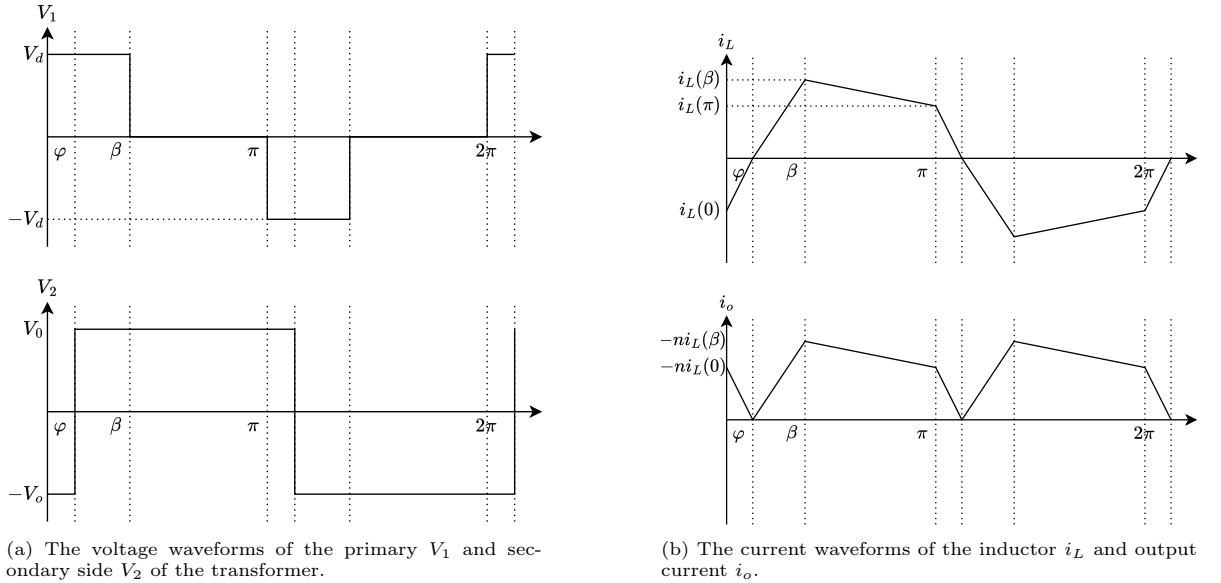


Figure 3.9: The waveforms from the SABL converter in CCM with a turns ratio of $a = 1$. The waveforms are presented in [40].

First, the average output current is determined from the bottom figure of Figure 3.9a. The figure shows that the output current is divided into three intervals between $\theta = [0 : \pi]$. Calculating the average output current during half a switching cycle is readily achieved by determining the areas of the three intervals. The resulting average output current $I_{o,avg,pu}$ is shown in Equation (3.20) and also provided

by [40]. The per unit quantities in Equation (3.20) and the following equations are derived by dividing the relevant quantity by the associated based value.

$$I_{o,avg,pu} = \frac{\pi}{4} (2\beta_{pu} - V_{o,pu}^2 - \beta_{pu}^2) \quad (3.20)$$

Next, the RMS for the inductor current is calculated. As the output current also flows through the inductor, the waveform of i_o in Figure 3.9a is used for the RMS calculation. Again, the output current is split into three intervals between $\theta = [0 : \pi]$. In literature, the RMS values for saw-tooth and trapezoidal are well known. Using the known RMS equations and adding the results accordingly, Equation (3.21) is obtained for the RMS inductor current. It should be noted that the per unit subscripts are omitted in Equation (3.21) to improve readability. The inductor currents at $\theta = 0$ and $\theta = \beta$ and the angle φ are shown in Equation (3.22), Equation (3.23) and Equation (3.24) respectively. Further details of the derivation of the equations below are provided in [40].

$$I_{L,rms,pu} = \sqrt{\frac{1}{3} (i_L(\beta)^2 (1 - \varphi) + i_L(0)^2 (1 - \beta + \varphi) + i_L(0)i_L(\beta) (\beta - 1))} \quad (3.21)$$

$$i_L(0) = \frac{\pi}{2} (V_{o,pu} + 1) (V_{o,pu} - \beta_{pu}) \quad (3.22)$$

$$i_L(\beta) = \frac{\pi}{2} (1 - V_{o,pu}) (V_{o,pu} + \beta_{pu}) \quad (3.23)$$

$$\varphi = \frac{1}{2} (\beta_{pu} - V_{o,pu}) \quad (3.24)$$

Lastly, the final missing value for the apparent power calculation is the primary side transformer RMS voltage. This value is obtained by taking the RMS of the V_1 voltage waveform in Figure 3.9a. This waveform is similar to a pulsed signal, and the RMS of such a signal is known in the literature. The resulting primary side transformer RMS voltage is shown in Equation (3.25).

$$V_{1,rms,pu} = \frac{V_d \sqrt{D_{pu}}}{V_d} = \sqrt{\beta_{pu}} \quad (3.25)$$

LLC Converter

The layout of the LLC converter is somewhat similar to the previously discussed SABL converter. From Figure 3.10, it can be seen that the series inductance and the ideal transformer, with turns ratio a , are still present. Nevertheless, two new components are introduced: a series resonant capacitor C_r and a magnetizing inductance L_m . Together with the series inductance L_r , these three components form a resonant tank. As two inductive and a single capacitive component are involved in the converter, it is called an LLC converter. As with the SABL converter, the LLC converter can be driven from a half-bridge inverter.

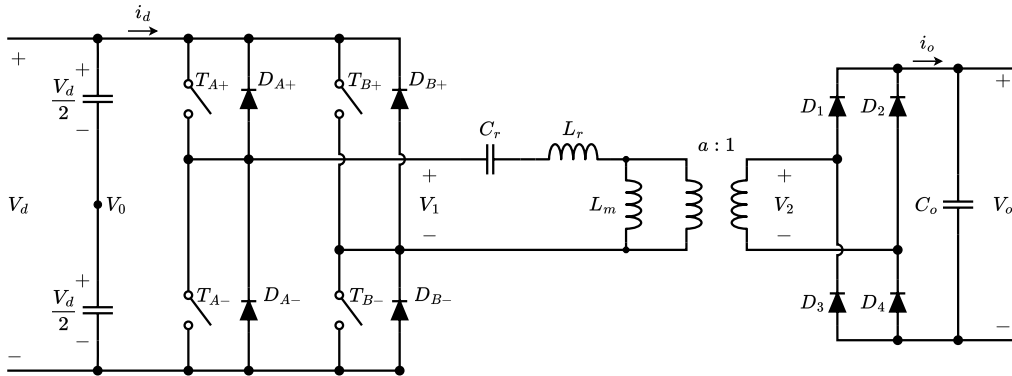


Figure 3.10: A schematic overview of the LLC converter with components C_r , L_r and L_m forming the resonant tank. The transformer with turns ratio a is considered ideal.

As both inductive and capacitive elements are present in the converter, the components resonate with each other, and a resonance frequency is introduced. At the resonance frequency, the combined impedance of the LLC components is minimal. Consequently, the losses are also minimal in the converter operating at a high efficiency [41]. When the input signal frequency is changed, the combined impedance of the LLC components changes as well. As a result, the converter voltage gain changes.

The downside of using the square-wave mode in a full-bridge is the loss of amplitude control at the output. However, as just stated, the LLC converter output voltage gain depends on the frequency. Consequently, from the converter's point of view, the output voltage control is maintained when using square-wave mode for the full-bridge inverter. Therefore, the square-wave mode controls both frequency and output voltage with a single input. Thus, the square-wave mode is a suitable control method for the LLC converter and will be used in this research.

The resonance frequency, originating from the resonance capacitor and the series inductance, allows for three distinct operating modes depending on the switching frequency. Figure 3.11 shows the current waveforms of the two inductors and the rectifier diodes for the three operating modes, and the effects on the converter output are discussed next.

In Figure 3.11a, the converter switching frequency operates at the resonance frequency. At half the switching cycle, the series inductance current equals the magnetizing current, resulting in a zero secondary current. A power delivery cycle is completed, and the current direction is switched at the output.

Next, the LLC converter operation below the resonance frequency is shown in Figure 3.11b. During this operation, the series inductance current equals the magnetizing current before completing the switching cycle. As a result, the secondary current is zero for a significant period, and the rectifier and output are considered disconnected from the resonant tank. The magnetizing inductance only has a small voltage across it, resulting in a stable magnetizing current as seen in Figure 3.11b. The conduction losses on the primary side increase as the average current over a switching cycle increases compared to the operation at the resonance frequency.

Lastly, Figure 3.11c shows the operation above the resonance frequency. In this operation mode, the switching interrupts the power cycle as the series inductor current is greater than the magnetizing inductance at the switching point. As a result of the larger current in the switches during switching, the turn-off losses are increased. Furthermore, from Figure 3.11c, it is observed that the diodes suffer from hard commutation as the diode current is none zero during the switching.

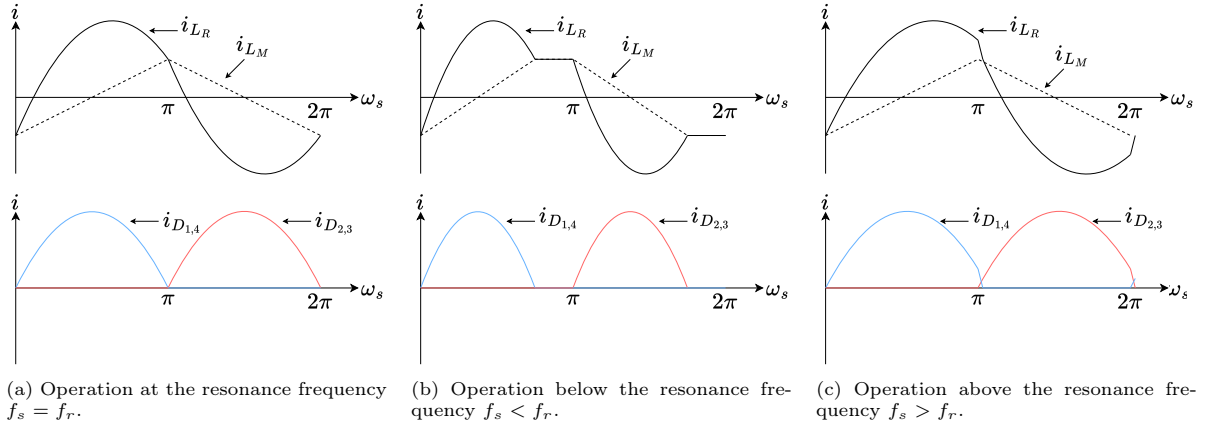


Figure 3.11: The LLC converter current waveforms at different operating frequencies where I_{Lm} , I_{Lr} and I_D are, respectively, the magnetizing and series inductances and diode currents.

Unfortunately, due to the introduced resonance, the LLC converter's waveforms are more complex than the SABL converter. Therefore, a different approach is taken to analyze the LLC converter voltage gain. The basis for the LLC converter analysis relies on the equivalent circuit shown in Figure 3.12a. In the figure, the rectifier and load are replaced with an equivalent AC load $R_{L,eq}$.

The voltage gain of the equivalent circuit A_v is presented in [41] and shown in Equation (3.26). The voltage gain depends on the switching and resonance frequency ratio F_x , shown in Equation (3.27), the quality factor Q and the ratio between the series and magnetizing inductance m . The quality factor

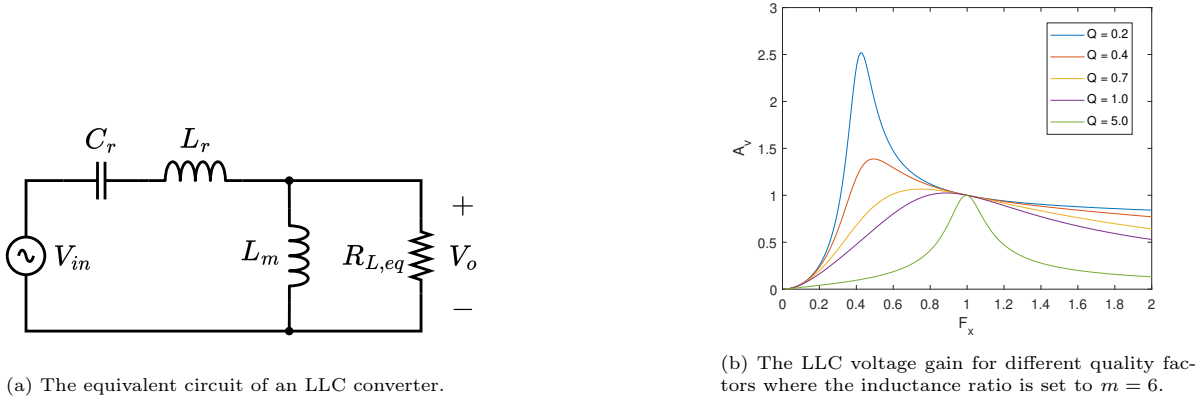
mainly depends on the load conditions and differs at different output powers. Figure 3.12b shows the voltage gain response versus the frequency ratio F_x for different quality factors. Next, the voltage gain for the three operating regions is briefly discussed.

$$A_v = \frac{F_x^2(m-1)}{\sqrt{(F_x^2 m - 1)^2 + F_x^2 Q^2 (F_x^2 - 1)^2 (m-1)^2}} \quad (3.26)$$

$$F_x = \frac{f_s}{f_r} \quad (3.27)$$

When the LLC converter operates at the resonance frequency, the voltage gain is unity independent of the quality factor. The region $F_x < 1$ in Figure 3.12b corresponds to the LLC converter operating below the resonance frequency. In this region, the voltage gain is larger than one if the quality factor is below one, achieving a boost-mode operation. In contrast, the voltage gain is smaller than one for the region, $F_x > 1$, corresponding to operating above the resonant frequency. Thus, a buck-mode operation is achieved independent of the quality factor.

Until now, the topology and basic waveforms of the SABL and LLC converter are introduced. The following subsections compare the two converters based on designed example converters for both types.



(a) The equivalent circuit of an LLC converter.

(b) The LLC voltage gain for different quality factors where the inductance ratio is set to $m = 6$.

Figure 3.12

SABL Converter Solution

This section provides the designs of a basic example converter for the SABL converter. The example converters for both converter types are designed with the exact specifications, shown in Table 3.10, and afterwards are compared based on the apparent power required and the operating modes. First, the real and apparent powers for the SABL converter are derived based on the per unit parameters.

Table 3.10: The specifications for the example converter.

Parameter	Value
Input Voltage (V_i)	300 V
Output Voltage (V_o)	210 V
Output power (P_o)	3 kW
Resonance frequency (f_r)	50 kHz

Starting with the power calculations. In Equation (3.28) and Equation (3.29), the real and apparent power calculations are shown respectively. With the real and apparent power defined, the relation to the output voltage and β is analyzed. The voltage and current quantities in Equations (3.28) and (3.29) are already derived in Section 3.3.3.

$$P_{o,pu} = I_{o,avg,pu} V_{pu} \quad (3.28)$$

$$S_{L,pu} = I_{L,rms,pu} V_{1,rms,pu} \quad (3.29)$$

In Figure 3.13, the real and apparent powers are plotted against β for different output voltage values. A first observation from the real power plot is that the maximum output power is achieved by setting the output voltage to $V_{o,pu} \approx 0.6$. Both increasing or decreasing the output voltage reduces the available output power. A second observation is that the maximum power is transferred at $\beta = 1$ for all output voltage settings. This β value results in a square wave operating as there will be no overlap between the switching legs of the full-bridge inverter.

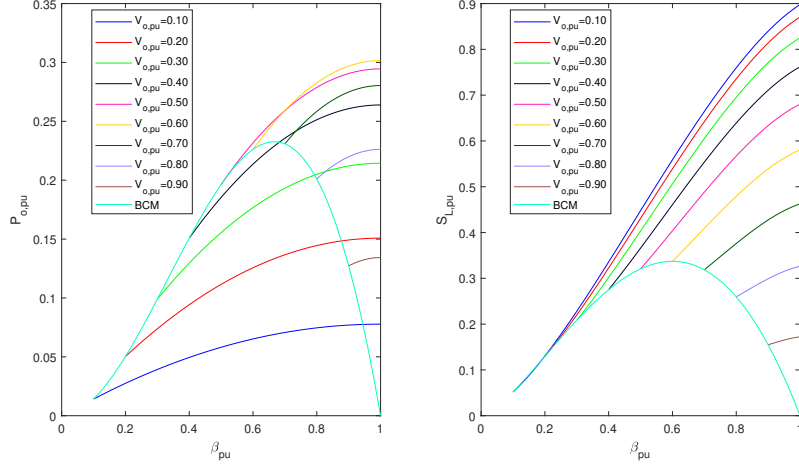


Figure 3.13: The left and right plots show the output real power and transformer apparent power per unit, respectively, for different output voltage values.

In contrast, the apparent power increases as β is increased. Furthermore, by selecting a larger output voltage, the apparent power decreases.

Comparing the effects of both the real and apparent powers shows that a trade-off needs to be made between the two when choosing the output voltage and β . A value of $V_{o,pu} = 0.7$ is chosen to balance the real and apparent power. While this output voltage does not deliver the converter's maximum power, the apparent power reduction is more significant than the real power decrease. Next, from the real power plot in Figure 3.13, it can be seen that the real power barely increases beyond $\beta = 0.9$. In contrast, the apparent is reduced compared to $\beta = 1$. Therefore, the value is set to $\beta = 0.9$.

With both the output voltage and the β chosen, the per unit values for the real and apparent power can be determined. In Table 3.11, are the per unit specifications shown for the SABL converter. These specifications will determine the example converter's real and apparent power. However, first, the LLC converter is introduced in the next section.

Table 3.11: The per unit design parameters for the SABL converter.

Parameter	$V_{o,pu}$	β_{pu}	$P_{o,pu}$	$S_{L,pu}$
Value	0.7	0.9	0.275	0.428

The last remaining step for the example SABL converter is to convert the per-unit specifications to real values. Using the base values of the power and the impedance, the required inductance value is expressed in terms of the power per unit, output power and input voltage, as shown in Equation (3.30). Similarly, once the inductance is calculated, the input apparent power is represented by Equation (3.31).

$$L = \frac{P_{pu} V_d^2}{\omega_s P_o} \quad (3.30)$$

$$S_{in} = S_{L,pu} P_b = \frac{S_{L,pu} V_d^2}{\omega_s L} \quad (3.31)$$

To summarize, the real and apparent powers are analyzed on a per-unit basis, and optimal settings for the per-unit output voltage and β are chosen. The required inductance and input apparent power

values are derived from the per-unit values. The resulting values are discussed later after the example LLC converter is designed in the next section.

LLC Converter Solution

As with the SABL example converter, the LLC converter is designed for the specifications shown in Table 3.10. Compared to the SABL converter, the LLC converter design is more complex and requires an iterative process. This iterative process and the remaining design procedure are explained in Chapter 4. The same design procedure is followed for the example LLC converter, and the resulting specifications are shown in Table 3.12. The converter switching frequency is twice the resonance frequency to obtain the required voltage gain. The resulting example converters are compared in the next section, and the most suitable type is chosen.

Table 3.12: The component and design values of the LLC converter solution.

Parameter	Q_{max}	m	$R_{L,min}[\Omega]$	C_r [nF]	L_r [μ H]	L_m [μ H]	f_s [kHz]
Value	0.6	10	11.91	445.2	22.76	204.8	100kHz

Comparison of SABL and LLC Converters

With both the SABL and LLC example converters designed, the two types are compared. The switching frequency for the LLC converter is set to $f_s = 100$ kHz, and therefore, the SABL converter switching frequency is set to the same value. With the switching frequency, the inductance and input apparent power are calculated using Equations (3.30) and (3.31).

Both converters' component values and performance are shown in Table 3.13. Besides the analytical analysis, an LTspice simulation is performed for both converters to validate the analytical methods. The apparent input power for both converters is slightly higher in LTspice compared to the analytical model due to the simplifications assumed in the analytical models. Still, from the results, it can be seen that the LLC converter has a slightly lower input apparent power at the cost of larger component values. In addition, by remembering the fact that the LLC converter operates at $F_x = 2$ and looking at Figure 3.14, it can be seen that the LLC converter operates at a point with significant reactive power. The reactive power can be significantly reduced if an LLC converter operates with a unity gain, resulting in $F_x = 1$. This results in a lower apparent power for the same output power.

Table 3.13: The performance characteristics of the SABL and LLC converter.

Topology	S_{in} [kVA]	P_o [kW]	V_o [V]	L_s [μ H]	L_m [μ H]	C_r [nF]
SABL	4.66	3	210	13.13	-	-
SABL (LTspice)	4.88	2.95	208	13.13	-	-
LLC resonant tank (FHA)	4.3	3	189	22.76	204.8	445.2
LLC resonant tank (LTspice)	4.78	2.99	172	22.76	204.8	445.2

Another aspect to consider before choosing the topology is the possibility for ZVS to reduce the switching losses. In the case of the SABL topology, there is only a transformer connected to the output of the inverter. This results in an inductive load behaviour where the current lags the voltage. Hence, ZVS is possible for the SABL converter. For the LLC converter, the load behaviour seen from the inductor is less evident due to the introduction of the resonance capacitor.

Nevertheless, the voltage gain, shown in Figure 3.12b, indicates the load behaviour. Before the peak voltage gain, the gain increases with the frequency corresponding to a capacitive load. After the peak voltage, the inverse is valid for the relation between the voltage gain and the frequency, resulting in an inductive behaviour. Therefore, ZVS can be achieved for the LLC converter if it operates at frequencies above the maximum gain frequency.

The operating modes are the last aspect of comparing the two converter topologies. The SABL converter can only operate in buck mode, thus requiring a higher input voltage than the output voltage. For this research, the input source has a variable input voltage depending on the drawn power and the solar panel irradiance, resulting in a large input voltage range. The maximum power point requires a

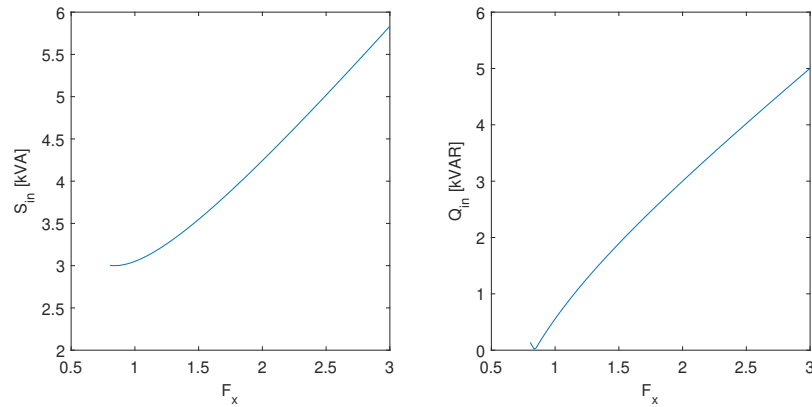


Figure 3.14: The LLC converter apparent and reactive input powers for different frequency ratios.

buck-mode operation with the solar panel's current configuration and the satellite voltage requirement from Table 3.7. However, the operating window of the SABL is limited, and the device can not deliver power at lower setpoints or solar panel irradiance. In contrast, the LLC converter can operate in buck and boost mode. While the apparent power is smallest at unity gain and increases in buck and boost mode, the increased operation window is a definite advantage of the LLC converter over the SABL converter.

3.3.4. Conclusion

To summarize, at the beginning of the section, the half- and full-bridge inverters are introduced along with their characteristics. Both inverter topologies with corresponding output voltage ranges were presented before moving on to the control methods. While both inverters can operate with square-wave mode, the full-bridge inverter also has phase-shift angle control options. As the full-bridge output voltage range is larger and the conduction losses are lower, it is deemed the most suitable inverter. Next, two SAB converters; the SABL and LLC converters were introduced based on topology and waveform analysis. By comparing the two converter types based on a designed converters, the LLC converter offered both buck and boost mode operation, resulting in a large input voltage range, a lower input apparent power and the possibility for ZVS.

In conclusion, the optimal converter topology for the satellite CET system is an LLC converter with a full-bridge as an inverter. The next chapter explains the LLC design procedure in more detail. In addition, an LLC converter is designed based on the specifications for the CET system.

3.4. Transformer choice

In the last section of this chapter, the last part of the CET system, the AC-link, is further defined. This section aims to choose the most suitable transformer geometry for the AC-link. First, different transformer geometries of experimental prototypes found in the literature are compared to achieve this goal. After selecting the most promising transformer geometries, the availability of core shapes and manufacturer lead times are considered when finalizing the transformer geometry.

3.4.1. Transformer Geometries

This section analyses and compares the previously introduced IPT prototypes based on their geometries. Two geometry types are introduced based on the direction the magnetic flux crosses the transformer air gap. When the magnetic flux crosses the air gap in the axial and radial direction, the respective geometries are called axial and radial gap transformers. Next, the axial gap transformer is introduced.

A schematic example of an axial gap transformer is shown in Figure 3.15a. While axial gap transformers are based on the schematic shown Figure 3.15a, the transformer designs can differ significantly, as demonstrated by the four axial gap prototypes introduced next.

First, the transformers in [32] and [30] have similar geometries, and the latter is shown in Figure 3.15b. The ferrite core is circular with a U-shaped cross-section. While the geometries are similar,

the transformer of [30] is almost twice the size of [32].

Second, the design of [29] is even larger compared to [30]. As a result of this increase in size, Zhang *et al.* reported manufacturing limitations and a continuous circular U-shaped core was impossible to produce. The resulting design comprises several U-shaped core pieces connected in a circular bracket.

Lastly, a different approach is taken by [35] to produce a small, coreless transformer. In the design, the transformer coils are routed on Printed Circuit Boards (PCBs), resulting in a compact AC-link. The PCB coil transformer schematic is shown in Figure 3.15c.

The introduced axial prototypes make it clear that the axial gap transformer is pancake-shaped. This shape makes them suitable for applications where the axial length is limited and the radius of the AC-link is plenty. Specific dimensions and performance characteristics are discussed after introducing the radial gap transformers.

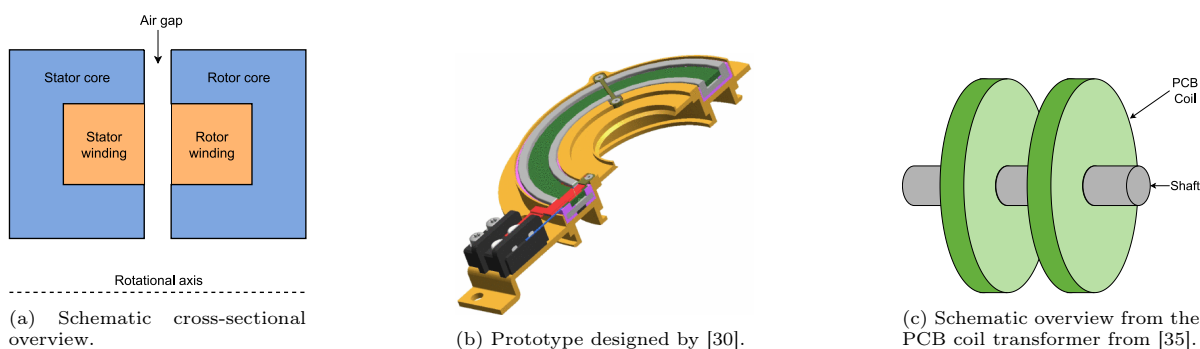


Figure 3.15: Examples of axial gap transformers found in literature.

Next, two prototype radial gap transformers are introduced. Both [33] and [34] have a transformer with the cross-section LL-shaped as shown in Figure 3.16. While both have the same shape, the sizes and power transfer capabilities differ between the two designs. Unfortunately, the papers from the two prototypes report different types of results. Subsequently, comparing the two designs based on performance aspects other than the power transferred proved difficult. At first glance, the radial gap geometry does not offer a compact design in a single direction. Both the axial and radial directions are used to guide the magnetic flux. Next, the axial and radial gap prototypes are compared based on the dimensions and performance specifications.

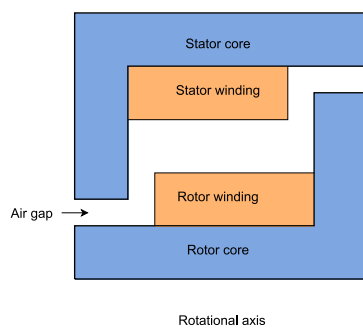


Figure 3.16: A schematic cross-sectional overview of the radial transformer used by [33] and [34].

In Table 3.14, the dimensions, performance specifications and geometry type are shown. By looking at Table 3.14, it is clear that the axial gap transformer from Stancu *et al.* has the largest power transfer capability. It should be noted that the prototype is actively cooled; therefore, the power transfer capability cannot be compared to the other prototypes. Besides [30], the other prototypes have similar power transfer capability, and there is no apparent difference between the radial and axial geometry.

Moving on to the comparison of the power density. Interestingly, the increased power transfer capability from the cooling does not result in the best power density performance for [30] compared to the other prototypes. Due to its minimal size, the highest power density is achieved by the PCB transformer from [35]. However, the power transferred is low compared to others. Therefore, it is

essential to consider other power-dense transformers. After [35], the radial transformers have a higher power density than the axial transformers.

Another aspect to consider before choosing the preferred geometry is the scalability of the power transfer capability. While the design in [35] seems to have high potential, the scalability is uncertain. As no core material is used, enlarging the coils might not increase the power transfer capabilities.

In contrast, the radial transformers from [33] and [34] show that increasing the size also increases the power transfer capability. The same cannot be said for sure about the other axial designs. The uncertainty originates from the fact that the axial prototypes all have different shapes. Furthermore, with the active cooling of [30], a direct comparison to other axial designs is difficult.

When considering the power density, power transfer capability and scalability of the prototypes shown in Table 3.14, the radial gap transformer shows the most promise when active cooling is not considered. Therefore, this research chooses a radial gap transformer for the CET system. The following section refines the transformer geometry based on available core components.

Table 3.14: Dimensions and performance specifications of rotary transformer designs found in the literature. *Estimation as no data was provided. **The AC-link was actively cooled.

Design	Type	Axial length [mm]	Outer diameter [mm]	Power [W]	Power Density [kW/m ³]	Efficiency [-]
Littau [32]	Axial	29	70	1000	2240	97.6%
Stancu [30]	Axial	27*	130	5000	3490**	95%
Zhang [29]	Radial	110	250	1000	46.3	90%
Sun [35]	Radial	7	60	400	3710	-
Krupp [33]	Radial	15	53	400	3020	-
Vip [34]	Radial	30	60	1000	2950	96.30%

3.4.2. Coaxial Solenoid Transformer

With the selection of the radial gap geometry, the ferrite core used by [33], [34], and shown in Figure 3.16, seems an interesting design concept. However, before further analysis was made, the availability of the ferrite core shape was checked.

Unfortunately, a rotary ferrite core with an LL-shaped cross-section is unavailable as an off-the-shelf component. Krupp and Mertens solved the problem by grounding two sized P ferrite cores until the desired LL-shaped cross-section was achieved. On the other hand, [34] does not specify the manufacturer or production method for the ferrite core.

Without the experience of modifying ferrite material combined with the fact that ferrite is a brittle material, modifying existing ferrite core shapes to achieve the desired LL-shaped rotary geometry is not an option. Another option would be to request the desired ferrite core geometry from a manufacturer. However, the lead times of custom ferrite cores are long and often, single editions are either expensive or rejected. Since the lead time of the custom ferrite cores is too long for this research, a different geometry using off-the-shelf ferrite cores is considered.

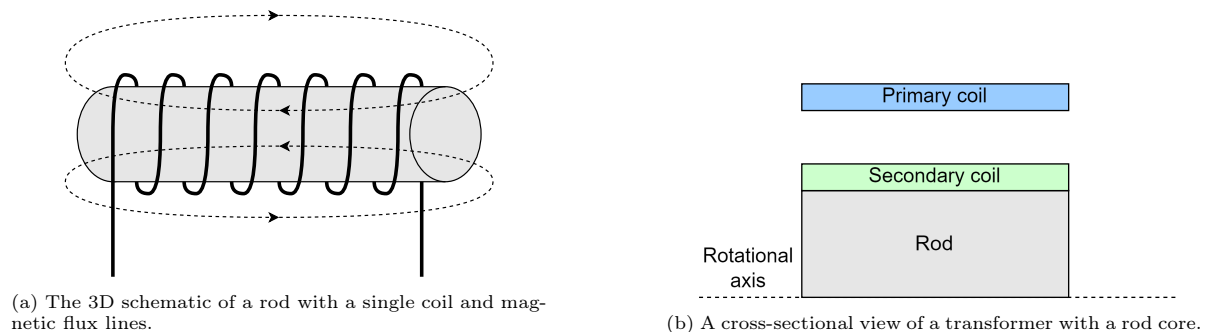


Figure 3.17: The schematic representation of a ferrite rod core with coil(s) wound around it.

A readily available ferrite core from distributors is a ferrite rod. A relatively simple transformer can be constructed using the rod by simplifying winding two coils around it. In Figure 3.17b, it can be seen

that one coil can be directly wound around the ferrite rod. An air gap is left between the coils to allow for the rotation of the outer coil. As the solar panels are rotating in CET system, the outer and inner coils are called the primary and secondary coils.

The geometry depicted in Figure 3.17 resembles the LL-shaped cross-section geometry in Figure 3.16. In both geometries, there is an outer and inner coil, and the flux is concentrated inside the inner coil.

Nevertheless, the magnetic flux paths of the two geometries are vastly different. For the core with an LL-shaped cross-section, the magnetic flux path is well-defined by the ferrite cores and the air gap. Since the ferrite material has a high permeability, the flux is mostly concentrated inside the ferrite core except for some small leakage flux. Therefore, it is considered a closed magnetic circuit, and the reluctance model can be used to determine the inductive parameters analytically.

On the other hand, in Figure 3.17a, it can be seen that the magnetic flux lines connect to the top and bottom of the rod via a long air path. The ferrite rod has a high permeability, resulting in a magnetic flux concentration inside the rod. In contrast, air has a low permeability, resulting in a spread of the magnetic flux in the medium. While the magnetic flux lines start and end respectively at the top and bottom of the ferrite rod, the path through air is not well-defined. As a result, this type of geometry is called an open magnetic circuit. The reluctance model is unsuitable for the analysis as the air path reluctance is not clearly defined. Instead, analysis is performed based on the magnetic field strength and flux density with the aid of Finite Element Method (FEM).

A final note on the ferrite rod geometry considers flexibility in the design process. The available ferrite rods have a wide range of diameters and lengths, resulting in a wide range of possible inductances. Another benefit is the ability to stack multiple rods on top of each other to reach the desired length while maintaining the same diameter. This again increases the inductance range of the ferrite rod transformer.

To summarize, radial gap prototypes in literature outperformed axial gap prototypes in terms of scalability and power density. While the LL-shaped cross-sectional rotary transformer seemed promising, the combination of long manufacturing lead times and the limited duration of this research meant that an off-the-shelf ferrite core was needed. A ferrite rod transformer proved highly modular despite the downside of being an open magnetic circuit. Nevertheless, the chosen transformer geometry for this research is a ferrite rod geometry. The detailed design process of the ferrite rod transformer will be discussed in Chapter 5.

4

LLC Design

Now that the LLC converter is chosen for the satellite CET system, this chapter presents the design procedure in more detail. For clarity, the specifications for the LLC converter are repeated in Table 4.1. It should be noted that the resonance frequency specification is added to the table. The available full-bridge converters in the ESP lab of the TU Delft have operating frequencies in the range of $f_s = \sim 100$ kHz. Therefore, the maximum switching frequency is set to $f_{s,max} = 150$ kHz. By setting the resonance frequency to $f_r = 75$ kHz, the LLC converter can operate below and above the resonance frequency. Consequently, as discussed in the previous chapter, the LLC converter can operate both in boost and buck mode for the voltage.

This chapter starts by introducing the LLC converter design procedure. Here, every step of the design is explained, along with the influence of the design parameters. The designed LLC converter is presented in the following section, and the voltage gain and currents are analyzed. Finally, the LLC converter characteristics are given to conclude the chapter, including the parameters required for the transformer design, which will be discussed in the next chapter.

Table 4.1: The specifications for the LLC converter used in the satellite CET system.

Parameter	Value
$V_{in,min}$	163 V
$V_{in,mp}$	327.7 V
$V_{in,max}$	343 V
$P_{in,max}$	3010 W
V_{out}	300 V
Maximum Power gain ($A_{v,mp}$)	0.915
Maximum gain ($A_{v,max}$)	1.840
f_r	75 kHz
$f_{s,max}$	150 kHz
Efficiency (η)	≥ 98 %

4.1. Design Process

To design the LLC converter according to the specifications in Table 4.1, the design process from [41] is used. The main focus of the design is to ensure the maximum voltage gain is reached at the corresponding load. In addition, the minimum operating frequency is determined such that the LLC resonant tank has an inductive behaviour, allowing for ZVS in the full-bridge.

The design process in [41] is shown in Figure 4.1 and six steps. First, an initial maximum quality factor Q_{max} is set based on the load requirements. Second, an initial value for the inductance ratio m is set based on the voltage gain and efficiency requirement. Third, at maximum load, using Q_{max} , the minimum switching frequency is calculated to ensure ZVS at all load conditions. Fourth, the maximum gain at the corresponding load is calculated and compared to the gain requirement. Fifth,

if the maximum gain differs from the gain requirement, the value of m is adjusted accordingly, and steps three and four are repeated. Sixth and lastly, when the gain requirements are met, the resonant component values are calculated, concluding the LLC design.

The following section elaborates on the six design steps and highlights design choices. First, the initial value for the maximum quality factor is presented.

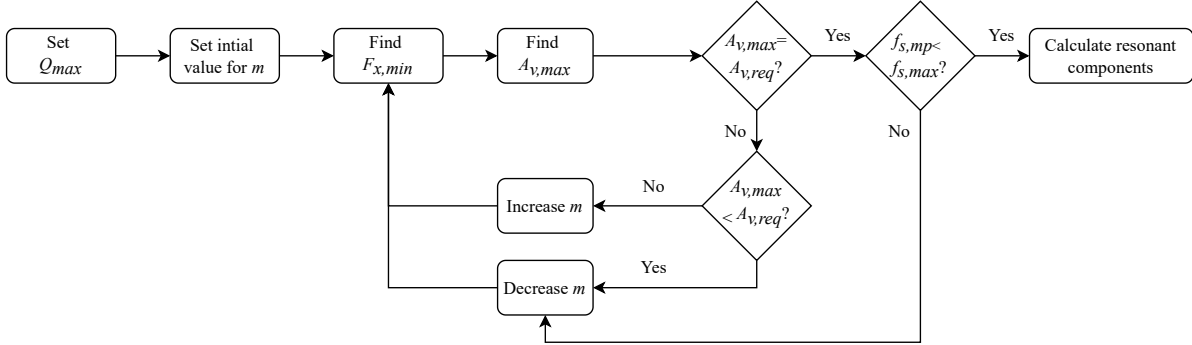


Figure 4.1: The design flow chart for the LLC converter, as presented in [41].

Maximum Quality Factor Setting

For clarity, the LLC converter voltage gain is repeated in Equation (4.1) where F_x is the ratio between the switching and resonance frequency, m the inductance ratio and Q the quality factor. The equation shows that the maximum gain is inversely proportional to the quality factor. Therefore, the maximum gain requirements are evaluated at the corresponding load when choosing the quality factor.

$$A_v = \frac{F_x^2(m-1)}{\sqrt{(F_x^2m-1)^2 + F_x^2Q^2(F_x^2-1)^2(m-1)^2}} \quad (4.1)$$

To further show the influence of the quality factor on the LLC converter gain, Figure 4.2a shows the LLC converter gain for different quality factors. From the figure, it can be seen that the quality factor heavily influences the maximum gain. Furthermore, the peak of voltage gain is located at lower frequencies for smaller Q values. As the peak gain is the crossover point between the capacitive and inductive behaviour of the resonant tank, the minimum allowed frequency to ensure ZVS is lower for smaller Q values. Limiting the minimum switching frequency influences the maximum achievable gain at loads below the maximum conditions.

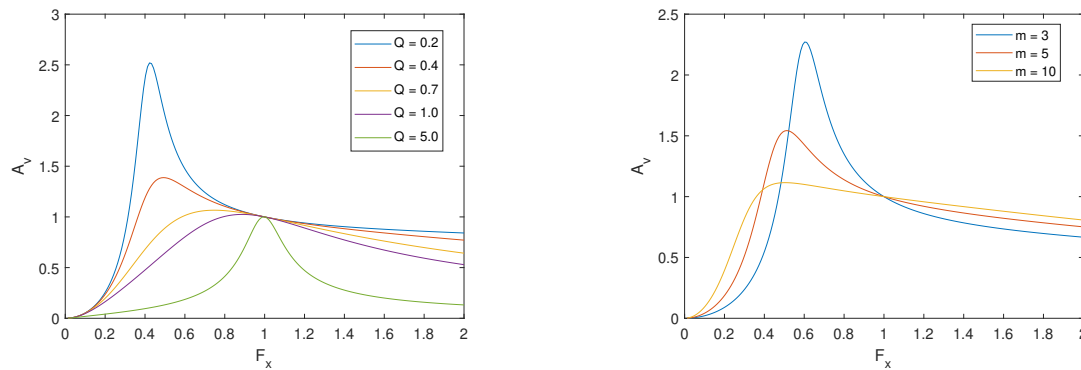
By looking at the region where the switching frequency is larger than the resonance frequency $F_x > 1$, it can be seen that the voltage attenuation is proportional to the quality factor. As a result, higher quality factors provide a more significant attenuation at the same switching frequency than lower quality factors.

To summarize, both the minimum and maximum gain must be considered at their corresponding load conditions and resulting quality factors when selecting the maximum quality factor Q_{max} . By choosing a low Q_{max} , the maximum gain is higher at a lower minimum frequency in boost-mode operation at the cost of attenuation capability in buck-mode operation. In contrast, the opposite is true when selecting a high Q_{max} .

Next, the Q_{max} value is chosen according to the LLC design requirements of the CET system. In this research, the LLC converter is connected to a solar panel, so the maximum gain is required at half the input power. Therefore, the quality factor will be half of Q_{max} and the achieved gain at the minimum switching frequency is increased compared to Q_{max} . In addition, the output voltage must be attenuated at the maximum input power, resulting in Q_{max} . Thus, these two specifications result in a trade-off for selecting Q_{max} . To allow for both the maximum gain in boost mode and the attenuation at maximum power, the maximum quality factor is set to a conservative value of $Q_{max} = 0.6$.

Initial m selection

Next up is the influence of the inductance ratio m . In Equation (4.2), the definition of the inductance ratio is shown where L_r and L_m are the resonant and magnetizing inductance, respectively. The



(a) The gain for different quality factor values Q where the inductance ratio is set to $m = 6$.

(b) The gain for different inductance ratio factors m where the quality factor is set to $Q = 0.4$.

Figure 4.2: The LLC converter voltage gain A_v as a function of the ratio between the switching and resonance frequency F_x .

equation shows that an increase of m increases the magnetizing inductance relative to the resonant inductance. Increasing the magnetizing inductance means less current flows through the magnetizing inductance during a switching cycle. As a result, the flux density in the transformer core is lower, and the core losses are decreased. In addition, less circulating current reduces copper losses as well. From an efficiency point of view, m should be set as high as possible.

$$m = \frac{L_r + L_m}{L_r} \quad (4.2)$$

Nevertheless, m should not be chosen purely based on efficiency as m also influences the LLC converter gain. From Equation (4.1), it is not immediately clear what the effect of m is on the voltage gain due to the multiple appearances of the term. However, Figure 4.2b provides the voltage gain for various values of m while keeping the quality factor constant. From the figure, two observations are made.

First, as m increases, the voltage gain curve flattens in both the buck and boost mode operation regions. As a result, the maximum gain and attenuation decrease. This behaviour differs from that under the quality factor influence, where a large value of Q would decrease the maximum gain but increase the attenuation.

The second observation is that as m increases, the peak of the voltage gain curve shifts to lower frequencies. This shift allows for a lower minimum switching frequency while ensuring the possibility for ZVS.

Combining the two observations and the previous notion regarding efficiency, it becomes clear that the selection of m is a trade-off between efficiency and the control of the voltage gain. It should be noted that the value of m is adjusted during the design process to meet the gain requirements. As this research aims to design an efficient CET system, a high starting value for the inductance ratio is chosen and is set to $m = 10$. While the starting value of m is expected to be too high to meet the required gains, m will be decreased further in the design process until the gain requirements are met.

Minimum Switching Frequency

With the selected quality factor and inductance ratio, the voltage gain curve can be expressed by the frequency ratio F_x . As mentioned before, the voltage gain peak is the crossover point between the capacitive and inductive behaviour of the resonant tank. Therefore, the voltage gain peak determines the minimum allowed switching frequency. Furthermore, the voltage gain peak is not equal for all values of Q . From Figure 4.2a, it can be seen that the frequency ratio at which the voltage gain peak occurs increases with Q . Thus, to ensure that the LLC converter is capable of ZVS at all operating points, the minimum switching frequency is determined during maximum load conditions $Q = Q_{max}$.

Next, the derivative of equation Equation (4.1) needs to be taken to determine the voltage gain peak. Unfortunately, the voltage gain equation is nonlinear and can not be solved easily analytically. To circumvent this problem, the symbolic toolbox from MATLAB is used to derive the derivative and

solve the Equation (4.3) for F_x . Using the result from MATLAB, the minimum switching frequency is determined with Equation (4.4).

$$\left. \frac{\delta A_v(Q, m, F_x)}{\delta F_x} \right|_{Q=Q_{max}, m=m} = 0 \quad (4.3)$$

$$F_x = \frac{f_s}{f_r} \quad (4.4)$$

Maximum Gain Validation

The minimum and maximum gain requirements are validated before proceeding to the design process's final step. First, the maximum gain requirement is discussed.

The maximum gain is required at the lowest input voltage of the LLC converter. As the input to the LLC converter is solar panels, the power is decreased at lower voltages, resulting in a lower load and a lower Q value. When validating the maximum gain, Equation (4.5) is used to account for the changed quality factor. The maximum achievable gain at the minimum switching frequency is then given by Equation (4.6).

$$Q_{v,min} = \frac{V_{min}}{V_{mp}} Q_{max} \quad (4.5)$$

$$A_{v,max} = A_v(Q_{v,min}, m, F_{x,min}) \quad (4.6)$$

Next, the maximum power gain requirement is validated by checking the required switching frequency for the maximum power gain occurs $f_{s,mp}$. By setting Equation (4.1) equal to the maximum gain requirement and using $Q = Q_{max}$ and the obtained value for m , F_x can be solved for with the use of the MATLAB symbolic toolbox. If no solution is found or the solution is in the region $F_x > 2$, the LLC design does not meet the minimum gain or the maximum switching frequency specification.

If the gain or frequency requirements are not met, m is adjusted, and the minimum switching frequency and gain verification steps are repeated. When the maximum gain is too low, the value of m is decreased. In contrast, when the maximum gain exceeds the requirement, m can be increased. Should the required switching frequency for the maximum power gain exceed the maximum switching frequency requirement, then m needs to be decreased. When both requirements are met, the design process moves to the last step, where the resonant components are calculated.

Calculate resonance components

The last remaining step before the LLC design is completed is the calculation of the resonant components with the obtained parameters. For clarity, the equations for the quality factor, the inductance ratio and the resonant frequency are repeated in Equations (4.7) to (4.9).

$$Q = \frac{\sqrt{\frac{L_r}{C_r}}}{R_{ac}} \quad (4.7)$$

$$m = \frac{L_r + L_m}{L_r} \quad (4.8)$$

$$f_r = \frac{1}{2\pi\sqrt{L_r C_r}} \quad (4.9)$$

There are three LLC components: the resonant capacitor C_r , resonant inductor L_r and the magnetizing inductance L_m . As there are three equations and three unknowns, the component values can be expressed using Equations (4.7) to (4.9). The resulting component definitions are shown in Equations (4.10) to (4.12) where the equivalent AC output resistance is given by Equation (4.13). The maximum quality factor is achieved at the maximum input power. Consequently, the equivalent AC output resistance will attain its minimum value. Hence the component values are calculated using the minimum equivalent AC output resistance $R_{ac,min}$.

$$C_r = \frac{1}{2\pi Q_{max} R_{ac,min} f_r} \quad (4.10)$$

$$L_r = (Q_{max}R_{ac,min})^2 C_r \quad (4.11)$$

$$L_m = L_r (m - 1) \quad (4.12)$$

$$R_{ac} = \frac{8}{\pi^2} R_o = \frac{8}{\pi^2} \frac{V_o^2}{P_o} \quad (4.13)$$

4.2. Analysis of the Resulting LLC Design

In the previous section, the design procedure for the LLC converter is fully described, along with the initial settings for the maximum quality factor Q_{max} and the inductance ratio m . The input specifications and values used in the design procedure are shown in Table 4.2. After performing the design procedure, the LLC design is finished, and the resulting parameters are shown in Table 4.3.

Next, the behaviour of the designed LLC converter is further analyzed. First, the voltage gain is analyzed using the analytical transfer function and LTspice AC small circuit analysis and steady-state waveform simulations. The analysis is performed to validate that the designed LLC converter reaches the required voltage gain. Furthermore, the currents in the resonant tank are inspected using LTspice waveforms along with the analytical transfer function. The resulting currents are used as inputs for the transformer design from the analysis, discussed in Chapter 5.

Table 4.2: The input specifications for the LLC design process where A_v represents the voltage gain and f_s is the switching frequency.

Parameter	Value
$V_{in,min}$	163 V
$V_{in,mp}$	327.7 V
$P_{in,max}$	3010 W
V_{out}	300 V
$A_{v,mp}$	0.915
$A_{v,max}$	1.840
$f_{s,max}$	150 kHz
f_r	75 kHz
Start m	10
Q_{max}	0.6

Table 4.3: The output parameters of the LLC design where f_s represents the switching frequency.

Parameter	Value
m	3.875
$f_{s,min}$	46.56 kHz
$f_{s,mp}$	85.59 kHz
$f_{s,max}$	92.35 kHz
C_r	146 nF
L_r	30.86 μ H
L_m	88.72 μ H

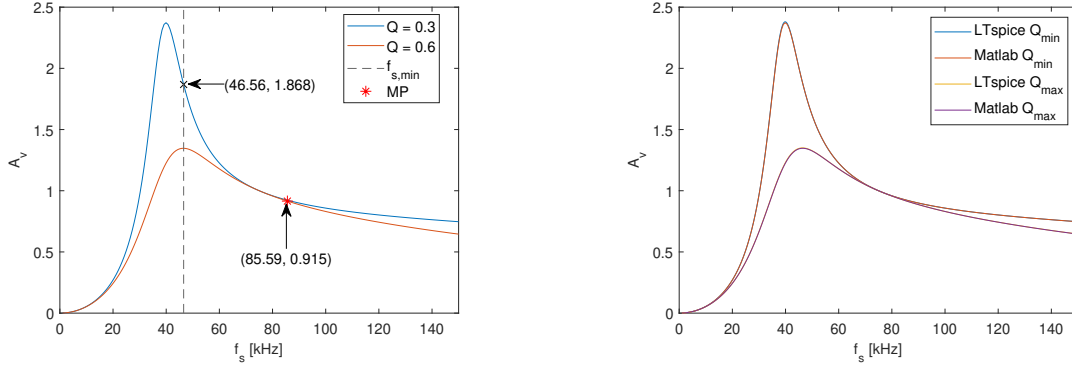
4.2.1. Voltage Gain

In Figure 4.3a, the LLC converter voltage gain curve is shown for both the minimum and maximum quality factor corresponding to the minimum and maximum loads. In addition, the minimum switching frequency is indicated with the dashed line. In the figure, the two points are highlighted, namely, the maximum voltage gain and maximum power (MP). The maximum voltage gain from the LLC design is slightly higher than the required maximum voltage gain specified in Table 4.2. Furthermore, the MP voltage gain occurs below the specified maximum switching frequency.

Next, the analytical LLC converter voltage gain, shown in Equation (4.1), is compared to a circuit simulated in LTspice using the First Harmonic Approximation (FHA). The LTspice circuit is shown in Figure 4.4, and the implemented LTspice circuit is shown in Appendix A Figure A.1. The circuit in LTspice is simulated with a small-signal AC analysis to determine the voltage gain. The minimum and maximum quality factors are simulated by adjusting the equivalent AC output resistance accordingly.

In Figure 4.3b, both the analytical and LTspice voltage gain curves are presented for the minimum and maximum quality factors. The figure shows almost no difference between the analytical and LTspice results. There is only a slight difference at the voltage gain peak for the Q_{min} curve. As the results from LTspice are similar to those of the analytical results, the analytical design process for the LLC converter is considered valid.

In addition to the voltage gain simulation, a second transient LTspice simulation is performed. This simulation is used to show the steady state behaviour of the LLC converter. The corresponding input



(a) The highlighted points are the minimum switching frequency $f_{s,min}$, and MP is the maximum power point.

(b) A comparison between the voltage gain curve obtained analytically and via LTspice.

Figure 4.3: The voltage gain A_v curve of the resonant tank where f_s is the switching frequency.

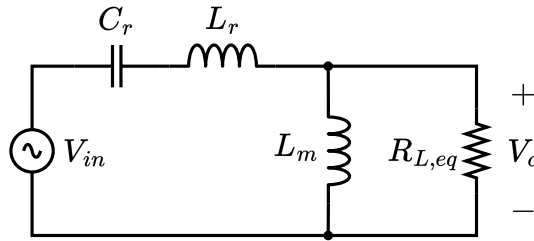


Figure 4.4: The equivalent circuit of an LLC converter.

voltage, AC resistance and frequency are used for the minimum and maximum load conditions. In Figures 4.5a and 4.5b, the minimum and maximum load results are shown respectively. The RMS output voltage is derived from the steady-state waveforms. By recalling that the resonant tank is connected to a full-bridge rectifier, the DC output voltage is calculated from the RMS value using Equation (4.14). With the DC output voltage, the voltage gain of the LLC converter is determined based on the DC in- and output voltage.

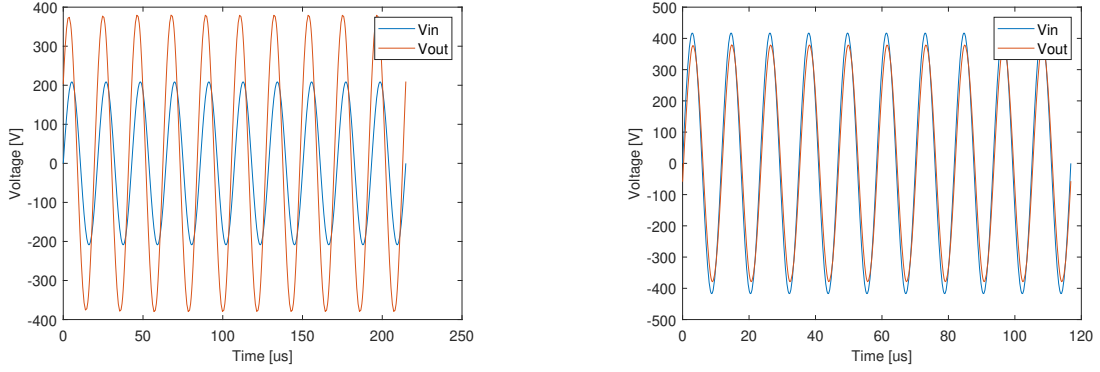
$$V_{dc} = \frac{\pi\sqrt{2}}{4} V_{rms} \quad (4.14)$$

After the calculations, the resulting DC output voltage and the voltage gain are presented in Table 4.4. From the table, it can be seen that at both the mini and maximum load, the DC output voltage is slightly below the desired output voltage. As a result of the lower output voltage, both gains are lower than the required values.

The minimum allowed frequency is used for the LLC converter during the minimum load. Since the maximum voltage gain is slightly lower, the minimum allowed input voltage is higher. Thus, the input voltage range is smaller. In contrast, the lower voltage gain at the maximum load does not influence the input voltage range. The higher voltage gain can be achieved by lowering the switching frequency within the allowed switching frequency range.

Table 4.4: The results from the LTspice steady state waveform analysis.

Load condition	Parameter	Analytical	Transient
Minimum	A_v [-]	1.840	1.819
	$V_{out,dc}$ [V]	300	298.1
Maximum	A_v [-]	0.915	0.907
	$V_{out,dc}$ [V]	300	297.5



(a) Simulation at minimum load $Q = 0.3$ and $f_s = 46.56$ kHz. (b) Simulation at maximum load $Q = 0.6$ and $f_s = 85.59$ kHz.

Figure 4.5: The voltage voltage waveforms of the LLC equivalent circuit simulated in LTspice.

4.2.2. Current Analysis in the Resonant Tank

Moving on to the currents in the resonant tank. Understanding the magnitude and phase of the current flow in the transformer is essential. These transformer currents influence the winding and core losses and the flux density in the transformer core.

By looking at Figure 4.4, the transformer is characterized by the magnetizing inductance L_m and partly by the resonance inductance L_r . The currents in the primary and secondary winding are respectively i_{Lr} and i_{out} . In addition, the magnetizing current i_m is defined by the difference between the primary and secondary winding current. Considering that AC currents flow through the transformer, not only is the magnitude of the currents significant, but also their phase.

The current transfer function between the primary and secondary winding is given by Equation (4.15) where $s = j\omega$. This equation is obtained after performing a relatively simple circuit analysis on Figure 4.4. From the transfer function, it can be seen that the magnetizing inductance and the load resistance influence the transfer behaviour.

$$H_{it}(s) = \frac{i_{out}}{i_{Lr}} = \frac{sL_m}{R_{ac} + sL_m} \quad (4.15)$$

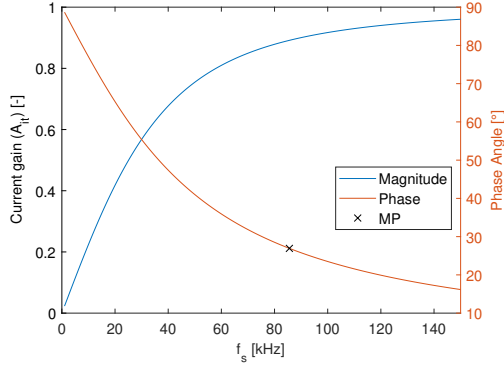
In Figure 4.6a, the current transfer function is plotted for maximum load conditions. At the operating frequency, marked by MP, the expected phase difference between the primary and secondary currents is $\angle 26.93^\circ$. Furthermore, an LTspice simulation is performed to obtain the current waveforms shown in Figure 4.6b. In the figure, a peak is highlighted for both currents. The phase difference can be calculated by taking the time difference between the two peaks and the known switching frequency. The resulting phase difference is $\angle 24.65^\circ$. Comparing the LTspice value with the analytical value, there is a small difference between the two. Nevertheless, as the difference is small, the expected phase difference between the currents is estimated accurately enough for our purposes.

Another important observation from Figure 4.6b is the peak values of the primary and secondary currents. The transformer is simulated in FEMM, and the software uses peak current values to drive the windings, as will be further explained during the transformer design.

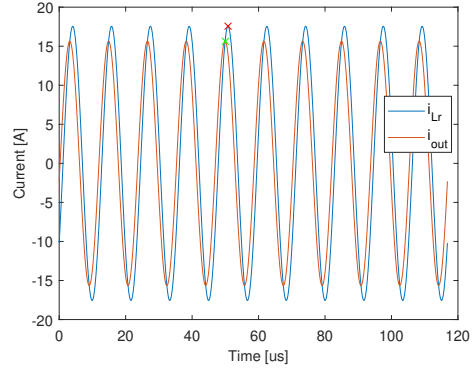
4.3. Conclusion

To summarize, in this section, the LLC converter design process and the influence of key design parameters are presented. First, the influence of the quality factor Q and the chosen value are discussed before moving on to the initial guess for the inductance ratio value m . Afterwards, an iterative process is followed where m is adjusted until the required maximum voltage gain $A_{v,max}$ is obtained within the allowed switching frequency range. After the gain is validated, the last step is calculating the resonance components L_m , L_r and C_r .

Next, the designed LLC converter is analyzed based on the voltage, current gain, and steady-state waveforms obtained from LTspice. When comparing the voltage gains from the transfer function with the steady-state waveforms, the latter showed a slightly lower gain for the same frequencies. This did not impact the performance during maximum load; however, a higher minimum input voltage is required



(a) The magnitude A_{it} and phase of the current transfer between the primary and secondary winding. MP indicates the maximum power point



(b) The current waveforms of the primary and secondary windings respectively i_{Lr} and i_{out} . The simulation is performed with $f_s = 85.59$ kHz and $V_{in,dc} = 327.7$ V.

Figure 4.6: The behaviour of the resonant tank's primary and secondary winding currents at maximum load $Q = 0.6$.

during minimum load operation to achieve the desired output voltage. Consequently, the input voltage range of the LLC converter is decreased.

Lastly, in preparation for the transformer design, the phase difference between the primary and secondary side windings is estimated using the transfer function and LTspice simulations. In addition, steady-state current waveforms from LTspice are used to determine the peak currents in both windings.

To conclude this section, Table 4.5 shows the designed LLC converter characteristics. The next chapter presents the design procedure and resulting design of the transformer.

Table 4.5: The designed LLC converter characteristics.

Parameter	Value
m	3.875
$f_{s,min}$	46.56 kHz
$f_{s,mp}$	85.59 kHz
$f_{s,max}$	92.35 kHz
C_r	146 nF
L_r	30.86 μ H
L_m	88.72 μ H
\hat{I}_{prim}	17.55 A
\hat{I}_{sec}	15.65 A
$i_{p,s} \angle$	26.93°

5

Design of a Coaxial Solenoid Transformer

This chapter aims to design a transformer that meets the inductance criteria for the LLC converter. Models are created for the inductance and power losses to aid with the design of the transformer. Afterwards, the use of the models during the design procedure is explained. Lastly, FEMM is used to refine the transformer design and validate the loss models. Nevertheless, before the modelling starts, the LLC converter inductance parameters are linked to the transformer.

The component at the centre of the satellite CET system is the AC-link to transfer energy from the rotor to the stator as efficiently as possible. In Section 3.4, different AC-link structures were compared, and the rotary transformer was deemed the most suitable for this research. More specifically, the coaxial-solenoid transformer with ferrite core was chosen as the transformer geometry and is shown in Figure 5.1. The primary winding generates a magnetic flux as current flows through it. Due to the high permeability of the ferrite rod, the magnetic flux will be concentrated inside the rod. As the magnetic flux passes through both windings, a coupling is created between the primary and secondary windings, and energy can be transferred.

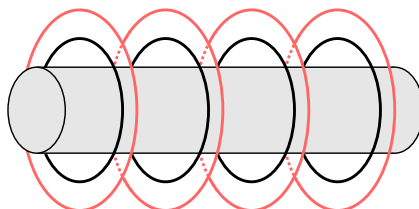
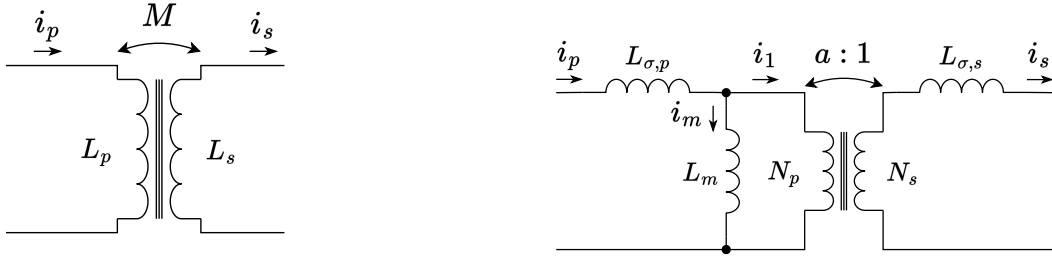


Figure 5.1: A 3D schematic view of the coaxial solenoid transformer with ferrite core and two windings.

In Figure 5.2a, a transformer model is shown based on three physics parameters, namely the mutual inductance, the primary and secondary self-inductance respectively represented by M , L_p and L_s . The primary and secondary coils are formed by the winding of a wire associated with the self-inductance parameters. As mentioned before, a coupling can exist between the coils and this coupling is represented by the mutual inductance. While the physics model accurately describes the transformer and its behaviour, the inductance parameters can not be linked to the LLC converter inductances in the current form.

To circumvent this problem, a second transformer model is introduced and presented in Figure 5.2b. In this model, the real transformer is replaced with an ideal transformer with a turns winding ratio a . The perfect transformer has an infinitely large magnetizing inductance and zero leakage inductances, resulting in an ideal power transfer between the primary and secondary sides. In addition, three inductances are introduced to mimic the behaviour of a real transformer. These inductances are the magnetizing, primary leakage and secondary leakage inductance and are represented by L_m , $L_{\sigma,p}$ and $L_{\sigma,s}$ respectively.

From Figure 5.2b, L_m and $L_{\sigma,p}$ are similar to the inductances L_m and L_r shown in the LLC converter. Therefore, a link is created between the physics and circuit models to relate the LLC converter inductance parameters to the transformer.



(a) The transformer model based on the physics parameters where M , L_p and L_s are respectively the mutual, primary self- and secondary self-inductance.

(b) The transformer model based on circuit parameters where L_m , $L_{\sigma,p}$ and $L_{\sigma,s}$ are, respectively, the magnetizing, primary leakage and secondary leakage inductance. An ideal transformer is introduced with a winding turns winding ratio of a .

Figure 5.2: Two models to represent a transformer.

Both circuits, shown in Figure 5.2a and Figure 5.2b, are analyzed using the flux linkage of the primary and secondary sides. Since both models represent the same transformer, the flux linkage needs to correspond between the models. First, the model in Figure 5.2a is analyzed before repeating the process for the circuit transformer model. Afterwards, the results are compared with each other.

The flux generated by a current flowing through an inductance is given by Equation (5.1). From Figure 5.2a, it is clear that the primary side flux linkage Ψ_p is a result of the primary side inductance L_p . In addition, the coupling between the coils needs to be considered. If the secondary current flows out of the transformer, it opposes the flux linkage on the primary side via the mutual inductance. This is shown in equation Equation (5.2). The same holds for the secondary side flux linkage as shown in Equation (5.3).

$$\Psi = Li \quad (5.1)$$

$$\Psi_p = L_p i_p - M i_s \quad (5.2)$$

$$\Psi_p = L_s i_s - M i_p \quad (5.3)$$

Moving on to the circuit transformer model, shown in Figure 5.2b. First, the primary side flux linkage is determined. The currents flowing into the magnetization inductance L_m and secondary side are given by Equation (5.4) and Equation (5.5) respectively.

$$i_m = i_p - i_1 \quad (5.4)$$

$$i_s = a i_1 \quad (5.5)$$

There are two inductances on the primary side: the primary leakage $L_{\sigma,p}$ and magnetizing inductance. Both inductances contribute to the primary side flux linkage. The primary side flux linkage is obtained by multiplying both inductances with the corresponding currents flowing through them. Afterwards, Equations (5.4) and (5.5) are used to rewrite the resulting equation into terms of the primary and secondary side currents, as shown in Equation (5.6).

$$\Psi_p = i_p L_{\sigma,p} + i_m L_m = (L_{\sigma,p} + L_m) i_p - \frac{L_m}{a} i_s \quad (5.6)$$

The same procedure is applied to the secondary side to obtain the flux linkage. However, the magnetizing inductance is moved to the secondary side before the procedure starts. Using energy conservation, the secondary side magnetizing inductance $L_{m,s}$ is defined by Equation (5.7). With the secondary magnetizing inductance defined, the secondary side flux linkage equation is given by Equation (5.8).

$$L_{m,s} = \frac{L_m}{a^2} \quad (5.7)$$

$$\Psi_s = i_s L_{\sigma,s} + i_{m,s} L_{m,s} = \left(L_{\sigma,s} + \frac{L_m}{a^2} \right) i_s - \frac{L_m}{a} i_p \quad (5.8)$$

The flux linkage equations obtained for the physics model, Equations (5.2) and (5.3), and for the circuit model, Equations (5.6) and (5.8), have a similar form. Due to the similarity, the inductance parameters of the two models are linked to each other as shown by Equations (5.9) to (5.11).

$$L_m = aM \quad (5.9)$$

$$L_p = L_{\sigma,p} + L_m = L_{\sigma,p} + aM \quad (5.10)$$

$$L_s = L_{\sigma,s} + \frac{L_m}{a^2} = L_{\sigma,s} + \frac{M}{a} \quad (5.11)$$

Lastly, the winding turns ratio a needs to be defined to link the two models. As the ideal transformer model is introduced to aid the circuit analysis, the value of a can be set to a desired value. By recalling that the resonant tank in the LLC converter only has a primary side resonance inductor L_r and no inductance on the secondary side, the goal is to eliminate the secondary side leakage inductance $L_{\sigma,s}$. If $L_{\sigma,s}$ is set to zero in Equation (5.11), the desired a value can be extracted. The resulting definition for a is shown in Equation (5.12). As a result, the primary leakage and magnetizing inductance are altered to Equations (5.13) and (5.14) respectively.

$$a = \frac{M}{L_s} \quad (5.12)$$

$$L_{\sigma,p} = L_p - \frac{M^2}{L_s} \quad (5.13)$$

$$L_m = \frac{M^2}{L_s} \quad (5.14)$$

Before moving on to the more detailed transformer modelling, the relevant parameters from the LLC converter are converted to design specifications for the transformer design and presented in Table 5.1. The values in the table serve as design specifications for the transformer. It should be noted that a maximum value is set for the primary leakage inductance $L_{\sigma,p}$. This is done because the primary side series inductance can be increased with an external inductor after measuring the transformer inductances. If the transformer leakage inductance turns out to be too high, there is no way to decrease the inductance.

Table 5.1: The design specifications for the LLC converter characteristics.

Parameter	Value
$f_{s,mp}$	85.59 kHz
$L_{\sigma,p}$	< 30.86 μ H
L_m	88.72 μ H
\hat{I}_{prim}	17.55 A
\hat{I}_{sec}	15.65 A
$i_{p,s} \angle$	26.93°

5.1. Transformer modelling

Next, the transformer model is further refined to relate the physical dimensions to the transformer inductances. When the inductance model is established, the losses in the windings are modelled. Since AC currents flow through the windings, the skin and proximity effect must be considered. The section concludes with a model for the losses generated in the core material called accordingly the core losses.

5.1.1. Inductance Estimation

A solenoid and the magnetic flux lines are shown in Figure 5.3. The figure shows that the magnetic flux path is not clearly defined outside the rod. Therefore, the solenoid is called an open magnetic structure. Consequently, it is difficult to analytically determine the magnetic field strength and flux density in the rod and the solenoid.

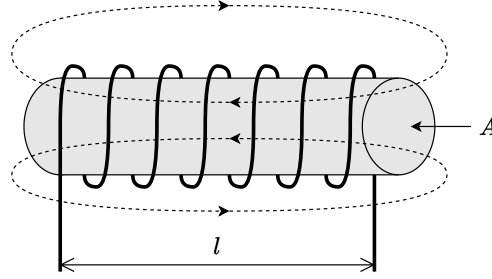


Figure 5.3: A schematic representation of a coil with core and the associated magnetic flux lines.

It is assumed that the magnetic field strength inside the coil is constant to enable the analytical estimation of the inductance. With this assumption, the magnetic field strength H inside the solenoid is given by Equation (5.15) where N is the number of turns, i the current through the coil and l the length of the coil.

$$H = \frac{Ni}{l} \quad (5.15)$$

While the magnetic field strength is constant inside the solenoid, the magnetic flux density of the rod and the air inside the solenoid are different. This is because the flux density depends on the magnetic permeability of a material μ . A common analogy for magnetic permeability is the higher electrical conductivity σ , representing the ability to guide magnetic flux or electrical current respectively. Consequently, a high permeability results in a large flux concentration compared to a low permeability. The permeability is expressed by the magnetic permeability of free space μ_0 and the relative permeability μ_r . For example, the relative permeability of air is $\mu_r = 1$ and non-magnetic materials have a low relative permeability.

Nevertheless, the relative permeability specified for the magnetic rod inside the solenoid can not be used directly. Since the magnetic flux also travels through air, the effective relative permeability of the solenoid is lower than that specified for the material. While there are analytical equations based on empirical data to determine the relative effective permeability $\mu_{r,eff}$ of a solenoid using the ratio between the length and the diameter of the rod, manufacturers of magnetic rods often provide the relative effective permeability.

Back to the relation between the magnetic field strength and the magnetic flux density. Equation (5.16) shows that the flux density is only related to the magnetic field strength via the relative permeability. It should be noted that it is assumed that there is prior magnetization in the magnetic material. From the flux density, the magnetic flux is easily calculated with the area through which the flux flows, as shown in Equation (5.17).

$$B = \mu_0 \mu_{r,eff} H \quad (5.16)$$

$$\Phi = BA \quad (5.17)$$

Lastly, the general equation for the coil self-inductance L is expressed in terms of dimensions, material properties and design parameters by combining Equations (5.15) to (5.17) along with the definition for the inductance, resulting in Equation (5.18). In the following subsections, the self- and mutual inductances of the solenoid transformer are presented in more detail.

$$L = \frac{\Phi N}{i} = \mu_0 \mu_r \frac{N^2 A}{l} \quad (5.18)$$

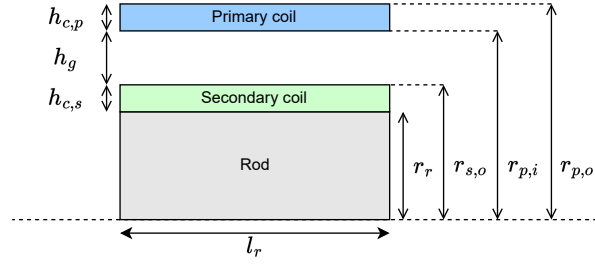


Figure 5.4: An axis-symmetric schematic representation of the solenoid transformer with magnetic core. The dotted line at the bottom indicates the rotational axis.

Self-Inductance

In the detailed inductance derivation, the dimensions of the solenoid transformer are used. Therefore, the transformer dimensions are indicated in Figure 5.4. For now, it is assumed that the length of the winding area l_w equals the rod length l_r . In addition, the primary and secondary windings are defined as the outer and inner coils, respectively, as seen in the figure.

First, the secondary coil self-inductance is calculated as the coil is wound directly onto the rod without any air in between. Equation (5.18) is used where A is equal to the area of the rod with radius r_r and N_s is the secondary winding number of turns. The resulting secondary coil self-inductance is shown in Equation (5.19).

$$L_s = \frac{N_s^2 \mu_0 \mu_{eff} \pi r_r^2}{l_r} \quad (5.19)$$

Second, to derive the primary coil self-inductance, the rod and the air between the rod and the primary coil need to be taken into account. Since copper has a relative permeability of $u_r = 1$, it is considered air in this derivation. The area through which the flux flows is separated into the ferrite rod A_r and the surrounding air A_a . The derivation for the flux in the core is similar to Equation (5.19); however, the primary winding number of turns N_p are used instead of N_s . In addition, A_a is the area of a circular band enclosed by the ferrite rod radius r_r and the inner radius of the primary coil $r_{p,i}$. The resulting primary coil self-inductance is shown in Equation (5.20).

$$L_p = \frac{N_p^2 \pi \mu_0}{l_r} (r_r^2 (\mu_{eff} - 1) + r_{p,i}^2) \quad (5.20)$$

Until now, the length of the winding window was considered equal to the length of the rod. However, the ratio between the two lengths $b = \frac{l_w}{l_r}$ influences the coil's inductance. Figure 5.5 is taken from a ferrite rod manufacturer [42] and shows the influence of the length ratio on the inductance. The influence is called the inductance modifier K and should be used to obtain the adjusted inductance $L_{ad,p,s}$ according to Equation (5.21).

$$L_{ad,p,s} = K L_{p,s} \quad (5.21)$$

Mutual Inductance

Next, the coupling between the primary and secondary coils is discussed based on the mutual inductance between the coils. First, the definition of the mutual inductance is introduced. Let the primary coil be excited to produce a magnetic field strength and magnetic flux. The primary and secondary coils are linked if the magnetic flux passes through a secondary coil. The amount of magnetic flux produced by the primary coil and received by the secondary coil must be determined to define the link between these two coils. The received flux will be called the mutual flux Φ_m . The mutual inductance is then calculated by applying the mutual flux to the general inductance equation along with the number of turns of the secondary coil N_s and the current used to excite the primary coil i_p . As a result, the mutual inductance is defined by Equation (5.22).

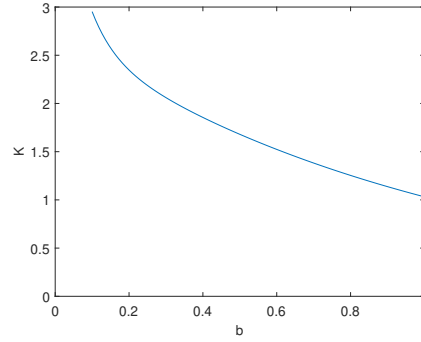


Figure 5.5: The inductance modifier K versus the length ratio b .

$$M = \frac{\Phi_m N_s}{i_p} \quad (5.22)$$

Since the mutual inductance expresses the link between the coils, both coils have the same mutual inductance associated with them. Therefore, the above-presented definition can also be applied to the excited secondary coil to determine the received flux in the primary coil.

Following the same approach as for the coil self-inductance, the mutual flux in the secondary coil is given by multiplying the flux density by the area of the secondary coil. Nevertheless, for determining the magnetic field strength, the primary winding number of turns should used N_p as the primary coil is excited. By including the inductance modifier in the derivation, the mutual inductance is given by Equation (5.23).

$$M = K \frac{N_p N_s \mu_0 \mu_{eff} \pi r_r^2}{l_r} \quad (5.23)$$

A final transformer characteristic is the coupling factor or coefficient k . This coefficient indicates how well the transformer coils are coupled with each other. Using the three physics quantities of the transformer mutual, primary self- and secondary self-inductance, the coupling coefficient is determined by Equation (5.24). It should be noted that coupling is always $0 < k < 1$.

$$k = \frac{M}{\sqrt{L_p L_s}} \quad (5.24)$$

5.1.2. Winding Losses

The transformer's loss needs to be modelled to evaluate its performance and see if the efficiency requirement is met. Besides validation, if the design requirements are met, the power loss model also provides insights into the origin of the losses. The transformer losses are characterized into two types: core and winding losses. The latter will be discussed in this subsection.

The DC resistance of a wire is determined by its length l , the conductor area A_c , and the conductivity of the conductor σ . This research uses round wires, and therefore, the area given by the conductor diameter d_c . Equation (5.25) shows the DC resistance of a wire per length.

$$R_{dc,pl} = \frac{1}{\sigma A_c} = \frac{4}{\sigma \pi d_c^2} \quad (5.25)$$

Skin Effect

Under DC conditions, the current density is evenly distributed inside the conductor. However, when an AC current flows through the conductor, an electric field is induced inside the conductor [43]. From the induced electric field, eddy currents are generated inside the conductor. These eddy currents oppose and enhance the current flow respectively at the centre and the edges of the conductor. As a result, the current density is higher at the conductor's edge than at the centre's. This phenomenon is called the skin effect.

A measure for this effect is the skin depth δ and represents the distance from the conductor edge where the current density is $1/e$ of the maximum value [43]. Equation (5.26) shows the skin depth dependency on the frequency and the conductor conductivity. When the frequency is increased, the skin depth decreases, and consequently, the current density is concentrated more on the edges of the conductor.

$$\delta = \frac{1}{\sqrt{\pi\mu_0\sigma f}} \quad (5.26)$$

[43] presents a factor $F_R = R_{ac}/R_{dc}$ where the effect of the skin effect on the resistance is included. Equation (5.27) shows the dependency of F_R on the skin depth.

$$F_R = \frac{\zeta}{4\sqrt{2}} \left(\frac{ber_0(\zeta)bei_1(\zeta) - ber_0(\zeta)ber_1(\zeta)}{ber_1(\zeta)^2 + bei_1(\zeta)^2} - \frac{bei_0(\zeta)ber_1(\zeta) + bei_0(\zeta)bei_1(\zeta)}{ber_1(\zeta)^2 + bei_1(\zeta)^2} \right) \quad (5.27)$$

Where ζ , shown in Equation (5.28), is the ratio of the strand diameter d_s and the square's diagonal where the sides have the skin depth for length. Furthermore, $ber_\nu(x)$ and $bei_\nu(x)$ are called Kelvin functions and they are the real and imaginary parts respectively of the ν^{th} order Bessel function of the first kind shown in Equation (5.29) [43].

$$\zeta = \frac{d_s}{\sqrt{2}\delta} \quad (5.28)$$

$$J_\nu \left(xj^{\frac{3}{2}} \right) = ber_\nu(x) + jbei_\nu(x) \quad (5.29)$$

To obtain the power losses originating from the skin effect, Equation (5.30) is used where \hat{I} represents the peak current in the winding and n_s the number of strands. It should be noted that these skin effect losses are in a per-length unit. If a solid wire is used instead of a Litz-wire, $n_s = 1$ and $R_{dc,pl}$ is calculated with the conductor diameter d_a .

$$P_{S,pl} = R_{dc,pl} F_R(f) \frac{\hat{I}^2}{n_s} \quad (5.30)$$

Proximity Effect

Moving on to the proximity effect in windings. A magnetic field is created outside the wire when a current flows in a conductor. This magnetic field influences nearby conductors as eddy currents are induced. Like the skin effect, the eddy currents shift the current density away from the centre. However, with the proximity effect, the direction of the shift is dependent on the direction of the magnetic field.

Since Litz wires are used in this design, the proximity effect can be split into an external and internal effect. The external proximity effect originates from the magnetic field of other conductors H_e and acts as described before. In addition, the internal proximity effect occurs due to the multiple strands inside a single bundle. These strands influence each other via the internally created magnetic field H_i in the same manner neighbouring conductors influence each other. The total proximity effect losses are calculated by combining the internal and external proximity effects.

Again, [43] presents a similar factor G_R for the proximity effect resistance as the skin effect. In Equation (5.31), the factor G_R is defined and d_s is the strand diameter.

$$G_R = -\frac{\zeta\pi^2 d_s^2}{2\sqrt{2}} \left(\frac{ber_2(\zeta)ber_1(\zeta) + ber_2(\zeta)bei_1(\zeta)}{ber_0(\zeta)^2 + bei_0(\zeta)^2} + \frac{bei_2(\zeta)bei_1(\zeta) - bei_2(\zeta)ber_1(\zeta)}{ber_0(\zeta)^2 + bei_0(\zeta)^2} \right) \quad (5.31)$$

In Equations (5.32) and (5.33) respectively, the external and internal proximity losses per-length unit are shown. As the external proximity losses are generated by the magnetic field from other conductors, only the external magnetic field strength is required for the calculation. Conversely, as the magnetic field inside the Litz wire is generated by the current flowing through the strands, the current through the wire is required. d_a represents the outer diameter of the Litz-wire and not the strand diameter.

$$P_{P,e,pl} = n_s R_{dc,pl} G_R(f) \hat{H}_e^2 \quad (5.32)$$

$$P_{P,i,pl} = n_s R_{dc,pl} G_R(f) \frac{\hat{I}^2}{2\pi^2 d_a^2} \quad (5.33)$$

The total proximity losses per length are obtained by combining the internal and external proximity losses. A last note on the proximity losses: if a solid wire is used instead of a Litz-wire, $n_s = 1$ and $R_{dc,pl}$ and $G_R(f)$ are calculated with conductor diameter d_a . In addition, the internal proximity effect losses are zero as there is effectively only a single strand. Next, the second type of transformer loss is presented, namely the core loss.

5.1.3. Core Losses

The magnetization of the core material causes the losses in the core P_v during operation. This magnetizing is represented in the equivalent circuit model by the magnetization current i_m . When the current is increased, so will the magnetization and the flux density inside the core. In the magnetization process, losses are created due to hysteresis P_h and eddy current P_e losses as seen in Equation (5.34).

$$P_v = P_h + P_e \quad (5.34)$$

First, the eddy current losses are briefly discussed. The eddy currents induced in the core are similar to the external proximity effect discussed before. A magnetic field is established in the core material due to the excitement of the windings around it. During a switching cycle, the magnetic field and the AC current change. Since the core has a finite conductivity, eddy currents are introduced in the core and generate losses in the form of heat [43]. The impact of the eddy current losses will be discussed further in Section 5.2, where the core material is selected.

Second, the hysteresis losses are caused by the magnetic response of the core material to the external magnetic field. In Figure 5.6, a typical relation between the flux density and the magnetic field is shown, called the BH-curve, for a soft magnetic material. If the core is not magnetized before an external magnetic field is applied, the dotted line represents the material's response. Interestingly, when the external field is removed after the magnetization, the core flux density does not return to zero. Instead, there is a residual flux density B_r in the core. A negative magnetic field must be applied to remove the core's magnetization. From these observations, it can be concluded that the magnetization of a magnetic core depends on the previous state or magnetization. Therefore, the path in Figure 5.6 is often called the hysteresis loop.

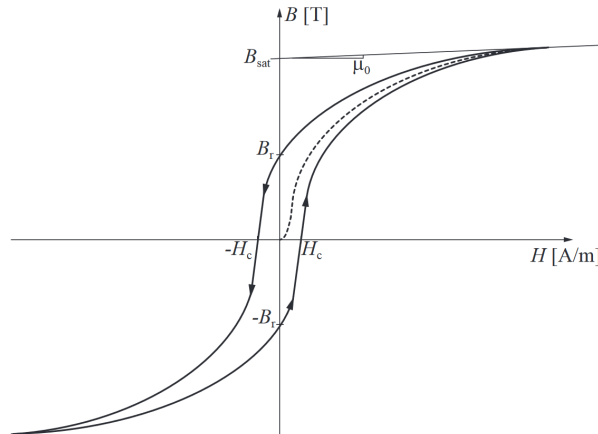


Figure 5.6: An example of a BH-curve from a soft magnetic material, taken from [43].

The core's magnetization is often presented as a singular value for the whole core. Nevertheless, the core exists of small magnetic sections with different magnetizing magnitudes and directions [43]. For example, the small magnetic sections are magnetized if the core has no magnetization. When the magnetization of all these small magnetic sections is added, the total magnetization will be zero. The behaviour of the magnetic sections during the magnetization results in losses in the form of heat. The small magnetic sections must change their magnetization magnitude and direction by applying an external magnetic field to the core. These changes to the small magnetic sections cause hysteresis losses

in the core. The energy loss generated by the hysteresis is calculated by integrating the flux density with respect to magnetic field strength over a hysteresis loop, as shown in Figure 5.6. Mathematically, this is represented by Equation (5.35).

$$W = \oint B dH \quad (5.35)$$

However, due to the hysteresis, the analytical BH-curve model of soft magnetic materials is complicated. Therefore, a standard method to estimate the hysteresis losses uses the Steinmetz equation, shown in Equation (5.36). The Steinmetz coefficients α , β and c are obtained via curve fitting the equation onto empirical loss data for a specific core material. Manufacturers of magnetic materials often provide the core loss curves for varying temperatures, frequencies and flux densities. The power loss curves can be applied to any core using the material, as the losses are quantified as power loss densities.

$$P_h = cf^\alpha \hat{B}^\beta \quad (5.36)$$

The magnetic field and flux density are required to calculate the winding and core losses. As highlighted previously, the open magnetic structure of the solenoid transformer makes the analytical modelling of the magnetic field strength and flux density difficult. Therefore, in the next section, the use of FEMM is discussed to extract the required quantities and validate the inductance of the transformer.

5.1.4. Foundation of FEMM and Simulation Model

FEMM is a software program that solves 2d magnetic problems. The program can apply the FEM to planar or axisymmetric geometries. First, the method used by FEMM to obtain the flux density B and magnetic field H is briefly presented before moving to the application of FEMM in this research.

Maxwell's equations related to the magnetic field are the basis for the magnetic solver for the FEMM program. The relevant equations are shown in Equations (5.37) and (5.38) where J is the current density. Furthermore, the material's permeability determines the relation between the magnetic field and flux density as seen in Equation (5.39).

$$\nabla \times H = J \quad (5.37)$$

$$\nabla \cdot B = 0 \quad (5.38)$$

$$B = \mu H \quad (5.39)$$

To solve the above differential equations, FEMM introduces a magnetic vector potential A defined by Equation (5.40). By combining Equations (5.37) to (5.40) the magnetic vector potential is directly related to the current density as shown in Equation (5.41). Based on the current provided by the user, FEMM numerically find A such that Equation (5.41) is satisfied. The resulting magnetic potential vector determines the flux density and magnetic field strength. For more information regarding the FEMM program, the reader is referred to [44].

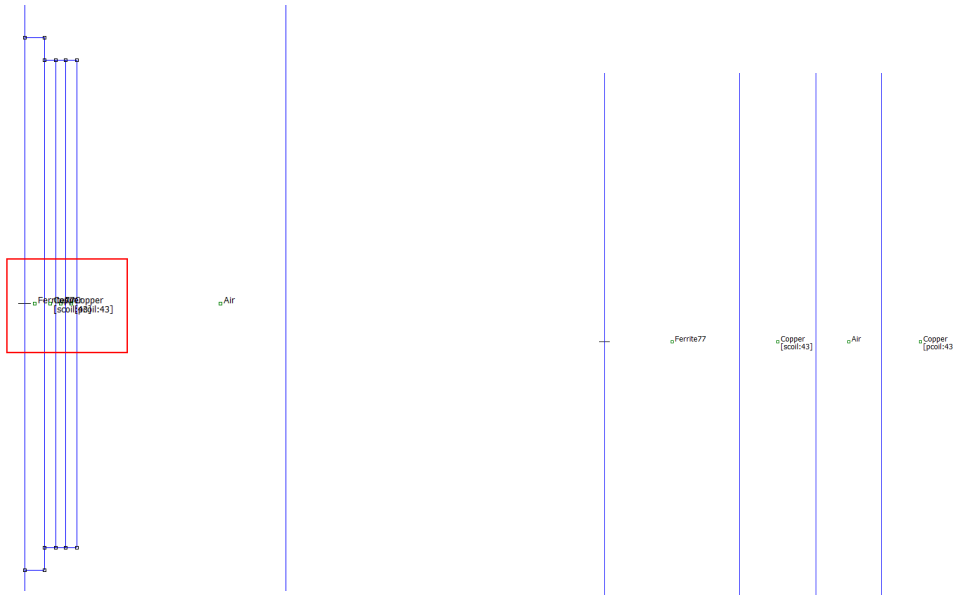
$$B = \nabla \times A \quad (5.40)$$

$$\nabla \times \left(\frac{1}{\mu(B)} \nabla \times A \right) = J \quad (5.41)$$

Transformer Model

Next, the implementation of the transformer model in FEMM is discussed. In Figure 5.7, the solenoid transformer is shown with the magnetic rod and both coils. Even though the transformer is designed for outer space, the space around the transformer is labelled as air since vacuum and air have the same magnetic properties.

A MATLAB script is created to draw the transformer FEMM model based on input parameters to enable rapid and automatic modelling of different transformers. The communication between FEMM and MATLAB is established via the 'OctaveFEMM' toolbox in the MATLAB environment. This toolbox contains commands used in a MATLAB script to perform actions in FEMM. Besides the drawing of



(a) The solenoid transformer consists of the rod and primary and secondary coils. The leftmost vertical line represents the symmetry axis.

(b) The content of the red square to make the region indications readable.

Figure 5.7: The model for the coaxial solenoid transformer in FEMM where the horizontal and vertical axes represent the radial and axial directions, respectively.

the models, there are also commands to simulate the model and extract outputs from the resulting solution. The next part of this section further explains the use of the simulation results concerning the inductance and power losses.

Starting with the inductance validation using FEMM. During the analytical derivation of the inductances, assumptions are made to simplify the equations. These simplified analytical equations, are used to get an estimation for the number of turns required to meet the inductance requirement, this will be further explained in Section 5.3. To check and possibly refine the transformer geometry and number of turns, the results from FEMM are used.

By, e.g. exciting the primary winding with a current while the secondary winding current is set to zero, the primary and mutual inductance can be extracted from FEMM. The circuit properties tool in FEMM shows the flux linkage λ for both the primary and secondary coils. With the use of Equations (5.42) and (5.43) and the applied current, the primary, secondary and mutual inductance are determined.

$$L_{p,s} = \frac{\lambda_{p,s}}{i_{p,s}} \quad (5.42)$$

$$M = \frac{\lambda_{p,s}}{i_{s,p}} \quad (5.43)$$

Next, the procedure for extracting the magnetic field strength and flux density from FEMM is presented. For this simulation, the primary and secondary currents are set to their respective values during the specified load, including the phase difference of the currents. From the simulation results, B and H can be extracted at a specified point via a MATLAB command.

The flux density is required for the calculation of the core losses. Taking the flux density at a single point is insufficient for the core losses, as the flux density is not uniform in the core. To circumvent this problem, the core is divided into segments, as shown in Figure 5.8, and the flux density is extracted from the centre of the segment. Next, the power losses are calculated per segment and added to obtain the total core losses. Unfortunately, FEMM does not provide a direct method to get the core losses from the simulation results. Therefore, only the Steinmetz equation is used to determine the core losses.

For the calculation of the winding losses, the magnetic field strength at the location of the wires is required. As shown in Figure 5.8, the centre's location for every turn in the coils is estimated. The

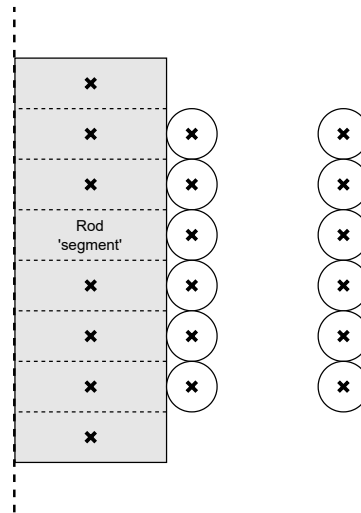


Figure 5.8: A schematic representation where the crosses are the locations where the flux density and magnetic field strength are extracted. The dashed line represents the symmetry axis.

magnetic field strength is extracted from the simulation at these locations and used to determine the external proximity effect at each turn individually. The losses of each turn in a coil are combined, resulting in the total winding loss for the coil.

In contrast to the core losses, FEMM does offer a method to extract the skin and proximity effect losses per coil. The winding area of a coil can be selected in the simulation results. After choosing the area, a resistive and proximity effect loss integration can be performed to obtain the skin and proximity effect losses, respectively.

The key takeaways from this section are the models introduced to estimate the inductance based on transformer dimensions, the number of turns, and the models for the winding and core losses. In addition, the FEMM program is briefly introduced, and the aid in the design and validation steps are presented. The following section introduces the wire and core materials considered for the transformer before moving on to the design process.

5.2. Wire and Core Material Selection

The wire and core material need to be defined before the transformer's design process can start. This section presents the chosen wire and core material and the reasoning behind the choice. First, the wire selection is discussed before moving on to the magnetic rod selection.

5.2.1. Wire Considerations

The ESP lab at the TU Delft has worked with wires from Elektrisola before, and spare wires are present at the lab. Therefore, wires from Elektrisola are considered. The wire selection will be based on two considerations: thermal and winding losses.

Starting with the former, the thermal performance of the wires is related to the current density in the conductor. By having a lower current density, the conductive losses are reduced. [45] advises a current density between 2 A/m^2 to 4 A/m^2 for natural air cooling of EM windings. Since the design in this research is meant for space applications and the presence of air for thermal conduction is uncertain, the aim for the current density is set below 3 A/m^2 . Based on the RMS current in the primary winding $I_{p,rms} = 12.41 \text{ A}$, the minimum conductor area required is 4.14 A/m^2 .

Another consideration for the wire is the type of wire used. Here, two types are differentiated: solid and Litz-wires. Solid wires consist of a single strand of copper, while Litz wires consist of multiple strands. In Figure 5.9, the power losses per unit length are shown for a solid wire and multiple Litz wires. The figure shows that for frequencies below 40 kHz , all three Litz-wires show lower losses compared to the solid wire.

Nevertheless, at higher frequencies, the Litz wires with more strands perform better than those with a low amount of strands. The Litz-wire with the least strands has more losses than the solid wire. As

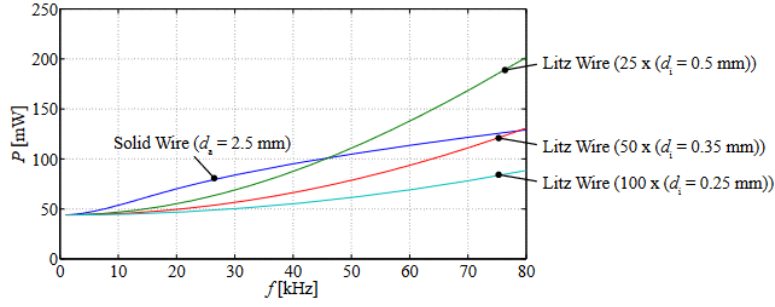


Figure 5.9: A comparison of the combination of skin and internal proximity effect versus frequency for different wire types. The figure is provided in [43].

the transformer operates at maximum power with a frequency of 86 kHz, the Litz-wire is selected for the design.

Next, the available Litz-wires from Elektrisola are reviewed to find a suitable match. From the wires, the smallest possible diameter was chosen to reduce the size of the transformer. In Table 5.2, the specifications of the chosen wires are shown.

Table 5.2: The specifications of the Litz-wire from Elektrisola.

Parameter	Value
Number of strands (n_s)	35
Strand diameter (d_s)	0.4 mm
Conductor cross-section (A_c)	4.3982 mm ²
Outer diameter (d_a)	3.516 mm

5.2.2. Magnetic Rods

The ferrite manufacturer Fair-rite was considered for the magnetic rods due to the large variety of rod sizes available. More specifically, the rods in stock at the distributor DigiKey were considered as these components could be ordered and delivered quickly. Unfortunately, due to this last constraint, only five materials were available for the ferrite rods. After inspecting the power loss curves of the remaining materials, three more were excluded as the power loss curves were specified for frequencies in the MHz range. The remaining materials for the ferrite rods are 77 and 78. From these two materials, the available rods' dimensions, considered in this research, are shown in Appendix B Table B.1.

On the Fair-rite website, the power loss curves are available for both material 77 and 78 and are shown respectively in Appendix B Figures B.1a and B.1b. From the power loss curves at a frequency of $f = 100$ kHz, the Steinmetz coefficients are estimated with the MATLAB curve fitter toolbox. [46] provides ranges for the exponential coefficients $1 < \alpha < 3$ and $2 < \beta < 3$ in the Steinmetz equation, and for the last coefficient, a range of $1 < k < 10$ is set. The resulting Steinmetz coefficients are shown in Table 5.3 along with the Root Mean Square Deviation (RMSD) compared to the datasheet value.

The datasheet and Steinmetz curves are compared in Figures 5.10a and 5.10b for materials 77 and 78, respectively. It should be noted that the difference at low flux densities seems significant in Figure 5.10a; however, due to the logarithmic scale, small variations at low power losses are enlarged by the scaling. Furthermore, as the RMSD are small, the approximation is considered valid for determining the core losses.

Table 5.3: The Steinmetz coefficients obtained with the MATLAB curve fitter toolbox with the RMSD compared to the datasheet values and the maximum peak flux density \hat{B}_{max} .

Material	α	β	c	RMSD	\hat{B}_{max}
77	1	2.155	0.3	6.3937	0.2 mT
78	1	2.3538	0.2722	2.3549	0.2 mT

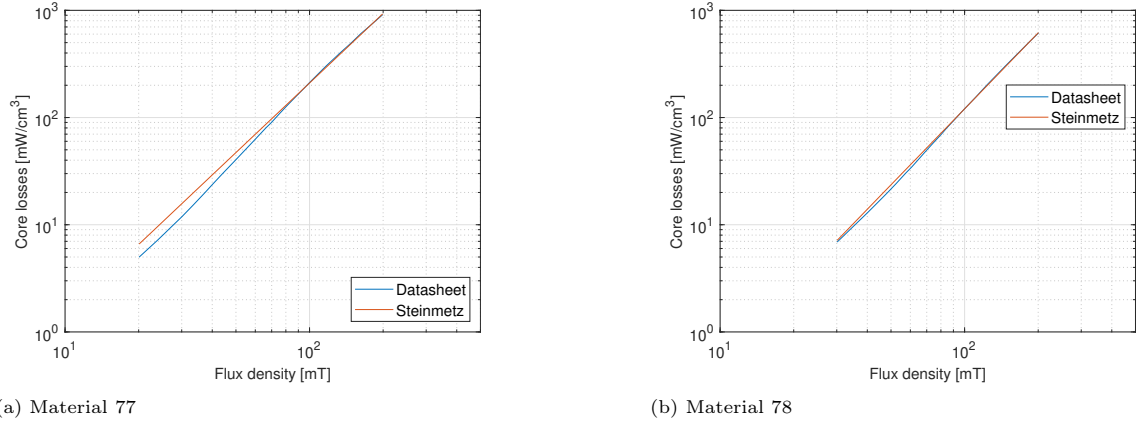


Figure 5.10: The power loss curve from the material datasheet compared to the Steinmetz equation approximation. Both material curves are evaluated at $f = 100$ kHz.

With the models for the transformer's sizing in place and the selection of the wire and rods completed, it is time to move on to the next step. The design procedure for the transformer is presented in the following section.

5.3. Design Procedure

This section introduces the design procedure for transformer sizing. First, the important assumptions that impact the design of the transformer are presented below.

1. The primary and secondary number of turns equals $N_p = N_s$. As a result, the mutual inductance is assumed to be similar to the secondary self-inductance $M \approx L_s$.
2. The primary leakage inductance should be lower than the series inductance $L_{\sigma,p} < L_r$. The value cannot be lowered if the leakage inductance exceeds the series inductance requirement. Therefore, the missing series inductance will be compensated with an external inductor.
3. A single-layer winding is considered to reduce the overall diameter of the design.
4. The window length should be smaller than the total rod length $l_w < l_r$ such that the secondary coil can be directly wound around the ferrite rods.
5. The air gap between the coils is set to $h_g = 3$ mm to enable space during assembly [21].

Next up, the design steps are explained in more detail to generate an understanding of the flowchart presented in Figure 5.11. The explanation starts with the analytical estimation of the required number of turns.

5.3.1. Analytical Transformer Sizing

While FEMM is relatively quick with its simulations, it still takes longer than a simple analytical model. Therefore, the analytical model obtains a starting point for the optimization with FEMM. Combining the two methods reduces the overall simulation time for FEMM.

Before estimating the transformer sizing, the magnetizing inductance requirement from the LLC converter needs to be linked to the analytical model. First, the mutual and magnetizing inductance equations are repeated for clarity in Equations (5.44) and (5.45) respectively.

$$M = K \frac{N_p N_s \mu_0 \mu_{ef} f \pi r_r^2}{l_r} \quad (5.44)$$

$$L_m = \frac{M^2}{L_s} \quad (5.45)$$

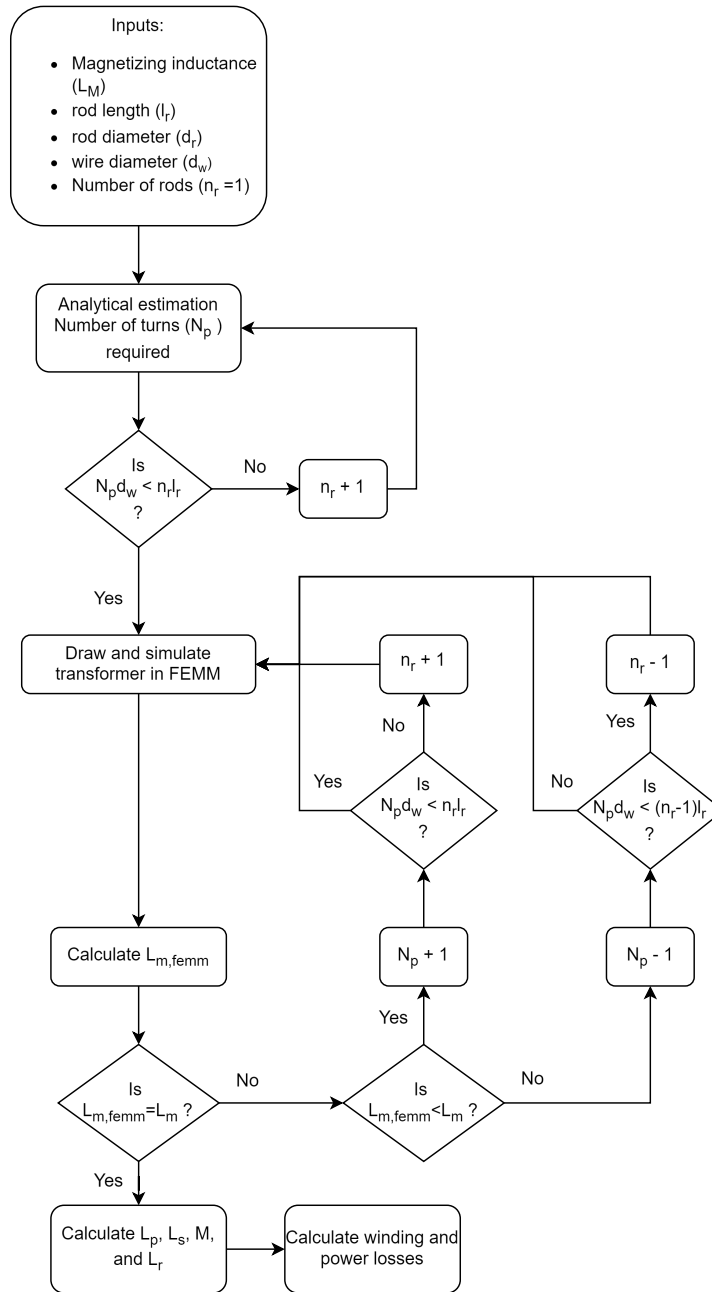


Figure 5.11: The design flowchart for the transformer sizing using the analytical inductance estimation and FEMM.

Using the first assumption specified above, the mutual and magnetizing are considered equal, as shown in Equation (5.46). When Equations (5.44) and (5.46) are combined, and the magnetizing inductance is related to the transformer dimensions and the number of turns Equation (5.47).

$$L_m = M \quad (5.46)$$

$$L_m = K \frac{N_p^2 \mu_0 \mu_e f f \pi r_r^2}{l_r} \quad (5.47)$$

For each rod considered for the transformer, the starting assumption is that a single rod is used $n_r = 1$. Next, the maximum number of turns is determined to make the winding window length smaller than the rod length. Afterwards, the minimum number of turns is defined as half the maximum number of turns rounded down. The inductance modifier K and the magnetizing inductance L_m are

calculated for every number of turns between and including the minimum and maximum. If the required magnetizing inductance can not be acquired with a single rod, the number of rods increases by one and the calculations are repeated. After the necessary number of rods and turns are found to achieve the required magnetizing inductance, the analytical parameters of the rod transformer are saved and passed onto the FEMM model.

5.3.2. FEMM Transformer Refinement and Power Losses

The starting parameters for the FEMM model are the results of the analytical estimation. First, these starting parameters are used as input to draw the model in the FEMM environment and simulate the inductance. The primary and secondary self- and mutual inductance are calculated using the simulation results. With the obtained inductances, the magnetizing inductance is calculated and compared to the required magnetizing inductance.

If the FEMM magnetizing inductance $L_{m,femm}$ is within 5% of the required magnetizing inductance, the design is considered optimized. The last step is calculating the leakage inductance and saving the transformer parameters.

In contrast, the design needs to be refined if the FEMM magnetizing inductance falls outside of the 5% margin. When $L_{m,femm} < L_m$, the number of turns increases by one. Afterwards, the total winding window length is compared to the total rod length and the number of rods is increased if the window length exceeds the rod length. The number of turns decreases should $L_{m,femm} > L_m$. Again, the new winding window length is compared against the rod length; however, in this case, the comparison determines if the number of rods can be reduced. If the new winding window is smaller than the rod length with a single rod removed, the number of rods is decreased by one. Should the opposite be true, the number of rods remains the same.

It should be noted that the margin of 5% might be too tight for the optimization. This occurs when the increase and subsequent decrease cause an overshoot and undershoot of the magnetizing inductance, respectively. For this scenario, a check is built into the optimization that tracks if the number of turns is increased and not subsequently decreased. When the number of rods is adjusted, the checks are reset to prevent the optimization from stopping prematurely.

After the transformers' sizing with different rod dimensions is completed, the power losses are calculated for the final transformer dimensions. The winding and core losses are calculated analytically using the methods presented in Sections 5.1.2 and 5.1.3 respectively. In addition, the magnetic field strength and flux density required for the analytical calculations are extracted from the FEMM simulation results as discussed in Section 5.1.4 along with the winding losses obtained in FEMM.

5.4. Results

In this section, the results from the transformer sizing are presented and analyzed. During the analysis, the assumptions stated at the beginning of Section 5.3 are revised and compared to the results. Furthermore, the analytical and FEMM sizing are compared. To conclude the section, the power losses of the different transformer designs are presented and analyzed.

5.4.1. Analytical vs FEMM Sizing

First, the analytical and FEMM transformer sizing are compared. In Table 5.4, the results for both sizing methods and the rod dimensions and material are presented. One immediately clear observation from the table is the more considerable difference between the analytical and FEMM sizing for rods with small diameters. This difference can be explained by the analytical estimation for the rod effective permeability μ_{eff} . A curve fitter is used to obtain the coefficient for Equation (5.48) based on the data from the manufacturer. The data provided is defined between $1 < l_r/d_r < 10$. Looking at the first transformer geometry, the length over diameter ratio results in $l_r/d_r = 35$, far outside the defined range for the function. In addition, $b = 1.5252$ for Equation (5.48) resulting in a fast increase in u_{eff} for large values of l_r/d_r . Therefore, it is likely that the unknown behaviour of the rod's effective permeability for values $l_r/d_r > 10$ is the cause for the overestimating of the magnetizing inductance.

$$\mu_{eff} = a \left(\frac{l_r}{d_r} \right)^b + c; \quad (5.48)$$

In contrast to the rods with smaller diameters, the rods with larger diameters have a smaller differ-

ence between the analytical and FEMM sizing. Looking at the last transformer in Table 5.4, the length over diameter ratio is $l_r/d_r = 13.4$. This value is closer to the range for which the effective permeability is defined. As a result, the analytical estimation of the inductance is closer to the FEMM value.

Table 5.4: The analytical and FEMM transformer sizing results for different rod geometries.

Design number	Rod specifications			Analytical			FEMM		
	d_r [mm]	l_r [mm]	Material	n_r	N_p	L_m [μ H]	n_r	N_p	L_m [μ H]
1	5	35	78	5	46	90.05	9	80	89.91
2	6.35	25.4	77	6	43	88.41	9	58	96.97
3	6.35	38.1	77	4	43	88.41	6	55	92.56
4	6.35	40	78	4	43	86.32	6	57	92.57
5	8	38.1	77	4	41	85.80	5	45	91.31
6	8	45	78	4	43	90.21	5	47	98.57
7	9.45	31.75	77	5	40	84.43	6	41	95.43
8	9.45	38.1	78	4	40	86.43	5	42	96.63
9	9.45	50.8	77	3	40	86.43	4	40	95.69
10	9.5	41.28	77	4	41	89.25	4	43	91.44
11	9.5	70	78	3	43	87.51	3	40	93.47
12	12.3	31.75	77	5	39	89.04	5	39	90.13
13	12.3	41.28	77	4	39	86.78	4	39	94.19

5.4.2. Winding Losses

Moving on to the winding losses in the primary and secondary coils. The transformer sizes obtained from FEMM are used to evaluate the power losses. The transformer models are drawn in the FEMM software and the corresponding load currents are applied to the primary and secondary winding. The phase shift between the two currents is taken into as well.

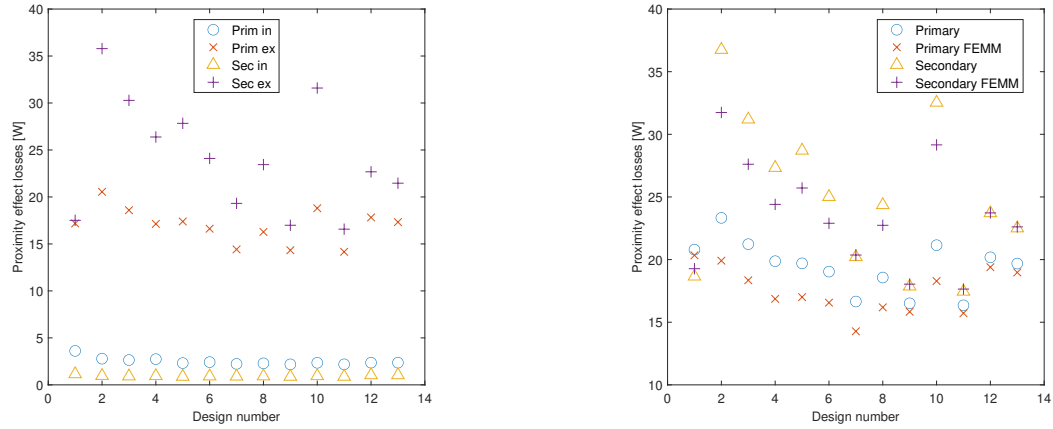
Figure 5.12a shows the internal and external proximity losses obtained from the analytical calculation method. From the figure, it can be seen that the external proximity losses are significantly higher compared to the internal proximity losses. This can largely be explained by the fact that the magnetic field strength is relatively large for both coils, e.g. for design number 13 the minimum magnetic field strength is $H \approx 3000$ A/m. The high magnetic field strength is a consequence of the relatively large number of turns, as each turn increases the magnetic field strength for the same current.

Furthermore, in Figure 5.13a, it can be seen that the magnetic field strength is more considerable for the secondary coil compared to the primary coil. This is explained by the magnetic field strength spikes at the boundary between the ferrite material and the air. This difference in magnetic field strength explains the larger external proximity losses for the secondary coil than the primary coil. When the magnetic field is discarded, it is expected that the primary coil experiences higher winding losses due to the larger radius of the turns, resulting in a longer wire. This is seen when looking at the internal proximity effect losses in Figure 5.12a.

Another observation from Figure 5.13a is that the highest magnetic field strength is located at the corners of the rod. These corners should be avoided when considering the placement of winding turns to prevent excessive external proximity losses. Alternatively, a rod with smoother edges can be chosen to reduce the magnetic field concentration at the corners of the rods.

The total proximity losses are the largest for the secondary coil for all designs except for design 1, as seen in Figure 5.12b. Furthermore, the difference between the analytical and FEMM method reduces as the design number increases, corresponding to an increase in the diameter of the rods. The exceptions are the designs with numbers 4,6,8 and 11, which use the rod material 78. For rod material 78, the proximity losses prove to be significantly higher than designs with material 77 and similar dimensions.

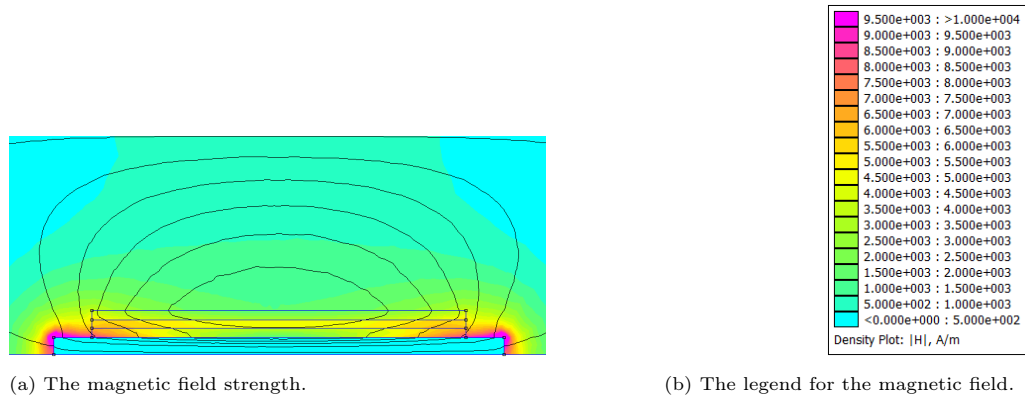
Moving on to the skin effect losses as shown in Figure 5.14a. For the skin effect losses, the analytical



(a) The internal and external proximity effect losses obtained from the analytical calculation method.

(b) The total proximity effect losses for the analytical method and FEMM.

Figure 5.12: The winding losses due to the proximity effect for both the primary and secondary coils.



(a) The magnetic field strength.

(b) The legend for the magnetic field.

Figure 5.13: FEMM simulation of design 13 under load conditions.

and FEMM calculation methods show good correspondence with each for all the simulated designs. As mentioned before, primary coil skin effect losses are expected to be higher due to the increased length compared to the secondary coil.

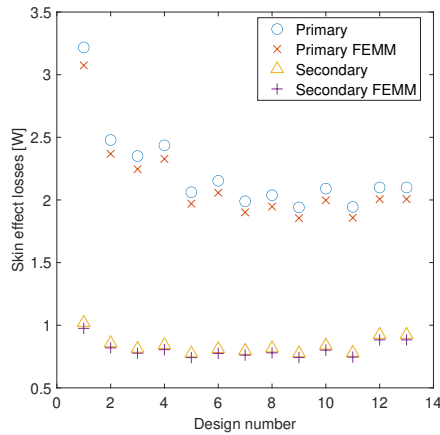
Lastly, the total winding losses are shown in Figure 5.14b. The total winding losses combine the skin and proximity effect losses. The external proximity losses mostly dominate the total winding losses, and therefore Figures 5.12b and 5.14b have a similar distribution. If the transformer needs to be optimized to reduce the power losses, the external proximity losses should be considered first.

5.4.3. Core Losses

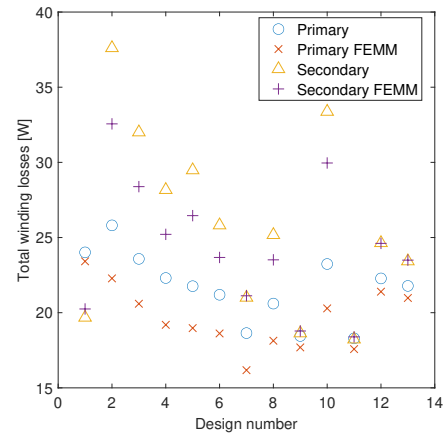
Next up, the core losses of the transformer are presented. As mentioned in Section 5.1.4, FEMM does not contain a method to extract the hysteresis losses directly from the simulation. Consequently, only the results from the analytical model are discussed.

Before the core losses are calculated, the maximum flux density in the rods needs to be investigated. By recalling that the core loss curves from the datasheet are only specified for flux densities up to 200 mT, a limit is set on the maximum flux density in the rod for valid core calculations. In Figure 5.15a, the peak flux density for the different transformer designs is shown. The figure shows that only designs 12 and 13 have flux densities below 200 mT. Interestingly, both designs have the same diameter but different lengths, and the peak flux density is slightly higher for design 13 than design 12.

The flux density distribution along the rods' centre is shown in Figure 5.15b. The flux is mainly concentrated at the centre of the rod. It should be noted that the minimum flux density for which the power losses are specified is 20 mT. Designs 12 and 13 show slightly above the minimum flux density;



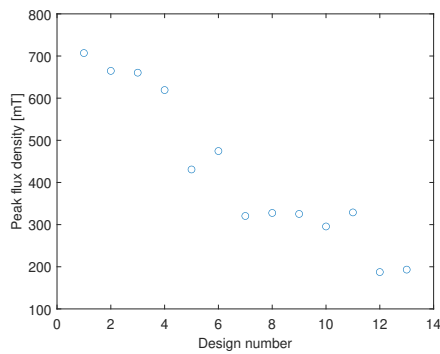
(a) The skin effect losses.



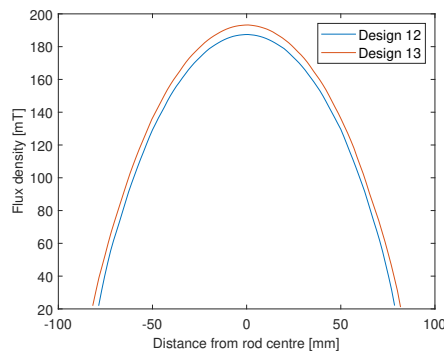
(b) The total winding losses.

Figure 5.14: The winding losses for the analytical and FEMM calculation methods for both the primary and secondary coils.

therefore, the core losses can be calculated over the whole rod.



(a) The maximum flux density for the different transformer designs.



(b) The flux density distribution in the rod for designs 12 and 13 from Table 5.4.

Figure 5.15: The flux density obtained from FEMM simulations.

To calculate the core losses, the core is segmented into 100 pieces. At the centre of each piece, the flux density is determined from the FEMM simulation result. Next, the Steinmetz equation is applied to each segment using the corresponding flux density. To convert the power loss density to power loss per segment, the result of the Steinmetz equation is multiplied by the segment's volume. Lastly, the segments are added to obtain the total core power losses.

The resulting core losses are presented in Table 5.5. Transformer design 12 has a slightly lower core loss compared to design 13. The designs are comparable in the number of turns, material, and rod diameter; however, the lengths differ. By combining the fact that the length of Design 12 is shorter than Design 13 and the flux density is lower for Design 12, the core losses are expected to be lower. The lower flux density can be explained by the lower magnetizing inductance for design 12, as seen in Table 5.4.

Table 5.5: The analytical core losses for design 12 and 13 from Table 5.4.

Design number	Core Losses [W]	Core length [mm]
12	7.5907	158.75
13	8.3370	165.12

With the transformer sizing and the power losses fully determined for the two designs, the infor-

mation is obtained to choose a final transformer design. In this chapter's next and final section, the decision for the final transformer design is presented along with the reasoning.

5.5. Final Transformer Parameters

An overview of the transformer parameters and performance specifications is shown in Table 5.6 for transformer designs 12 and 13. In Table 5.7, the design specifications from the LLC design are repeated as the values are used to validate the transformer design. The comparison of the two transformers starts with the similarities before moving on to the differences.

Starting with the series inductance L_r , both transformers have a significantly lower series inductance than the LLC requirement. In addition, the two series inductances are very similar. Second, despite the different number of rods used, the overall lengths do not differ much. Combining this with the fact that the outer radius of both transformers is equal results in a similar total volume. Third, the overall losses of the two transformers are very similar, resulting in a similar efficiency and power density. Fourth, the coupling coefficients of both transformers are very similar. Fifth and last, the number of turns is equal for both transformers.

More interesting regarding the decision for the transformer are the differences between the two designs. While the number of turns is equal, the resulting inductances do differ. First of all, the magnetizing inductance is higher for design 13. With the same number of turns and a longer rod, the inductance would be expected to decrease instead of increase. However, the increase in the inductance modifier and the effective permeability compensates for the decrease caused by the longer rod, resulting in a higher inductance. This applies to all inductances except the series inductance. Since the series inductance is determined by the ratio of the mutual inductance squared over the secondary self-inductance, the increase in both inductances counteracts each other.

The difference between the magnetizing inductance is further highlighted. Design 12 has a magnetizing inductance close to the required magnetizing inductance from the LLC design. Nevertheless, to keep the resonant tank's voltage gain response, the inductance ratio m value needs to remain constant. As a result, the series inductance and capacitor need to be adjusted to keep the same maximum quality factor. The resonance frequency of the LLC converter will be different due to the component changes. For both designs, the LLC components need to be recalculated. However, the larger magnetizing inductance of design 13 will result in larger values for the series inductance and capacitor. As a result, the resonance frequency and the switching frequency are reduced.

A last difference between the two designs is the distribution of the losses. Design 12's core losses are lower than design 13 because of the lower flux density and shorter length. In contrast, the winding losses for design 13 are lower compared to design 12. As design 12 has a shorter rod length, the magnetic field strength increases, resulting in higher proximity losses on both the primary and secondary winding.

Considering the higher potential for reducing core losses, design 13 is chosen as the preferred transformer design. In the next subsection, the LLC components are recalculated using the transformer's magnetization inductance.

5.5.1. Recalculation LLC components

To ensure the LLC voltage gain behaviour remains the same as designed in Chapter 4, the series inductance L_r and capacitor C_r are recalculated. This is done such that the inductance ratio m and the maximum quality factor Q_{max} remain constant. As a result, the resonance frequency will be altered.

In Equations (5.49) to (5.51), the previously introduced equations are rewritten to obtain the values for L_r , C_r and f_s respectively. The design procedure of the LLC converter is partly repeated to obtain the minimum, maximum and maximum power frequencies with the newly obtained resonance frequency as shown in Table 5.8. Interestingly, as the LLC component values and resonance frequency change, the current peaks and the phase difference remain the same.

$$L_r = \frac{L_m}{m - 1} \quad (5.49)$$

$$C_r = \frac{L_r}{Q_{max}^2 R_{ac,min}^2} \quad (5.50)$$

$$f_r = \frac{1}{2\pi\sqrt{C_r L_r}} \quad (5.51)$$

Table 5.6: The overview of transformer specifications for designs 12 and 13.

Parameter	Design 12	Design 13
n_s	5	4
Total length [mm]	158.75	165.12
Outer radius [mm]	16.2	16.2
Volume [cm ³]	130.6	135.8
$N_{p,s}$	39	39
L_m [μ H]	90.13	94.19
L_r [μ H]	4.850	4.825
L_p [μ H]	90.39	94.37
L_s [μ H]	94.96	99.10
M [μ H]	90.13	94.19
Coupling factor k	0.973	0.974
Primary winding losses [W]	21.40	20.98
Secondary winding losses [W]	24.61	23.5
Core losses [W]	7.59	8.34
Total losses [W]	53.60	52.82
Efficiency η [%]	98.25	98.28
Power density [MW/m ³]	23.1	22.2

Lastly, as the frequency of the maximum power operation has changed, the losses of the transformer need to be recalculated using the new frequency. As a result of the lower switching frequency, the losses are slightly reduced. The overview of the recalculated losses is shown in Table 5.9.

Table 5.8: The recalculated LLC component values and specifications based on the transformer magnetizing inductance.

Parameter	Value
m	3.875
C_r	154 nF
L_r	32.76 μ H
L_m	94.19 μ H
f_r	70.88 kHz
$f_{s,min}$	43.90 kHz
$f_{s,mp}$	80.88 kHz
$f_{s,max}$	90.90 kHz
\hat{I}_{prim}	17.55 A
\hat{I}_{sec}	15.65 A
$i_{p,s}\angle$	26.93°

Table 5.7: The designed LLC converter characteristics.

Parameter	Value
m	3.875
$f_{s,min}$	46.56 kHz
$f_{s,mp}$	85.59 kHz
$f_{s,max}$	92.35 kHz
C_r	146 nF
L_r	30.86 μ H
L_m	88.72 μ H
\hat{I}_{prim}	17.55 A
\hat{I}_{sec}	15.65 A
$i_{p,s}\angle$	26.93°

Table 5.9: The recalculated losses of the transformer with the new LLC specifications.

Parameter	Value
Primary winding losses [W]	15.72
Secondary winding losses [W]	17.16
Core losses [W]	7.14
Total losses [W]	40.02
Efficiency η [%]	98.69
Power density [MW/m ³]	22.2

6

Conclusions and Future Work

6.1. Conclusion

Finally, the results of this research are reflected in the research questions posed at the beginning. First, the sub-research questions are repeated in the following paragraphs, followed by the corresponding answers before the main research question. The section is concluded by comparing the designed CET and its components with the specifications.

The first discussed sub-research question is: 'What is the influence of the space environment on electronics used in satellites?'. As it turns out, the space environment is not a true vacuum, as charged particles are generated from the sun and the interaction of solar rays with Earth's atmosphere. Charge particles, especially high-energy electrons, cause surface and deep dielectric charging, potentially resulting in arcing. Furthermore, Prolonged exposure to radiation leads to the total dose effect, resulting in logic circuit errors. In addition, the space environment experiences large temperature swings depending on the sun's irradiance. In conclusion, electronics used in space applications require strict requirements regarding operating temperatures, arcing risk evaluation and logic circuit redundancy.

The second sub-research question is: 'What is the optimal structure for the AC-link?'. To gain the required knowledge to answer this question, prototype CET systems found in the literature were reviewed. Specifically, the CPT and IPT were compared. The latter provided a higher power density, power throughput and efficiency than the CPT method. After further reviewing the prototype IPT structures, the radial transformer had a higher power density throughput than the axial transformer, while both showed similar efficiencies. Furthermore, the scalability of the radial transformer was confirmed by the prototypes in the literature. The most optimal geometry for the AC-the link was determined to be an LL-shaped rotary transformer.

The third sub-research question is: 'What is the optimal conversion technique to transfer energy contactlessly?'. In Section 3.3, the SABL and LLC converter topologies are introduced for the conversation process. By comparing the two topologies through an example converter, the LLC converter required a smaller apparent input power than the SABL converter, resulting in smaller reactive components. In addition, the LLC converter can operate in boost and buck mode, allowing an extensive input voltage range. This is especially important as the solar panel output voltage can vary significantly. It should be noted that both converter types are capable of ZVS to reduce switching losses. Even though an extra capacitor is introduced, the LLC converter is considered the most suitable converter.

Furthermore, the inverter used in the LLC converter can either be a half- or a full-bridge. After reviewing both bridge topologies, the full-bridge offered a more extensive output voltage range and lower conduction losses than the half-bridge, even though the number of switches is doubled. Thus, an LLC converter with a full-bridge as an inverter is the most optimal conversion technique to transfer energy contactlessly.

Next, the main research question is: 'How can energy be transferred from the stator to the rotor contactlessly in a space environment?'. The answer to this question is obtained by combining the answers to the three sub-research questions. Firstly, the CET system uses an LLC converter with the full-bridge inverter. The inverter drives an LL-shaped rotary transformer designed according to the magnetizing inductance requirement from the LLC converter and an external inductor with an inductance to achieve

the series inductance requirement from the LLC converter. For all the electrical components, both power and signal, used, temperature, arcing and total dose effects need to be considered when determining the requirements.

Lastly, the design process for a proof-of-concept prototype LLC converter and coaxial solenoid transformer is presented in this work. An LLC converter is designed based on the requirements set for the satellite CET system. The required input voltage range of the LLC converter was almost reached. The maximum voltage gain of the designed LLC converter turned out to be slightly lower during transient simulation in LTspice, resulting in a slightly higher minimum input voltage. Nevertheless, the LLC converter design reached the required power transfer of $P = 3 \text{ kW}$.

Following the LLC design results, a prototype transformer was designed using the magnetizing inductance requirement through analytical equations and the FEMM tool. The transformer achieved an efficiency of 98.69%, which is slightly low considering the total CET system efficiency requirement was set to at least 98%. It should be noted that the required system efficiency will not be reached when the losses of the inverter, rectifier and external inductor are included. The largest source of transformer losses was the external proximity effect losses in the Litz wire. The overall transformer length and radius were, respectively, 165.12 mm and 16.2 mm and a power density of 22.2 MW/m^3 was achieved, which is higher than prototypes in the literature.

6.2. Future Work

The results presented in this work can be considered from preliminary research into the design of a satellite CET system. Even though a proof-of-concept satellite CET system is presented in this work, many areas need further research before a design can be used in spacecraft.

Firstly, the proof-of-concept transformer design does not have the most optimal transformer geometry, as deduced from this work. The main reason for this is the limited time of this research and the long lead times for custom ferrite core shapes. Future research can investigate whether the LL-shaped rotary transformer results in smaller transformer dimensions or if reducing the number of turns is possible. With a reduction in the number of turns, it is possible to reduce the winding losses of the transformer.

Secondly, the proof-of-concept transformer prototype has not been assembled and tested in this work. Measurements regarding the leakage and magnetizing inductance are required to validate the analytical and FEMM results before an external inductor can be designed. In addition, the power losses and efficiency need to be investigated in experimental setups to validate the analytical methods presented in this work. Furthermore, a thermal model and experimental validation for the space environment are required to see if the transformer size needs to be increased for cooling purposes.

Thirdly, a preliminary investigation of the effects of the space environment on electronics is presented in this work. Before these effects can be tackled in the design phase, specific design requirements regarding the electrical components in the CET system must be established.

Lastly, the satellite CET system control is not discussed during this research. Research in the literature shows that the LLC converter frequency is used for the solar panel MPPT [47]. In addition, the battery's output voltage is considered constant in this research. However, further research needs to be conducted to determine if the CET system can be used for battery management purposes when this function is considered during the design of the control system.

Bibliography

- [1] “Satellite communications,” in *Protocols for High-Efficiency Wireless Networks*, A. Andreadis and G. Giambene, Eds., Boston, MA: Springer US, 2002, pp. 91–114, ISBN: 978-0-306-47795-9. DOI: 10.1007/0-306-47795-5_4. [Online]. Available: https://doi.org/10.1007/0-306-47795-5_4 (visited on 08/23/2024).
- [2] J. Schulz, P. Albert, H.-D. Behr, *et al.*, “Operational climate monitoring from space: The EU-METSAT satellite application facility on climate monitoring (CM-SAF),” *Atmospheric Chemistry and Physics*, vol. 9, no. 5, pp. 1687–1709, Mar. 5, 2009, Publisher: Copernicus GmbH, ISSN: 1680-7316. DOI: 10.5194/acp-9-1687-2009. [Online]. Available: <https://acp.copernicus.org/articles/9/1687/2009/> (visited on 08/23/2024).
- [3] N. G. McDowell, N. C. Coops, P. S. A. Beck, *et al.*, “Global satellite monitoring of climate-induced vegetation disturbances,” *Trends in Plant Science*, vol. 20, no. 2, pp. 114–123, Feb. 1, 2015, Publisher: Elsevier, ISSN: 1360-1385. DOI: 10.1016/j.tplants.2014.10.008. [Online]. Available: [https://www.cell.com/trends/plant-science/abstract/S1360-1385\(14\)00272-6](https://www.cell.com/trends/plant-science/abstract/S1360-1385(14)00272-6) (visited on 08/23/2024).
- [4] A. Mackey. “Recap of all global launches for 2023,” SpaceWorks Enterprises, Inc. (Jan. 10, 2024), [Online]. Available: <https://www.spaceworks.aero/recap-of-all-global-launches-for-2023/> (visited on 04/22/2024).
- [5] T. G. Roberts. “Cost for space launch to low earth orbit- aerospace security project,” Aerospace Security. (Sep. 1, 2022), [Online]. Available: <https://aerospace.csis.org/data/space-launch-to-low-earth-orbit-how-much-does-it-cost/> (visited on 08/23/2024).
- [6] A. C. Boley and M. Byers, “Satellite mega-constellations create risks in low earth orbit, the atmosphere and on earth,” *Scientific Reports*, vol. 11, no. 1, p. 10642, May 20, 2021, Publisher: Nature Publishing Group, ISSN: 2045-2322. DOI: 10.1038/s41598-021-89909-7. [Online]. Available: <https://www.nature.com/articles/s41598-021-89909-7> (visited on 08/23/2024).
- [7] Y. Yang, M. Xu, D. Wang, and Y. Wang, “Towards energy-efficient routing in satellite networks,” *IEEE Journal on Selected Areas in Communications*, vol. 34, no. 12, pp. 3869–3886, Dec. 2016, Conference Name: IEEE Journal on Selected Areas in Communications, ISSN: 1558-0008. DOI: 10.1109/JSAC.2016.2611860. [Online]. Available: <https://ieeexplore.ieee.org/abstract/document/7572177> (visited on 06/20/2024).
- [8] J. Wang, R. Liu, R. Xiao, *et al.*, “Optimized design of slip ring assembly for aerospace to reduce deep dielectric charging,” *IEEE Transactions on Nuclear Science*, vol. 69, no. 4, pp. 915–924, Apr. 2022, Conference Name: IEEE Transactions on Nuclear Science, ISSN: 1558-1578. DOI: 10.1109/TNS.2022.3157670. [Online]. Available: https://ieeexplore.ieee.org/abstract/document/9729830?casa_token=DI1_JGhuXOQAAAAA:-ghGNk5QbU8_3XftNrGSXKuybu4fM7c8kR2-6HLp1oSMgBJihxIrVWeteTE-ZZb0ZiPWK26hma (visited on 01/25/2024).
- [9] F. Avino, P. Martens, A. A. Howling, D. Bommottet, and I. Furno, “Gas breakdown mitigation in satellite slip rings,” *Aerospace Science and Technology*, vol. 85, pp. 229–233, Feb. 1, 2019, ISSN: 1270-9638. DOI: 10.1016/j.ast.2018.12.010. [Online]. Available: <https://www.sciencedirect.com/science/article/pii/S1270963817305588> (visited on 01/25/2024).
- [10] M. C. Kelley, *The Earth’s Ionosphere: Plasma Physics and Electrodynamics*. Academic Press, Jun. 12, 2009, 593 pp., Google-Books-ID: 3GIWQnjBQNgC, ISBN: 978-0-08-091657-6.
- [11] T. G. Roberts. “Popular orbits 101,” Aerospace Security. (Nov. 30, 2017), [Online]. Available: <https://aerospace.csis.org/aerospace101/earth-orbit-101/> (visited on 03/11/2024).
- [12] G. Genta, “Space environment and radiations,” in *Next Stop Mars: The Why, How, and When of Human Missions*, ser. Springer Praxis Books, G. Genta, Ed., Cham: Springer International Publishing, 2017, pp. 83–100, ISBN: 978-3-319-44311-9. DOI: 10.1007/978-3-319-44311-9_4. [Online]. Available: https://doi.org/10.1007/978-3-319-44311-9_4 (visited on 03/12/2024).

- [13] W. Li and M. Hudson, "Earth's van allen radiation belts: From discovery to the van allen probes era," *Journal of Geophysical Research: Space Physics*, vol. 124, no. 11, pp. 8319–8351, 2019, eprint: <https://onlinelibrary.wiley.com/doi/pdf/10.1029/2018JA025940>, ISSN: 2169-9402. DOI: 10.1029/2018JA025940. [Online]. Available: <https://onlinelibrary.wiley.com/doi/abs/10.1029/2018JA025940> (visited on 03/12/2024).
- [14] Y. Lu, Q. Shao, H. Yue, and F. Yang, "A review of the space environment effects on spacecraft in different orbits," *IEEE Access*, vol. 7, pp. 93 473–93 488, 2019, Conference Name: IEEE Access, ISSN: 2169-3536. DOI: 10.1109/ACCESS.2019.2927811. [Online]. Available: <https://ieeexplore.ieee.org/abstract/document/8758870> (visited on 08/25/2024).
- [15] R. Schnyder, A. A. Howling, D. Bommottet, and C. Hollenstein, "Direct current breakdown in gases for complex geometries from high vacuum to atmospheric pressure," *Journal of Physics D: Applied Physics*, vol. 46, no. 28, p. 285 205, Jun. 2013, Publisher: IOP Publishing, ISSN: 0022-3727. DOI: 10.1088/0022-3727/46/28/285205. [Online]. Available: <https://dx.doi.org/10.1088/0022-3727/46/28/285205> (visited on 01/25/2024).
- [16] D. B. Go and A. Venkatraman, "Microscale gas breakdown: Ion-enhanced field emission and the modified paschen's curve," *Journal of Physics D: Applied Physics*, vol. 47, no. 50, p. 503 001, Nov. 2014, Publisher: IOP Publishing, ISSN: 0022-3727. DOI: 10.1088/0022-3727/47/50/503001. [Online]. Available: <https://dx.doi.org/10.1088/0022-3727/47/50/503001> (visited on 02/05/2024).
- [17] K. T. a. L. Burm, "Calculation of the townsend discharge coefficients and the paschen curve coefficients," *Contributions to Plasma Physics*, vol. 47, no. 3, pp. 177–182, 2007, ISSN: 1521-3986. DOI: 10.1002/ctpp.200710025. [Online]. Available: <https://onlinelibrary.wiley.com/doi/abs/10.1002/ctpp.200710025> (visited on 01/30/2024).
- [18] F. Avino, B. Gaffinet, D. Bommottet, A. Howling, and I. Furno, "Slip ring test assembly with increased breakdown voltage limit for high-voltage bus satellites," *IEEE Aerospace and Electronic Systems Magazine*, vol. 35, no. 8, pp. 32–36, Aug. 2020, Conference Name: IEEE Aerospace and Electronic Systems Magazine, ISSN: 1557-959X. DOI: 10.1109/MAES.2020.2993388. [Online]. Available: https://ieeexplore.ieee.org/abstract/document/9161332?casa_token=0CpxkCHuo1EAAAAA:QU3KU6NMua0wCHtxfsWUsM2TTwEs4ntbAQGX8kw63igTfFwsLtFdIEG5XxL7a8Nr3ejCKp74Aw (visited on 01/25/2024).
- [19] L. Kiener, H. Saudan, D. Novo, *et al.*, "Slipring rotor made by additive manufacturing: Redesign, manufacturing and validation testing for space applications," in *ACTUATOR; International Conference and Exhibition on New Actuator Systems and Applications 2021*, Feb. 2021, pp. 1–4. [Online]. Available: <https://ieeexplore.ieee.org/abstract/document/9400632> (visited on 01/25/2024).
- [20] X. Chen, Y. Wang, Y. Sheng, C. Yu, X. Yang, and J. Xi, "Vision-aided brush alignment assembly system for precision conductive slip rings," *Machines*, vol. 10, no. 5, p. 393, May 2022, Number: 5 Publisher: Multidisciplinary Digital Publishing Institute, ISSN: 2075-1702. DOI: 10.3390/machines10050393. [Online]. Available: <https://www.mdpi.com/2075-1702/10/5/393> (visited on 01/25/2024).
- [21] T. Deceuleneer, "Contactless power transfer through a rotating transformer for spatial application," Ph.D. dissertation, 2016.
- [22] D. Wang, S. Cui, Z. Bie, J. Zhang, K. Song, and C. Zhu, "A redundancy design of wireless power transfer system for satellite slip ring with high reliability," in *2021 IEEE 4th International Electrical and Energy Conference (CIEEC)*, May 2021, pp. 1–6. DOI: 10.1109/CIEEC50170.2021.9511063. [Online]. Available: <https://ieeexplore.ieee.org/abstract/document/9511063> (visited on 01/25/2024).
- [23] Y. Yang, X. Liu, H. Zhang, and Y. Shi, "A dual coupling LCC-LCC topology based WPT system for wireless slip ring," in *2023 IEEE 2nd International Conference on Electrical Engineering, Big Data and Algorithms (EEBDA)*, Feb. 2023, pp. 1333–1336. DOI: 10.1109/EEBDA56825.2023.10090535. [Online]. Available: <https://ieeexplore.ieee.org/abstract/document/10090535> (visited on 01/25/2024).

- [24] T. D. Gerarden, "Demanding innovation: The impact of consumer subsidies on solar panel production costs," *Management Science*, vol. 69, no. 12, pp. 7799–7820, Dec. 2023, Publisher: INFORMS, ISSN: 0025-1909. DOI: 10.1287/mnsc.2022.4662. [Online]. Available: <https://pubsonline.informs.org/doi/full/10.1287/mnsc.2022.4662> (visited on 08/26/2024).
- [25] W. Guter, F. Dunzer, L. Ebel, *et al.*, "Space solar cells – 3g30 and next generation radiation hard products," *E3S Web of Conferences*, vol. 16, p. 03 005, 2017, Publisher: EDP Sciences, ISSN: 2267-1242. DOI: 10.1051/e3sconf/20171603005. [Online]. Available: https://www.e3s-conferences.org/articles/e3sconf/abs/2017/04/e3sconf_espc2017_03005/e3sconf_espc2017_03005.html (visited on 06/17/2024).
- [26] "Projects & references - AZUR SPACE solar power GmbH." (), [Online]. Available: <https://www.azurspace.com/index.php/en/company/projects-references> (visited on 06/18/2024).
- [27] *30% triple junction GaAs solar cell, type: TJ solar cell 3g30c - advanced*, Jun. 5, 2019. [Online]. Available: https://www.azurspace.com/images/006050-01-00_DB_3G30C-Advanced.pdf (visited on 06/18/2024).
- [28] D. Sera, R. Teodorescu, and P. Rodriguez, "PV panel model based on datasheet values," in *2007 IEEE International Symposium on Industrial Electronics*, ISSN: 2163-5145, Jun. 2007, pp. 2392–2396. DOI: 10.1109/ISIE.2007.4374981. [Online]. Available: https://ieeexplore.ieee.org/abstract/document/4374981?casa_token=42Dd-c-EI4UAAAA:sLigm6wE1mRqYwJDiwIDbNVafwoJgUpw5nCcI3S33cbbp91aBuD1w37DfH147Vns1TiJkoL-g (visited on 06/17/2024).
- [29] Y. Zhang, J. Yang, D. Jiang, D. Li, and R. Qu, "Design, manufacture, and test of a rotary transformer for contactless power transfer system," *IEEE Transactions on Magnetics*, vol. 58, no. 2, pp. 1–6, Feb. 2022, Conference Name: IEEE Transactions on Magnetics, ISSN: 1941-0069. DOI: 10.1109/TMAG.2021.3094135. [Online]. Available: https://ieeexplore.ieee.org/abstract/document/9469925?casa_token=cRGM1a-josEAAAA:gHqGIodI8SyHSHcUGHFkxoXaqzdFpFtNLhkS82_rCmM5x1TiWp8DoRcr_dMjoRR1Gm30z-da7Q (visited on 01/25/2024).
- [30] C. Stancu, T. Ward, K. M. Rahman, R. Dawsey, and P. Savagian, "Separately excited synchronous motor with rotary transformer for hybrid vehicle application," *IEEE Transactions on Industry Applications*, vol. 54, no. 1, pp. 223–232, Jan. 2018, Conference Name: IEEE Transactions on Industry Applications, ISSN: 1939-9367. DOI: 10.1109/TIA.2017.2757019. [Online]. Available: https://ieeexplore.ieee.org/abstract/document/8052125?casa_token=RcoHn9ZXNXQAAAA:IwYwiwKh48xwMntj25aNs2yJirxP-wiGXz6fTgVRNBq8Qk4N0mQjc8-a8f11Ec2BDDxZQBs9w (visited on 01/25/2024).
- [31] M. Maier and N. Parspour, "Operation of an electrical excited synchronous machine by contactless energy transfer to the rotor," *IEEE Transactions on Industry Applications*, vol. 54, no. 4, pp. 3217–3225, Jul. 2018, Conference Name: IEEE Transactions on Industry Applications, ISSN: 1939-9367. DOI: 10.1109/TIA.2018.2814558. [Online]. Available: <https://ieeexplore.ieee.org/abstract/document/8310956> (visited on 01/25/2024).
- [32] A. Littau, B. Wagner, S. Köhler, A. Dietz, and S. Weber, "Design of inductive power transmission into the rotor of an externally excited synchronous machine," 2014. [Online]. Available: <https://www.semanticscholar.org/paper/Design-of-Inductive-Power-Transmission-into-the-of-Littau-Wagner/70e138693c5cbb7797619cb004c351655c45138d> (visited on 01/25/2024).
- [33] H. Krupp and A. Mertens, "Rotary transformer design for brushless electrically excited synchronous machines," in *2015 IEEE Vehicle Power and Propulsion Conference (VPPC)*, Oct. 2015, pp. 1–6. DOI: 10.1109/VPPC.2015.7353009. [Online]. Available: https://ieeexplore.ieee.org/abstract/document/7353009?casa_token=YcdXBp8uqBMAAAAA:afJebFBi5SUVc7fcYSiKkr rF00mCBIG7ApN8qADWk-XDEatzZTDNBE1An30t6xboNCQ71U23bQ (visited on 01/25/2024).
- [34] S.-A. Vip, J.-N. Weber, A. Rehfeldt, and B. Ponick, "Rotary transformer with ferrite core for brushless excitation of synchronous machines," in *2016 XXII International Conference on Electrical Machines (ICEM)*, Sep. 2016, pp. 890–896. DOI: 10.1109/ICELMACH.2016.7732631. [Online]. Available: https://ieeexplore.ieee.org/abstract/document/7732631?casa_token=TR8kBOxvSQ8AAAA:72nMnmsC5m3ONMBQxL5ep6Zq_zBqPLWt9R02TFMRF9tdqE71YY8CrRS5Cq8fpjYrGVH0eLrPPg (visited on 01/25/2024).

- [35] L. Sun, J. Kang, Y. Liu, Z. Mao, and Z. Zhong, "Wireless power transfer based contactless excitation of electrically excited synchronous motor," in *2020 IEEE 9th International Power Electronics and Motion Control Conference (IPEMC2020-ECCE Asia)*, Nov. 2020, pp. 1091–1097. DOI: 10.1109/IPEMC-ECCEAsia48364.2020.9368049. [Online]. Available: <https://ieeexplore.ieee.org/abstract/document/9368049> (visited on 01/25/2024).
- [36] D. C. Ludois, J. K. Reed, and K. Hanson, "Capacitive power transfer for rotor field current in synchronous machines," *IEEE Transactions on Power Electronics*, vol. 27, no. 11, pp. 4638–4645, Nov. 2012, Conference Name: IEEE Transactions on Power Electronics, ISSN: 1941-0107. DOI: 10.1109/TPEL.2012.2191160. [Online]. Available: https://ieeexplore.ieee.org/abstract/document/6170566?casa_token=J7P-_Agu4wgAAAAA:3pQSmHLsLn59ibFSzUPYFNxeLjDguVxbwd64QHhTXeg9CuAMN49oInnN4uZJeUmZhC3Y5V-nkg (visited on 01/25/2024).
- [37] J. Dai, S. Hagen, D. C. Ludois, and I. P. Brown, "Synchronous generator brushless field excitation and voltage regulation via capacitive coupling through journal bearings," *IEEE Transactions on Industry Applications*, vol. 53, no. 4, pp. 3317–3326, Jul. 2017, Conference Name: IEEE Transactions on Industry Applications, ISSN: 1939-9367. DOI: 10.1109/TIA.2017.2681621. [Online]. Available: https://ieeexplore.ieee.org/abstract/document/7876734?casa_token=YcBvfTzDxCkAAAAA:rCRoNGF8AvTs-xGnIK4zkwWTLuNEzS1zK1o6zwdl1fMBgHTnkJ2SKft4tEDPwYMur074IATNxMg (visited on 01/25/2024).
- [38] N. Mohan, T. M. Undeland, and W. P. Robbins. "Power electronics: Converters, applications, and design, 3rd edition | wiley," Wiley.com. (Oct. 2002), [Online]. Available: <https://www.wiley.com/en-us/Power+Electronics%3A+Converters%2C+Applications%2C+and+Design%2C+3rd+Edition-p-9780471226932> (visited on 05/13/2024).
- [39] C. Fontana, M. Forato, K. Kumar, M. T. Outeiro, M. Bertoluzzo, and G. Buja, "Soft-switching capabilities of SAB vs. DAB converters," in *IECON 2015 - 41st Annual Conference of the IEEE Industrial Electronics Society*, Nov. 2015, pp. 003 485–003 490. DOI: 10.1109/IECON.2015.7392640. [Online]. Available: https://ieeexplore.ieee.org/abstract/document/7392640?casa_token=wR917WrYq-wAAAAA:zmtIC-ElGIxysaShyIqQF2j0JCDSMa0_vKbe47vN1uvnHxa5LdTI2UNnzXTV7m8jKKQqxr0_BA (visited on 06/13/2024).
- [40] R. Jha, M. Forato, S. Prakash, H. Dashora, and G. Buja, "An analysis-supported design of a single active bridge (SAB) converter," *Energies*, vol. 15, no. 2, p. 666, Jan. 2022, Number: 2 Publisher: Multidisciplinary Digital Publishing Institute, ISSN: 1996-1073. DOI: 10.3390/en15020666. [Online]. Available: <https://www.mdpi.com/1996-1073/15/2/666> (visited on 05/15/2024).
- [41] S. Abdel-Rahman, "Resonant LLC converter: Operation and design," 2012.
- [42] Fair-Rite. "Rods (4077484611)," Fair-Rite. (), [Online]. Available: <https://fair-rite.com/product/rods-4077484611/> (visited on 09/20/2024).
- [43] J. Mühlethaler, "Modeling and multi-objective optimization of inductive power components," Accepted: 2020-05-12T08:28:31Z, Doctoral Thesis, ETH Zurich, 2012. DOI: 10.3929/ethz-a-007328104. [Online]. Available: <https://www.research-collection.ethz.ch/handle/20.500.11850/153529> (visited on 08/14/2024).
- [44] D. Meeker, *Finite element method magnetics version 4.2 user's manual*, May 15, 2020. [Online]. Available: <https://www.femm.info/wiki/Documentation/> (visited on 09/22/2024).
- [45] P. Ponomarev, "Tooth-coil permanent magnet synchronous machine design for special applications," Ph.D. dissertation, Oct. 24, 2013.
- [46] L. Petrescu, V. Ionita, E. Cazacu, and C. Petrescu, "Steinmetz' parameters fitting procedure for the power losses estimation in soft magnetic materials," in *2017 International Conference on Optimization of Electrical and Electronic Equipment (OPTIM) & 2017 Intl Aegean Conference on Electrical Machines and Power Electronics (ACEMP)*, May 2017, pp. 208–213. DOI: 10.1109/OPTIM.2017.7974972. [Online]. Available: <https://ieeexplore.ieee.org/abstract/document/7974972> (visited on 09/23/2024).

- [47] Y. Zhuang, F. Liu, X. Zhang, X. Diao, J. Jiang, and J. Sun, "Direct frequency control based MPPT algorithm of LLC resonant converter for photovoltaic system," in *2019 IEEE Energy Conversion Congress and Exposition (ECCE)*, ISSN: 2329-3748, Sep. 2019, pp. 3402–3406. DOI: 10.1109/ECCE.2019.8912689. [Online]. Available: <https://ieeexplore.ieee.org/abstract/document/8912689> (visited on 06/10/2024).

A

LTspice Circuit

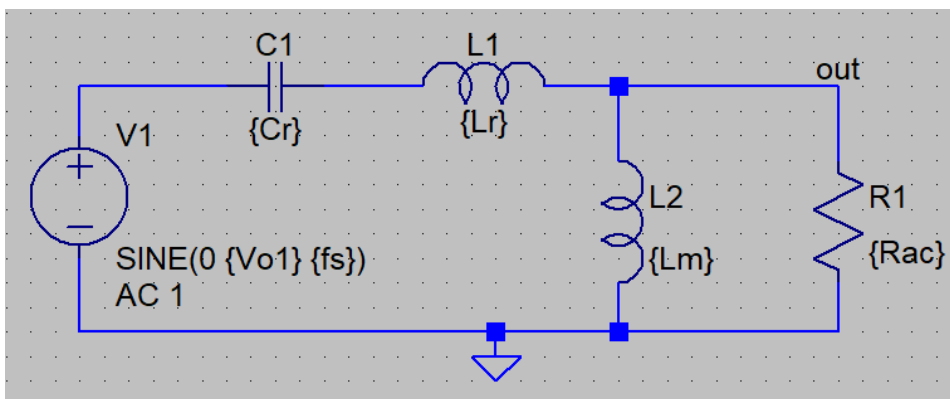


Figure A.1: The LTspice circuit is used to perform transient and transfer analysis of the LLC converter.

B

Core specifications

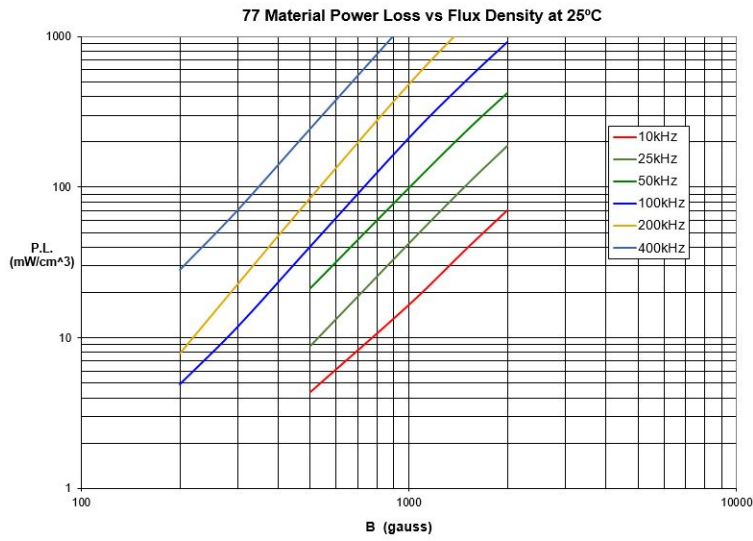
B.1. Ferrite rods

B.1.1. Rod Dimensions

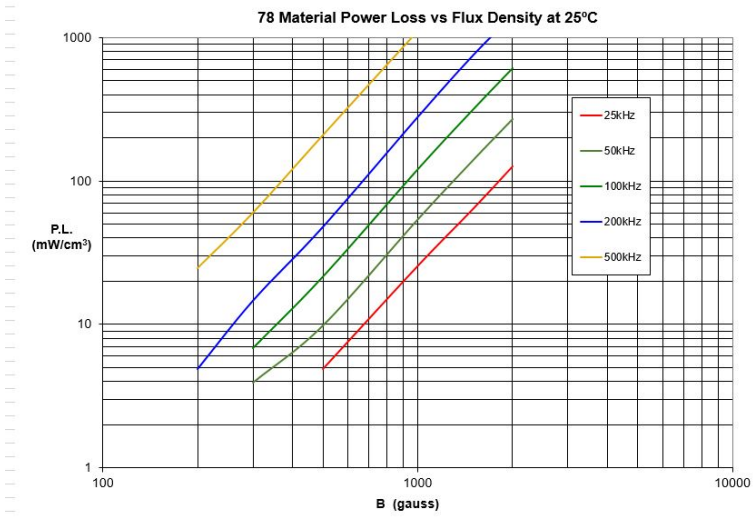
Table B.1: The considered rods from Fair-rite.

Rod diameter (d_r) [mm]	Rod length (l_r) [mm]	Material
0.76	7.5	78
1	10	78
1.5	15	78
2	15	78
2.5	20	78
3	25	78
3.25	25.4	77
4	30	78
4.45	22.	77
5	35	78
6.35	25.4	77
6.35	38.1	77
6.35	40	78
8	38.1	77
8	45	78
9.45	31.75	77
9.45	38.1	78
9.45	50.8	77
9.5	41.28	77
9.5	70	78
12.3	31.75	77
12.3	41.28	77

B.1.2. Core Loss Curves



(a) Material 77



(b) Material 78

Figure B.1: The core losses versus flux density for different frequencies.